EXPERIMENTAL AND NUMERICAL ANALYSIS OF HEAT TRANSFER PERFORMANCE OF OFF-SET STRIP FINS

A Thesis Submitted to
The Graduate School of Engineering and Science of
İzmir Institute of Technology
in Partial Fulfillment of the Requirements for the Degree of

MASTER OF SCIENCE

in Energy Engineering

by
Gürcan DURMAZ

July 2009
İZMİR

We approve the thesis of **Gürcan DURMAZ**

_____
Assist. Prof. Dr. Ünver ÖZKOL
Supervisor

_____
Assoc. Prof. Dr. Erol ŞEKER
Co-Supervisor

_____
Assoc. Prof. Dr. Moghtada MOBEDİ
Committee Member

_____
Assoc. Prof. Dr. Aytunç EREK
Committee Member

06 July 2009

_____
Assist. Prof. Dr. Ünver ÖZKOL
Head of the Energy Engineering Department

_____
Prof. Dr. Hasan BÖKE
Dean of the Graduate School of Engineering and Science

ACKNOWLEDGEMENT

I wish to thank all my committee members, and various faculty members who have encouraged and helped me.

I would like to express my sincere gratitude to my supervisor Assist. Prof. Dr. Ünver ÖZKOL for giving me the opportunity to work under him and for his valuable advises and guidance through the thesis.

The author also wishes to express his thanks to his labmates, Necati BİLGİN, H. İbrahim YANIKTAŞ, and his friends for their help and support during his studies.

My parents, Ali and Saliha, my sister Münevver and my brother Sercan have always encouraged and supported my decisions.

ABSTRACT

EXPERIMENTAL AND NUMERICAL ANALYSIS OF HEAT TRANSFER PERFORMANCE OF OFF-SET STRIP FINS

The aim of this study is to computationally and experimentally investigate the heat transfer and pressure drop characteristics of an offset-strip fin. In the present study, experiments are conducted at the range of Reynolds number from 150 to 3500 and a 3-D numerical domain, which is investigated as a conjugate problem, is created for finite volume computations. The computations are conducted by assuming that the flow in the offset-strip fin channels is steady and laminar at the range of Reynolds numbers from 200 to 5000. In this thesis, the effects of the flow behaviors in the offset strip fin channels on Colbourn j factor, which is the non-dimensional form of heat transfer coefficient, and fanning friction f factor, which is the non-dimensional form of pressure drop, are investigated. Also, the heat transfer boundary conditions and the Prandtl numbers of the fluids are kept different for these fins in order to see the effect of those. The effect of Prandtl number is investigated by using air, $0.707 < Pr < 0.71$ and water, $2 < Pr < 4.35$ and ethylene glycol, $94 < Pr < 138$. The effect of the thermal boundary conditions is investigated by using constant heat flux and uniform temperature. Moreover, all results are compared with Kays and London's experiments (1964) and also the results of Manglik and Bergles's correlations (1995). The results show a very good agreement between the results of Kays and London (1964) and of Manglik and Bergles's correlations (1995). It is also observed that results obtained from the two alternatives for the thermal boundary condition are very close to each other. According to obtained results, it is concluded that our computational results from laminar flow assumption and experiments are reliable at almost all the range of Reynolds numbers studied.

ÖZET

OFF-SET STRIP TİPİNDEKİ KANATÇIKLARIN ISI TRANSFERİ PERFORMANSININ DENEYSEL VE SAYISAL OLARAK İNCELENMESİ

Bu çalışma, bir offset-strip tip kanatçığın ısı transferi ve basınç düşüm karakteristiklerinin deneysel ve sayısal olarak incelenmesini içermektedir. Deneyler, Reynolds sayısı 150 ile 3500 arasında gerçekleştirilmiş ve taşınım ile iletimi bir arada içeren bu problem, üç boyutlu bir sayısal model kullanılarak çözülmüştür. Sayısal analizler için sonlu hacim metodu kullanılmıştır. Offset-strip tip kanatçığın içerisindeki akış, Reynolds sayısı 200 ile 5000 arasında, laminer ve zamandan bağımsız olarak kabul edilmiş ve bu kabuller ışığında sayısal analizler gerçekleştirilmiştir. Offset-strip tip kanatçık içerisindeki akışın ısı transferine ve basınç düşümüne etkileri, bu parametrelerin birimsiz büyüklüğü olan Colbourn-j faktör ve Fanning friction f faktör cinsinden incelenmiştir. Ayrıca iki farklı termal sınır koşulu tanımlanarak (sabit sıcaklık ve sabit ısı akısı) ısı transferine ve basınç düşümüne etkileri incelenmiştir. Buna ek olarak hava, su ve etilen-glikol gibi üç farklı akışkan kullanılarak, Prandtl sayısının etkileri araştırılmıştır. Oluşturulan modelin sayısal analiz sonuçları ve elde edilen deneysel sonuçlar, Kays ve London'ın (1964) deneysel sonuçları ve Manglik ve Bergles'in korelasyonlarından elde edilen sonuçlar ile karşılaştırılmıştır. Elde edilen sonuçlar ile bu araştırmacıların sonuçları karşılaştırıldığında birbirleri ile çok iyi örtüştüğü görülmektedir. İki farklı ısıl sınır koşulu kullanılarak elde edilen sonuçlar, bu iki sınır koşulu arasında önemli bir fark olmadığını göstermiştir. Elde edilen tüm sonuçlar irdelendiği zaman, çalışmada kullanılmış olan sayısal modelin ve yapılmış olan deneylerin Reynolds sayısı 200 ile 5000 arsında oldukça güvenilir olduğu sonucuna varılmıştır.

TABLE OF CONTENTS

LIST OF FIGURES

LIST OF TABLES

Table **Page**

NOMENCLATURE

A	Cross sectional area	m^2
C_p	Specific heat	J/kg.K
D_h	Hydraulic diameter	mm
f	Fanning fdriction factor	
F	External force vector	N
h	Fin height	mm
h	Convective heat transfer coefficient	W/m^2K
i	Unit vector in x direction	
j	Unit vector in y direction	
k	Unit vector in z direction	
k	Thermal conductivity	W/mK
L or l	Fin lenght	mm
L_c	Channel length	mm
$\dot{m}$	Mass flow rate	kg/s
Nu	Nusselt number	
P	Pressure	Pa
Pr	Prandtl number	
Q	Heat transfer rate	W
q	Heat flux	W/m^2
R	Residual	
Re	Reynolds number	
s	Fin size	mm
t	Fin thickness	mm
t	Time	s
T	Temperature	K
U	Overall heat transfer coefficient	W/m^2K

u	Velocity vector	m/s
V	Volume	m^3
x	x coordinate	
y	y coordinate	
z	z coordinate	

Subscripts

air	for air
Al	for aluminium
water	for water
c	channel
f	fin
t	turbulance
x	in x direction
y	in y direction
z	in z direction

Greek

α	Under-relaxation factor	
Δ	Difference	
μ	Dynamic viscosity	kg/ms
ρ	Density	kg/m^3
Φ	General variable	
k	Turbulance kinetic energy generation	m^2/s^2
ε	Turbulance kinetic energy dissipation	m^2/s^2
∇	The vector differential operator	

CHAPTER 1

INTRODUCTION

Fundamental of heat exchanger principle is to facilitate an efficient heat flow from hot fluid to cold fluid. This heat flow is a direct function of the temperature difference between the two fluids, the area where heat is transferred, and the conductive/convective properties of the fluid and the flow state. This relation was formulated by Newton and called Newton's law of cooling, which is given in Equation 1.1.

$$Q = h\ A\ \Delta T \tag{1.1}$$

Where h is the heat transfer coefficient [W/m^2K], where fluid's conductive/convective properties and the flow state comes in the picture, A is the heat transfer area [m^2], and ΔT is the temperature difference [K].

In order to increase the heat transfer in a basic heat exchanger mechanism shown below in Figure 1.1, assuming that the heat transfer coefficient can not be changed, the area or the temperature differences have to be increased.

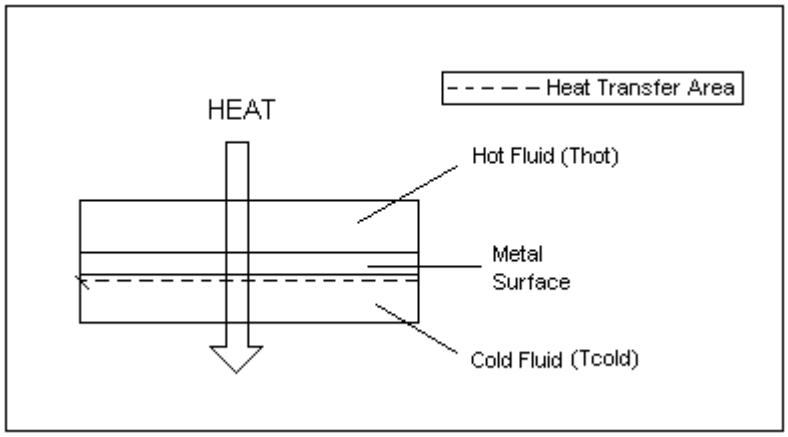

Figure 1.1. Basic heat exchanger mechanism

In practice, the best solution is that the heat transfer surface area is extended although increasing the temperature difference is logical, too. In reality, it may not be much meaningful to increase the temperature difference because either a hotter fluid should be supplied to mechanism or the heat should be transferred to a colder fluid where neither of them usually available. For both cases the system requires much more extra work. Furthermore increasing the temperature difference more than enough will cause unwanted thermal stresses on the metal surfaces between two fluids. The situation usually results in deformation and also decreases of life span of those materials. As a result of these facts, increasing the heat transfer surface area generally is the best engineering approach. One of the most widely used method is to employ extended metal interface surfaces between two fluids in order to extend the heat transfer surface area. These extended metal interfaces are usually called *Fins,* as shown in Figure1.2.

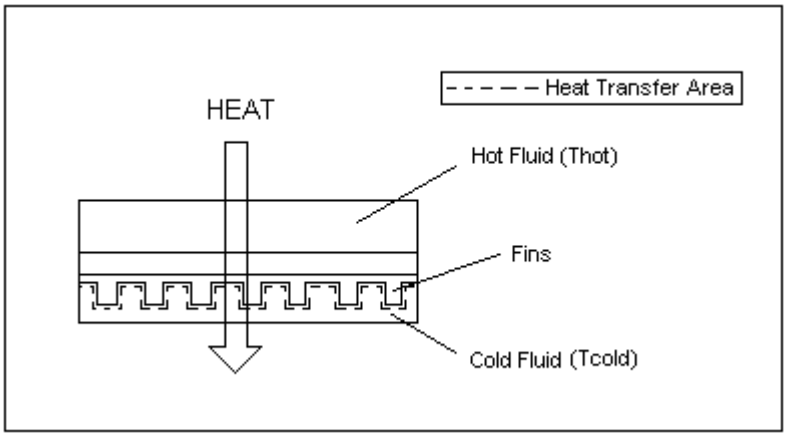

Figure 1.2. Basic heat exchanger mechanism with fins

Although there are so many methods which are applied for heat transfer enhancement such as using fins, swirl flow devices, coiled tubes, using plate or tube fins are the most commonly employed methods in heat exchangers. These types of exchangers are called as "*Extended Surface Heat Exchangers* or *Compact Heat Exchangers*". These types of heat exchangers including plate fins have been used in so many applications such as: automobile radiators, air-conditioning systems, condensers, electronic cooling devices, and regenerators, and cryogenic exchangers. Since the compact heat exchangers are lightweight and also have much smaller footprint, they are highly desirable in many applications.

Compact heat exchangers are categorized according to the amount of extended surface area per volume. There are many kinds of fins which are adopted in heat exchangers to increase the heat transfer rate. Among those, plate fins are known to be attractive for their simplicity of manufacture and potentials for enhanced thermal-hydraulic performance. Therefore they are preferred by many heat exchanger designers. Various different forms of plate fins may be found in application such as plain fins, offset strip fins, wavy fins, perforated fins, and pin fins, as shown in Figure1.3.

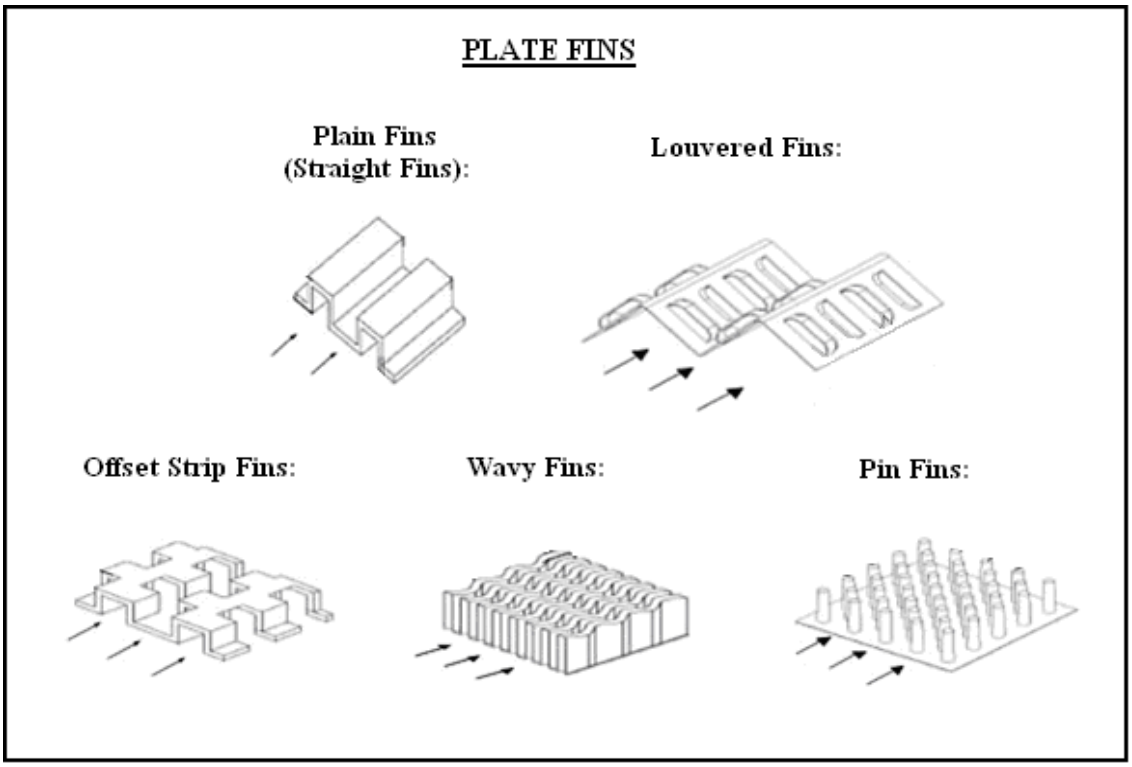

Figure 1.3. Types of plate fins.
(Source: Shah and Sekulic 2003)

The offset strips fins (OSF) are the most widely applied methods in order to achieve the required the heat transfer enhancement because of their excellent geometrical properties. The OSFs behave as short thin flat plates aligned with the flow direction. The flow passages of the OSF are periodically interrupted along the stream-wise direction. These interruptions in the geometry result in an initiation of the velocity and temperature boundary layers which in turn result in a higher heat transfer

coefficients and therefore more homogeneous temperature distributions. This enhancement is of course accompanied by an increase in pressure drop.

There are many published researches is available on extended surfaces and particularly on OSFs. Among those researches, the numerical methods have become increasingly popular recently because of the fact that detailed information about all kinds of heat transfer problems may be obtained by computational models. Moreover, computations can be more economical than experimental analysis. On the other hand, experimental analyses are always performed in order to confirm numerical results. Also experiments can be the only solution for problems where no numerical models are available and where geometry is too complicated or very big in size.

Working fluids, the required heat flow rate and/or mass flow rates are usually known in most heat exchanger problems. If certain correlations between geometry and fin performance are established, then the problem can be greatly simplified. For that purpose two correlation factors called fanning friction factor f and Colbourn j factor have been developed by investigators.

1.1. Thesis Objective

The main aim of the present study is to experimentally and numerical analyze the OSFs. We tried to focus on issues that are not particularly studied much in the literature. The general geometrical parameters and a photo of OSF are illustrated below in Figure 1.4.

In this thesis, one of the OSFs used in analyses has a code number, 1/8-16.00(D) that was only experimentally performed by Kays and London (1964). The geometrical parameters of it are tabulated in Table 1.1.

The OSF with code number 1/8-16.00(D) will be performed for only numerical analyses. Since one of the aims of this thesis is achieving a numerical model which confirms the results obtained from experimental analyses. For that purpose the numerical model for OSF with code number 1/8-16.00(D) will be used as a guide for modeling of these types of OSFs.

In this thesis, the geometrical parameters of another OSF used in analyses are given in Table 1.2. The OSF will be analyzed for both numerical and experimental analyses. Because the fin has not been analyzed up to now, and no result exists in literature.

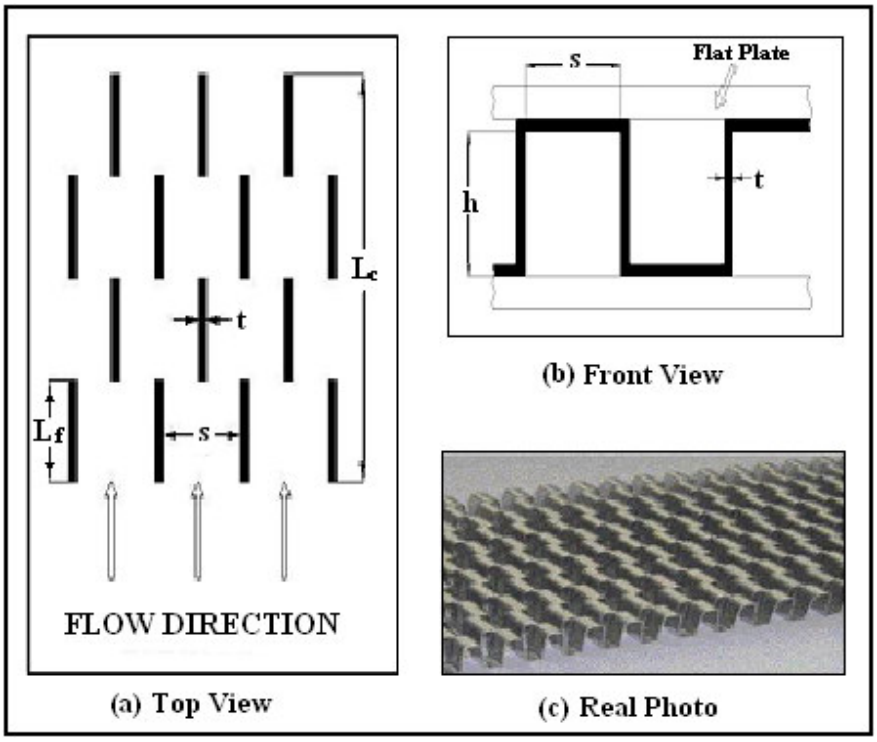

Figure 1.4. General geometrical parameters of OFS.

Table 1.1. Geometrical parameters of OSF with code name1/8-16.00(D).

Geometrical Parameters	Dimensions (mm)
Fin Length (L_f)	3.175
Fin Height (h)	3.006
Fin thickness (t)	0.152
Fin Size (s)	1.434
Channel Length (L_c)	93.25

Table 1.2. Geometrical parameters of second OSF.

Geometrical Parameters	Dimensions (mm)
Fin Length (L_f)	1.5
Fin Height (h)	3.8
Fin thickness (t)	0.2
Fin Size (s)	2.6
Channel Length (L_c)	200

These studied issues are shortly are;

Firstly, working fluid in the reviewed literature was taken mostly as air and its thermo-physical properties were assumed to be constant, especially for numerical analyses. Although, these assumptions may be acceptable for most of the applications of air whose Prandtl number is less than one. On the other hand; for water or another working fluids whose Prandtl numbers are greater than one this situation differs where the thermal properties of the fluid considerably change with temperature. Therefore, the thermo-physical properties are taken as temperature dependent in this study and its effects are discussed.

Secondly, the numerical studies in the literature generally were usually performed for two dimensional cases. However, it is noticed that three dimensional effects are important particularly in short and interrupted fins. Therefore, numerical analysis is conducted in this thesis show a close agreement with the experimental results also points out that 3-D effects are not to be left out in the analysis of this type of exchangers.

Moreover, existed experimental studies in this area are usually assumed that the heat source/sink thermal boundary condition of the heat transfer surfaces as of uniform temperature type. Although, especially in the electronic cooling applications constant heat flux plays an important role and therefore our numerical and experimental studies points out some important differences in heat transfer due to this different boundary condition.

Above mentioned goals are planned to be achieved by the following measurements;

- Determining the average heat transfer coefficient and pressure drop in OSF at different Reynolds numbers,
- Determining the effect of Prandtl number on the heat transfer rate and pressure drop,
- Determining the effects of the two thermal boundary conditions on heat transfer and pressure drop,

CHAPTER 2

LITERATURE SURVEY

Over the past few decades a large amount of study has been conducted to analyze the heat transfer and pressure drop characteristics of compact heat exchangers. Although various types of interrupted fin surfaces have been performed in the past, this study focuses on the offset-strip fin (OSF) type compact heat exchanger. Various similar studies about this type of fin are available in the literature and they will be summarized in this chapter.

Patankar and Prakash (1981) presented a two dimensional numerical analysis for the flow and heat transfer in an interrupted plate passage, which is an idealization of the OSF heat exchanger. The main aim of the study is investigating on effect of plate thickness as a non dimensional form t/H on heat transfer and pressure drop in OSF channels because the impingement region resulting from thick plate on the leading edge and recirculating region behind the trailing edge are absent if the plate thickness is neglected. Their calculation method was based on the periodically fully developed flow through one periodic module because the flow in OSF channels attains a periodic fully-developed behavior after a short entrance region, which may extend to about 5 (at the most 10) ranks of plates (Sparrow, et al. 1977). In the periodic regime the flow repeats itself in an identical manner for successive geometrical modules. The existence of this fully developed periodic regime was first identified in the study of Sparrow, et al. (1977). They assumed the flow as steady and laminar in the Reynolds number ranges from 100 to 2000. Patankar and Prakash (1981), in this range of Reynolds number the real flow is expected to be mostly laminar, although it is possible that transition to turbulence may occur somewhat before the Reynolds number is almost 2000 especially for the higher values of t/H. they also used a constant heat flow boundary condition with additional specification that each row of fins were at a fixed temperature. They made some analysis for different fin thickness ratios t/H= 0, 0.1, 0.2, 0.3 at the same fin length given by L/H=1, and also they fixed the Prandtl number of fluid as 0.7. They also compared their numerical results with available experimental results of Kays and

London (1964). Their numerical results showed that by increasing the non dimensional form of fin thickness at same Reynolds number based on the hydraulic diameter, the flow pattern changes resulting in increasing overall heat transfer also pressure drop. For the lower Reynolds number such as 100 and 500, they observed an impingement flow on the leading edge of the fin and a small recirculation zone behind the trailing edge for the higher Reynolds numbers such as 1000 and 2000, they also observed the recirculating flow fills the space between the trailing edge of one plate and the leading edge of next plate, and the impingement flow disappears. As a result of their investigation it was concluded that the thick plate situation leads to significantly higher pressure drop while the heat transfer does not sufficiently improve despite the increased surface area and increased mean velocity.

Joshi and Webb (1987) developed elaborate analytical models to predict the heat transfer coefficient and the friction factor of the OSF heat exchanger surface geometry. In order to identify the transition from laminar to turbulent flow an equation based on the conditions in the wake was developed by conducting flow visualization experiments.

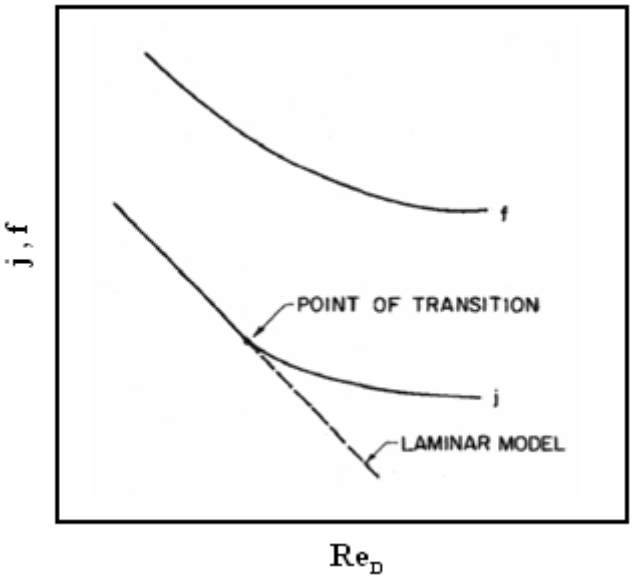

Figure 2.1. Typical j and f characteristics.
(Source: Joshi and Webb 1987)

The condition predicted by transition equation corresponds to onset of oscillating velocities in the fin wakes. Thus they easily defined the laminar, turbulent, and transition regions. They also modified the correlations of Wieting (1975). There are some differences between the correlations. These correlations are based on hydraulic

diameter than that used in the correlations of Wieting (1975) because the area of the fin ends has been included in the study. Using flow visualization four different flow regimes could be identified by Joshi and Webb (1987). In the first regime, the flow was laminar and steady. In the second regime, the oscillating flow structures appeared in the transverse direction. In the third regime, the flow oscillated in the wake region between two successive fins. In the fourth regime, the vortex shedding started to become important. The laminar flow correlation of Joshi and Webb started to under predict the j and f at the second regime. Thus, they assumed the Reynolds number at that point as the critical Reynolds number to identify the transition between laminar and turbulent.

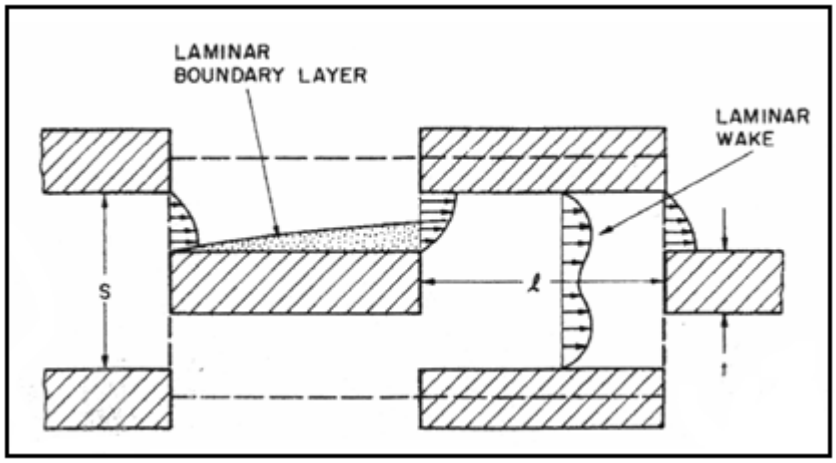

Figure 2.2. Laminar flow on the fins and in the wakes.
(Source: Joshi and Webb 1987)

Kalkar and Patankar (1990) numerically analyzed the fluid flow and heat transfer for a tube with staggered and in-line fins as three dimensional. They observed that the flow shows three-dimensional parabolic behavior because of the repetitive nature of geometry of both staggered and in-line fins in axial direction, so the flow shows periodically repeating behavior after some initial development length. The effects of Prandtl number on the heat transfer and the fluid flow were also investigated. The Prandtl numbers were 0.7 and 5. Their results showed that for Prandtl number of 0.7, a tube with staggered fins supplies less heat transfer enhancement than a tube with in-line fins produces much heat transfer enhancement than tubes with either continuous or staggered fins and also with less pressure drop.

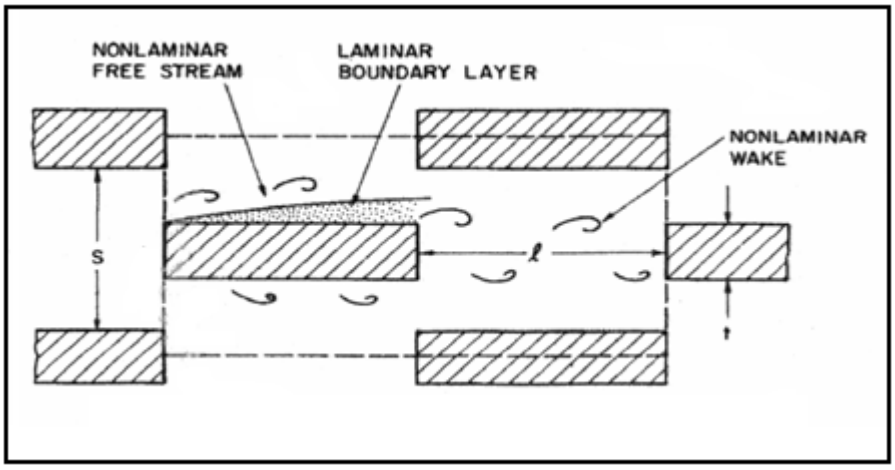

Figure 2.3. Laminar flow on the fins and oscillating flow in the wakes.
(Source: Joshi and Webb 1987)

Maughan and Incropera (1990a) (1990b) studied on mixed convection heat transfer with longitudinal fins in a horizontal parallel plate channel. They presented two papers about the study. In the first paper (Maughan and Incropera 1990a) the numerical results of it was presented although the second study (Maughan and Incropera 1990b) was about experimental results. They made the numerical calculations for laminar region and they assumed that the flow was fully developed. They used two different thermal boundary conditions. The first one was an isothermally heated bottom plate with isothermally cooled top plate. The second one was a uniform heat flux at the bottom surface of plate with adiabatic upper surface of it. The reason of using the different two boundary conditions was that they wanted to analyze the effect of secondary flows on the heat transfer enhancement. Maughan and Incropera emphasized that "traditionally, extended surfaces like fins and ribs have been used to augment heat transfer by adding additional surface area and encouraging mixing; however, mixed convection and buoyancy-driven secondary flows also enhance heat transfer above forced convection levels". The results of the two boundary conditions showed that the secondary flow in the form of longitudinal vortices caused by buoyancy forces increased the heat transfer.

Tinaut, et al. (1992) developed two correlations including heat transfer and flow friction coefficients for OSF and plane parallel plates. He used water for analyzing plane parallel plates and engine oil for OSFs as working fluids in experiments. He got the correlations using standard correlations of Dittus and Boelter, and some expressions

of Sieder and Tale and also Kays and Crawford. In order to check the validation of the correlations proposed in the study the correlations were compared to correlations of Wieting (1975) and also Focke. Generally the expressions done by Tinaut et al. have been found to be acceptable upon comparing the results to data obtained from correlations of other researchers, although there were some differences between them. According to Tinaut the reason of the situation was that "the working fluid used by Wieting was air and that of the present study is engine oil, and the discrepancy could be due to different values of Prandtl number for air and oil."

Manglik and Bergles (1995) reported a most needed comprehensive review of experimental research on OSFs. They studied with eighteen different OSFs an investigated the effects fin geometries as non-dimensional forms of them on heat transfer and pressure drop. After analyzing the effects, they arrived upon two correlations, one for heat transfer and another for pressure drop including all three regions. They also reanalyzed the expressions done by other researchers and described the asymptotic behavior of the data obtained from the correlations in the deep laminar and fully turbulent regimes. These correlations can be acceptable when comparing the results of the expressions to experimental data obtained by Kays and London (1964).

Hu and Herold (1995a) (1995b) presented two papers about the effect of Prandtl number on heat transfer and pressure drop in OSF array. In the first paper Hu and Herold (1995b) experimentally studied on this effect. For that purpose they used seven OSFs having different geometries, and three working fluids having different Prandtl numbers. Also the effect of changing the Prandtl number of fluid with temperature was investigated. In the second paper Hu and Herold (1995a) studied on developing laminar models to predict the heat transfer and pressure drop performance of liquid-cooled OSFs. Thus they studied in the range of Reynolds numbers from 10 to 2000 in both two papers. The result of these two studies showed that the Prandtl number effect has a significant influence on heat transfer in OSF channel. Although it does not have any effect on pressure drop upon comparing the Colbourn J factors and f fanning friction factors.

Zhang, et al. (1997) investigated on the heat transfer enhancement mechanisms for parallel plate fin heat exchangers including inline and staggered array of OSFs. The effect of finite fin thickness was also studied. The study was numerically analyzed as two dimensional. They took into account the time-dependent flow behavior due to vortex shedding by solving unsteady momentum and energy equations. The effect of

vortices, which they are generated at leading edge of the fins and travel downstream along the fin surface, was also researched. Their results showed that only the surface interruption increases the heat transfer because the surface interruptions cause to periodically restart the boundary layers on fin surfaces and bound growing of them so the thermal resistance to heat transfer between fin surfaces and fluid is reduced. On the other hand after a critical Reynolds number the flow becomes unsteady. In this regime vortices play an important role to increase the heat transfer by bringing fresh fluid from the main stream to fin surface. But the swirling flow generated by the vortices near the fin surface increases the skin friction on it thus, pressure drop improves.

Dejong, et al. (1998) presented a complementary experimental and numerical study for flow and heat transfer in OSFs. In the study the surface-average heat transfer and heat transfer and pressure drop, local Nusselt number and skin friction coefficients on fin surface, instantaneous flow structures, and local time-averaged velocity profiles in OSF channel were investigated. In order to explain the instantaneous flow structures flow visualization method were used and they were compared with numerical results, and also they compared their experimental and numerical results with experimental results obtained by Dejong and Jaccobi (1997) and unsteady numerical simulation of Zhang, et al. (1997). Their results showed that the three-dimensional flow becomes significant when the Reynolds numbers are greater than about 1300, and the thermal boundary conditions are significant when the Reynolds numbers become lower than 1000. Thus they implied that" the results indicate that boundary layer development, flow separation and reattachment, wake formation, and vortex shedding are all important in this complex geometry".

Saidi and Sudden (2001) investigated on numerical analysis of the instantaneous flow and heat transfer for OSF geometries in self-sustained time-dependent oscillatory flow. The effect of vortices over the fin surfaces on heat transfer was also studied at intermediate Reynolds numbers where the flow remains laminar, but unsteadiness and vortex shedding tend to dominate. The obtained numerical results were compared with previous numerical and experimental data done by Dejong, et al. (1998).

Comini, et al. (2004) worked on the illustration of modeling procedures for wavy channel, ribbed channel and offset strip channel. The geometries were made up of the repetition of identical modules. Because of the geometries of channels after a short distance from the entrance, flow and thermal fields repeated themselves from module to module attaining a fully developed character. In this context, Comini et al. made an

assumption that the repeatitive fields allowed the limitation of the analysis to a single module so, he defined periodic boundary condition. Assuming the thermo-physical properties of the fluid to be constant and the flow to be laminar, the governing equations were the standard Navier-Stokes and continuity equations. In the absence of volumetric heating and neglecting the effects of viscous dissipation, the energy equation was solved. His results showed that the surface interruptions bound the growth of boundary layers and cause periodical restarts. At low Reynolds numbers, the flow is regular and steady such as in flat channels. However, in this study, he got substantial increases in both the pressure drop and heat transfer rate with respect to flat channels, because of the restarting of boundary layers. And high Reynolds numbers the flow became unsteady because of transverse vortices, generated at the leading edges; these vortices bring fresh fluid from the main stream to the surface and, consequently, further enhance the local heat transfer coefficients.

It is easy to get information about the effects of OSFs on heat transfer and pressure drop studied by a few researchers such as Patankar and Prakash (1981), Kays and London (1964). But the researchers did not take account the manufacturing irregularities such as burred edges, bonding imperfection, separating plate roughness which is also influence on the heat transfer and flow, and material and brazing having the direct effect on the manufacturing irregularities. So, Dong, et al. (2007) thought that making experiments and analysis again had been necessary to get better thermal hydraulic performance of the OSFs. Thus, the aim of this paper was reanalyzing of the OSF heat exchangers. Sixteen types of OSFs and flat tube heat exchangers were used to make the experimental studies on the heat transfer and pressure drop characteristics. A lot of tests were made by changing fin parameters including fin space s, fin height h, fin thickness t, fin length l and flow length d. And these tests were conducted in specific region of air-side Reynolds number 500–7500, and at a constant water flow rate. The thermal performance data were analyzed using the effectiveness- Number of Transfer Units Method (NTU) in order to obtain the heat transfer coefficient. The heat transfer coefficients and pressure drop data, which were analyzed with different fin space, fin height, and fin length, were related with the inlet air velocity. The general correlations for Colburn j-factor and Fanning fraction f-factor were derived by using regression analysis and F-test. Geometry parameters of all OSFs were converted as non-dimensional format to be able to compare the experimental and analytical results easily. All tested OSFs were checked before brazing. As a result, the heat transfer coefficient

and pressure drop with different fin spaces, fin heights and fin length are the functions of the velocity while other geometrical parameters are same. Heat transfer coefficient and pressure drop reduce with enlarging fin space, fin height and fin length. Because of the fact that the air velocity increases in smaller fin passage which makes the boundary layer thickness smaller. At the same time, the effect of the finite fin thickness becomes obvious, which means that the eddy and vortex shedding start.

OSF heat exchangers are used in a variety of applications and these exchangers are usually operated at low Reynolds numbers because increasing Reynolds number causes the pressure drop to improve. However most of the studies were performed at low Reynolds numbers to avoid the pressure drops, a research was operated at higher Reynolds numbers, where the heat transfer rate increases due to the vortex shedding and turbulent flow, by Michna, et al. (2005) The study was conducted at Reynolds numbers between 5000 and 120 000. As expected, both the pressure drop and the heat transfer coefficient increased with improving Reynolds number because of growing of the vortex shedding and eddy at turbulent regime. Operation of the OSF heat exchangers under these Reynolds numbers may be useful in such systems that minimizing heat exchanger size or maximizing the heat transfer coefficient is more important than minimizing the pressure drop.

Muzychka and Yovanovich (2001a) (2001b) presented two comprehensive studies on OSFs. Also the researchers first attempted to separate the OSF studies into two categories according to fluid flow orientations, one study was about the Low Pressure Direction (LPD) where the fluid flows parallel to the fin surfaces like previous studies done by other researchers; another study was about High Pressure Direction (HPD) type where the fluid impinges on the fin surfaces as shown in Figure 1.

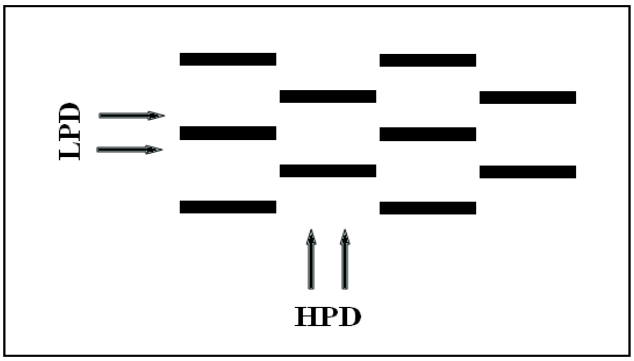

Figure 2.4. Flow orientation definition for OSFs.
(Source: Guo et al. 2007)

In the first study on LPD type OSFs (Muzychka and Yovanovich 2001a), they performed to develop analytic models in order to predict the thermal hydraulic characteristics of OSF arrays. The analytical models were based on Wieting (1975) and Joshi and Webb (1987), but much simpler than them. They also compared the results obtained from the correlations with the experimental data obtained by Kays and London (1964), and with their own experimental data, and also the data obtained from the correlations of Manglik and Bergles (1995). As a result of the study it is concluded that the models developed by Muzychka and Yovanovich were in correlation with the experimental data and also the data presented by Kays and London (1964) at the all range of Reynolds numbers although there are some differences between the data obtained from the correlations of Manglik and Bergles (1965). In the second study including HPD type OSFs (2001b) they created new analytical models to get the thermal hydraulic performances of transverse flow through on HPD type OSF arrays. They made new experimental analysis for ten OSF configurations to compare the experimental results with the data obtained from new correlations. Their results showed that the model predictions almost found to be in correlation with experimental data. It is also worthwhile to emphasize that the HPD type OSFs supply much greater heat transfer and friction loss than LPD type OSFs. The main possible reason may be that the staggered surfaces of the HPD type OSFs interrupt flow and thermal boundary layers much more strenuously than the LPD type ones.

Guo, et al. (2007) (2008) presented two papers including the HPD type OSFs. In the first study (Guo, et al. 2008) he developed empirical correlations for the HPD type OSFs. He used thirty-six OSFs having different geometries to get the expressions. The material of OSFs were steel although Muzychka and Yovanovich (2001a) (2001b) who first attempted to identify the correlations for HPD type fins used brass and aluminum OSFs in their experiments. Thus, these two studies presented by different researchers can be important for understanding the thermal behaviors of the flow upon taking into consideration the material differences. He examined the effects of geometrical factors of HPD type OSF on heat transfer and pressure loss. He compared the data obtained from correlations with his experimental results and also the data obtained from the correlations of Muzychka and Yovanovich (2001a) (2001b). His results showed that their correlations agree with the experimental data but not agree with the data obtained from the correlations of Muzychka and Yovanovich when the Colbourn j factor was taken into consideration. The reason may be the materials having different thermal

conductivity. In the second paper Guo, et al. (2007) wanted to supply comprehensive study on HPD type steel OSFs. In this study the effects of mould wear and also the geometrical irregulaties resulted from manufacturing differences on thermal hydraulic performance were investigated. He explained the reason as that " however, as a result of manufacturing difference between the 'soft' materials of aluminum or brass and 'hard' material of steel, it is not practical to get the general heat transfer and flow friction models applied to all OSFs made of different materials, even made of the same material but different manufacturing technologies". Manglik and Bergles (1995) emphasized the same situation that manufacturing irregulaties such as burred edges, bonding imperfections and separating plate roughness affect the flow behavior on heat transfer in actual heat exchanger cores.

Of above mentioned there are too many correlations for heat transfer and pressure drop characteristics obtained by lots of researchers. The reason of developing the predictive equations is that generally in most heat exchanger problems the working fluid, the heat flow rate and mass flow rate are usually known. If certain correlations between geometry and fin performance is also known, then the problem can be greatly simplified. For that purpose developing the two correlation factors called fanning friction factor *f* and Colbourn *j* factor are important for heat exchanger designers. Some of The correlations and their investigators are given in Table1. Generally the correlations include three distinct non-dimensional ratios depending on OSF geometry. These are the ratio of free flow area ($\alpha = s/h$), the ratio of heat transfer area ($\delta = t/\ell$), and the ratio of fin density ($\gamma = t/s$). The correlations depending on these non-dimensional ratios are tabulated in the Table 2.1.

In this thesis the correlations of Manglik and Bergles (1995) will be used to compare with the numerical and also experimental results of the considered problem.

Table 2.1. Chronological listing of the correlations for OSF channels.

INVESTIGATOR(s)	CORRELATION
Manson	$j = \begin{cases} 0.6(l/D_h)^{0.5}\,Re^{0.5}, & l/D_h \le 3.5 \\ 0.321\,Re^{0.5}, & l/D_h > 3.5 \end{cases}$ For Re < 3500: $f = \begin{cases} 11.8(l/D_h)\,Re^{0.67}, & l/D_h \le 3.5 \\ 3.371\,Re^{0.67}, & l/D_h > 3.5 \end{cases}$ For Re > 3500: $f = \begin{cases} 11.8\,(l/D_h)Re^{0.67}, & l/D_h \le 3.5 \\ 3.371Re^{0.67}, & l/D_h > 3.5 \end{cases}$ Where $D_h = 2sh/(s+h)$
Kays	$j = 0.665Re_{\ell}^{-0.5}$ $f = 0.44\,(t/l) + 1.328Re_{\ell}^{-0.5}$
Wieting	Re < 1000: $j = 0.483(l/D_h)^{-0.162}\,\alpha^{-0.184}\,Re^{-0.536}$ $f = 7.661(l/D_h)^{-0.384}\,\alpha^{-0.092}\,Re^{-0.712}$ Re > 2000: $j = 0.242(l/D_h)^{-0.322}\,(t/D_h)^{0.089}\,Re^{-0.368}$ $f = 1.136(l/D_h)^{-0.781}\,(t/D_h)^{-0.534}\,Re^{-0.198}$ Where $D_h = 2sh/(s+h)$
Joshi and Webb	Re < Re* $j = 0.53Re^{-0.5}\,(l/D_h)^{-0.15}\,\alpha^{-0.14}$ $f = 8.12Re^{-0.74}\,(l/D_h)^{-0.41}\,\alpha^{-0.02}$ Re > Re* + 1000 $j = 0.21Re^{-0.4}\,(l/D_h)^{-0.24}\,(t/D_h)^{0.02}$ $f = 1.12Re^{-0.36}\,(l/D_h)^{-0.781}\,(t/D_h)^{0.17}$ Where $D_h = 2(s-t)h/[(s+h)+th/l]$ and $Re^{*} = 257\left(\frac{l}{s}\right)^{1.23}\left(\frac{t}{l}\right)^{0.58} D_h\left[t + 1.328\left(\frac{Re}{l\,D_h}\right)^{-0.5}\right]^{-1}$
Mochizuki et al.	Re < 2000 $j = 1.37(l/D_h)^{-0.25}\,\alpha^{-0.184}\,Re^{-0.67}$ $f = 5.55(l/D_h)^{-0.32}\,\alpha^{-0.092}\,Re^{-0.67}$ Re > 2000 $j = 1.17(l/D_h + 3.75)^{-t}\,(t/D_h)^{0.089}\,Re^{-0.36}$ $f = 0.83(l/D_h + 0.33)^{-0.5}\,(t/D_h)^{0.534}\,Re^{-0.20}$ Where $D_h = 2sh/(s+h)$
Manglik and Bergles	$j = 0.6522Re^{-0.5403}\,\alpha^{-0.1541}\,\delta^{0.1499}\,\gamma^{-0.0678}$ $\times\left[1 + 5.269\times10^{-5}Re^{1.340}\,\alpha^{0.504}\,\delta^{0.456}\,\gamma^{-1.055}\right]^{0.1}$ $f = 9.6243Re^{-0.7422}\,\alpha^{-0.1856}\,\delta^{0.3053}\,\gamma^{-0.2659}$ $\times\left[1 + 7.669\times10^{-8}\,Re^{4.429}\,\alpha^{0.920}\,\delta^{3.7676}\,\gamma^{0.236}\right]^{0.1}$ Where $D_h = 4shl/2[(sl + hl + th) + ts]$

CHAPTER 3

NUMERICAL ANALYSIS

3.1. Introduction to Computational Fluid Dynamics

Computational Fluid Dynamics (CFD) means predicting fluid flows and heat transfer using computational methods. CFD is based on various disciplines of science such as mathematics, computer engineering and physics to provide meaningful modeling of fluid flows. CFD is primarily concerned with numerical solutions of differential equations such as conservation of mass, momentum, and energy in moving and deforming fluids.

CFD is used in an extremely wide range of industries. Any industrial process that involves fluid flow and/or heat transfer can benefit from it. For example, such list of industrial and/or academic areas is;

- Aerospace: Aerodynamics, wing design, missiles, passenger cabin
- Automotive: Internal combustion, underbody, passenger comfort
- Biology: Study of insect and bird flight
- Building: Clean rooms, ventilation, heating and cooling
- Civil Engineering: Design of bridges, building exteriors large structures
- Chemical Process: Static mixing, separation, reactions
- Electrical: Equipment cooling
- Environmental: Pollutant and effluent control, fire management, shore protection
- Marine: Wind and wave loading, sloshing, propulsion
- Mechanical: Pumps, fans, heat exchangers
- Meteorology: Weather prediction
- Oceanography: Flows in rivers, estuaries, oceans
- Sports Equipment: Cycling helmets, swimming goggles, golf balls
- Turbomachinery: Turbines, blade cooling, compressors, torque convertors

A variety of reasons can be cited for the increased importance that simulation techniques have achieved in recent years (Löhner 2008);

- The need to forecast performance. The inability to forecast accurately the performance of a new product can have a devastating effect on companies. The only way to minimize the risk of unexpected performance is through insight information. Simulation techniques such as CFD can provide this information.
- Cost of experiments. Experiments, the only other alternative to simulations, are very costly.
- Impossibility of experiments. In some instances, experiments are impossible to conduct. Examples are atmospheric nuclear explosions or biomedical situations that would endanger the patient's life.
- Insight. Most large-scale simulations offer more insight than experiments. A mesh of 1×10^6 grid points is equivalent to an experiment with 1×10^6 probes or measuring devices. Moreover, many derived properties (e.g. vorticity, shear, residence time, etc.) can easily be obtained in a simulation, but may be unobtainable in experiments.
- Computer speed and memory. Computer speed and memory capacity continue to double every 18 months. At the same time, algorithm development continues to improve accuracy and performance. So, more realistic simulations can be performed.

CFD codes are structured around the numerical algorithms that can deal with the fluid flow problems. The CFD codes contain essentially three main stages;

1. ***Pre-processor***: Pre-processing means creating a representative model of flow problem before numerical solution process. This part also consists of some necessary inputs of the flow problem given by the analyzer and these inputs are transformed to the solver. At the pre-processor stage, the following activities are performed by the analyzer (Versteeg and Malalasekera 1995);

- Definition of the geometry of the region of interest: the computational domain.
- Grid-generation – the subdivision of the domain into a number of smaller, non-overlapping sub-domains: a grid (or mesh) of cells (or control volumes or elements).
- Selection of the physical and chemical phenomena that need to be modeled.
- Definition of fluid properties.
- Specification of appropriate boundary conditions at cells which coincide with or touch the domain boundary.

In the pre-processor part the number of elements or cells in a domain play important roll for the accuracy of the CFD solution of the fluid problem. The accuracy of a CFD solution is governed by the number of cells in the grid. In general, the larger number of cells the better solution accuracy. However, more cells also cause longer computational time and need more powerful computer hardware. Thus, the cells in a grid should be created at optimum level to obtain physically realistic results in a meaningful time.

2. ***Solver:*** There are three different streams of numerical solution techniques. These are finite difference or finite volume method (FVM) which is another special form of finite difference, finite element and spectral methods. The problem under consideration was solved by using FVM solution techniques. In a general manner the numerical methods that form the basis of the solver perform the following steps (Versteeg and Malalasekera 1995):

- Approximation of unknown flow variables by means of simple functions.
- Discretisation by substitution of the approximations into the governing flow equations and subsequent mathematical manipulations.
- Solution of the algebraic equations.

Briefly the main differences between the three methods are associated with the way in which flow variables such as velocity, pressure etc. are approximated and with the discretisation of governing equations including continuity, momentum and energy equations.

3. ***Post-processor***: This is the final step in CFD analysis, and it involves the organization and interpretation of the predicted flow data and production of CFD images and animations. At the post-processor stage, the CFD images obtained from predicted flow data can include (Versteeg and Malalasekera 1995);

- Domain geometry and grid display.
- Vector plots.
- Line and shaded contour plots.
- Particle tracking.
- View manipulations (translation, rotation, scaling etc.)
- Color postscript output.

3.2. Description of the Problem and Geometry

In the present thesis, a cold plate type heat exchanger including offset-strip fin (OSF) is investigated numerically and also experimentally. Numerical part of this study is performed due to the fact that detailed information about the heat transfer may be obtained provided that the computational model is accurate. On the other hand, experimental analyses are used to ensure the accuracy of numerical results. As a result of these facts, if the results of the experimental analysis are confirmed by the numerical ones, then a heat exchanger can safely be analyzed by using the numerical model created in the present thesis. The cold plate type heat exchanger used for the experimental analysis is illustrated in Figure 3.2.1.

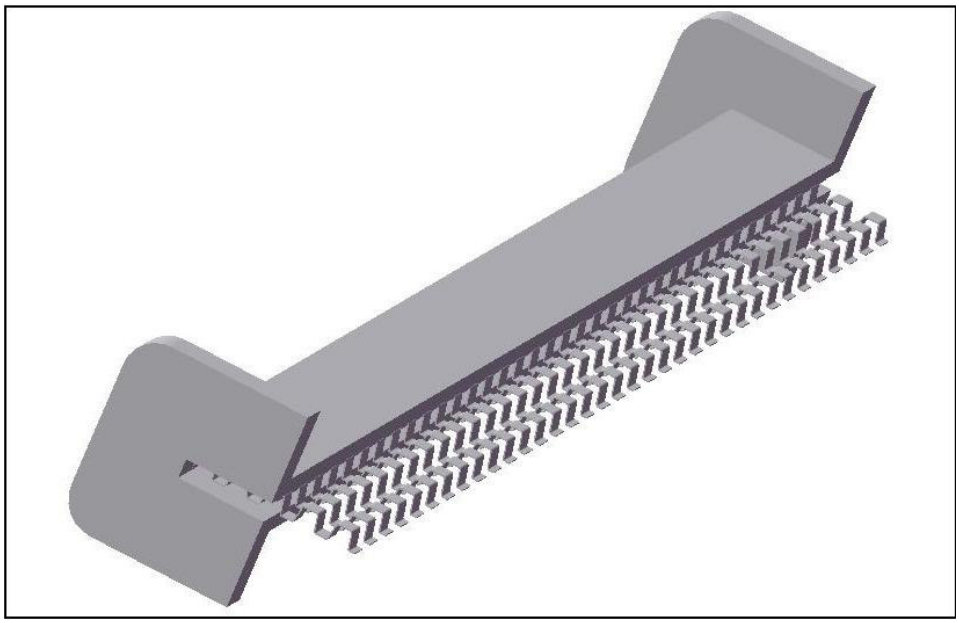

Figure 3.1. View of the cold plate type heat exchanger under analysis.

As it can be seen from Figure 3.1, the working fluid enters the heat exchanger, and flows through the OSF channels. The flowing fluid absorbs the heat from the fin walls where heat sources are at bottom and top side of cold plate. The cold plate heat exchanger is used also for experimental analysis consists of 5 modules in the spanwise direction and 134 modules along the flow direction. The OSF used in the heat exchanger is illustrated in Figure 3.2.

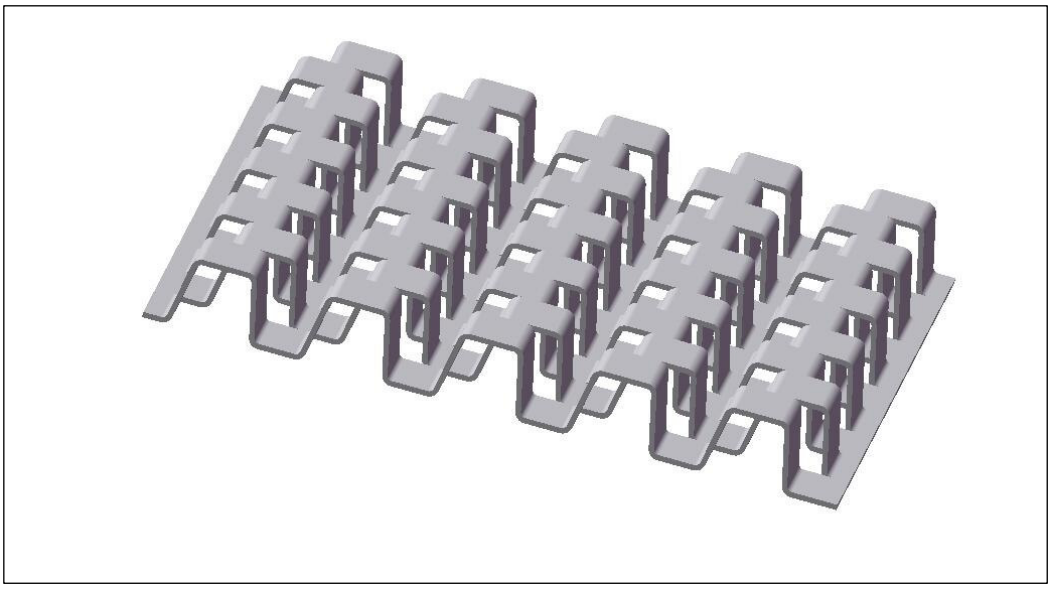

Figure 3.2. The offset-strip fin used in the heat exchanger.

For the considered heat exchanger problem (including an OSF) some assumptions and simplifications for geometry are performed in order to ease computational burden. Otherwise, the capability of computer hardware such as CPU, RAM etc. could not be enough to handle such a complicated geometry. First simplification is that the one module, which is the middle row in span-wise direction, of OSF along to flow direction is isolated for computational analysis since it is representative enough for the whole geometry because of the symmetrical nature of all heat exchangers as shown in Figure 3.3.

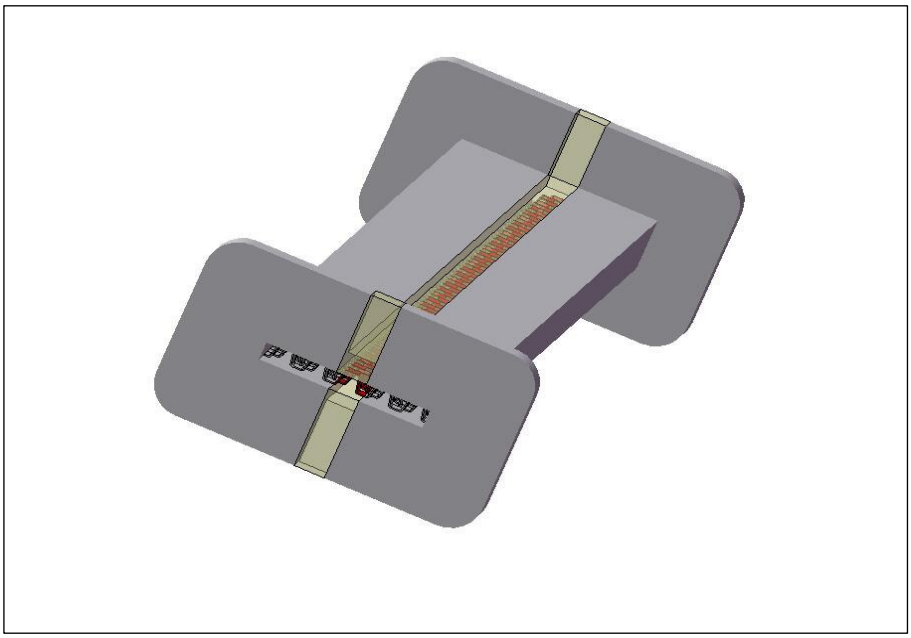

Figure 3.3. The first geometrical assumption of the heat exchanger problem.

Secondly, the 30 rows along the flow direction are found to be enough to numerically analyze the OSF because it is seen in the literature that the flow in OSF channels attains fully-developed behavior after a short distance from entrance region, which may extend to about 5 (at the most 10) rows of plates (Patankar and Prakash 1981, Dejong and Jacobi 1998). For that purpose 30-row-OSF channel is chosen in order to decrease the effects of the entrance region or hydro-dynamically developing region.

Thirdly, the OSF fin has trapezoidal shape and had radiuses at top and bottom corners. The fin shape and radiuses increase the mesh numbers and also computational time. So in this thesis one more assumption is made that the fins could be assumed as rectangular shape if the fin size is equal to average of fin sizes of bottom and top sides of the fin as shown in Figure 3.4.

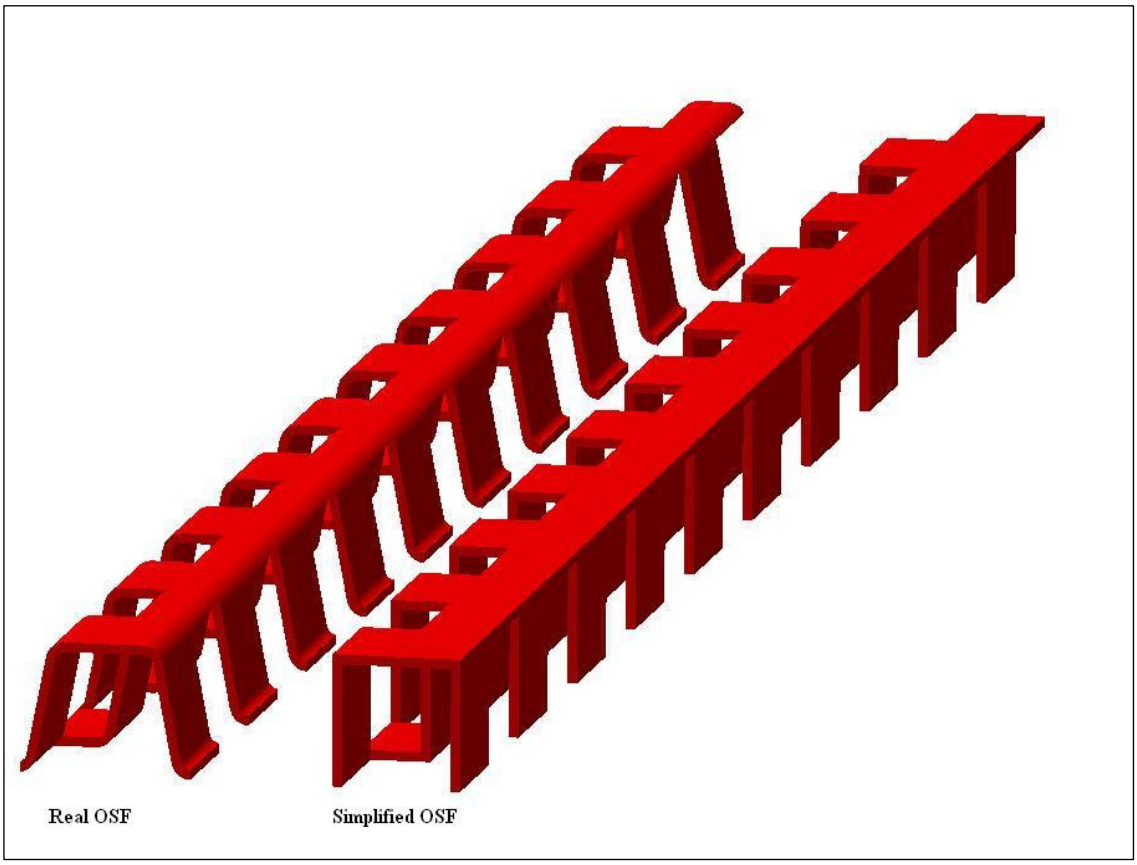

Figure 3.4. Making rectangular OSF

The fins and the cold plate heat exchanger are made of 6061-T6 alloy of aluminum because of its good thermal conductivity and excellent brazebility. Assuming that the thermal resistance between the contacting walls of heat source and the fins are very low because of high brazing quality, and the fin thickness of OSF walls is very thin, 0.2 mm, then, the fin walls touching with the bottom and top side of the OSF channels can be negligible in order to simply the numerical geometry. The OSF with and without ignoring top and bottom walls are illustrated in Figure 3.5.

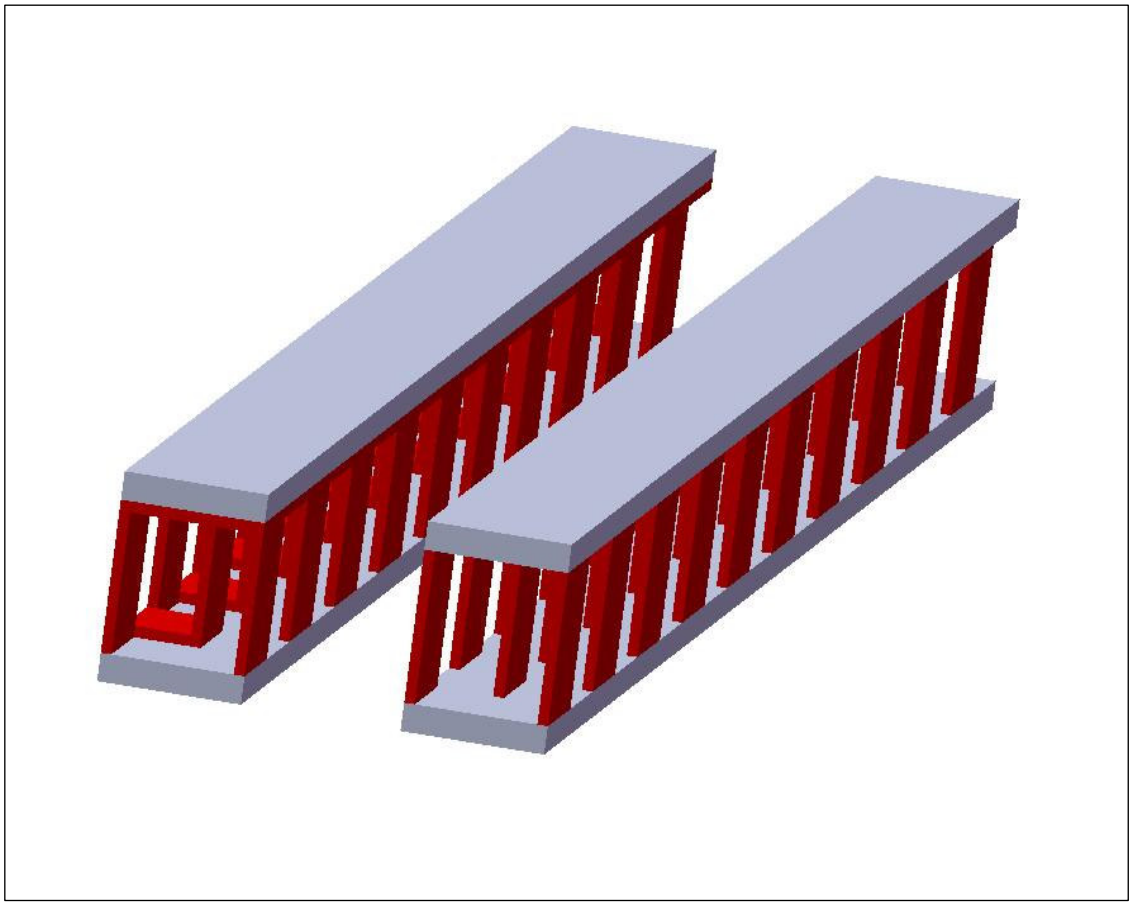

Figure 3.5. The OSF with and without ignoring fin walls.

The physical behavior of fluid in OSF channels and their geometry allow us to divide the domain into two parts by using symmetry plane at the middle of the considered cold plate heat exchanger and it is parallel to top and bottom walls of the OSF channels as shown in Figure 3.6.

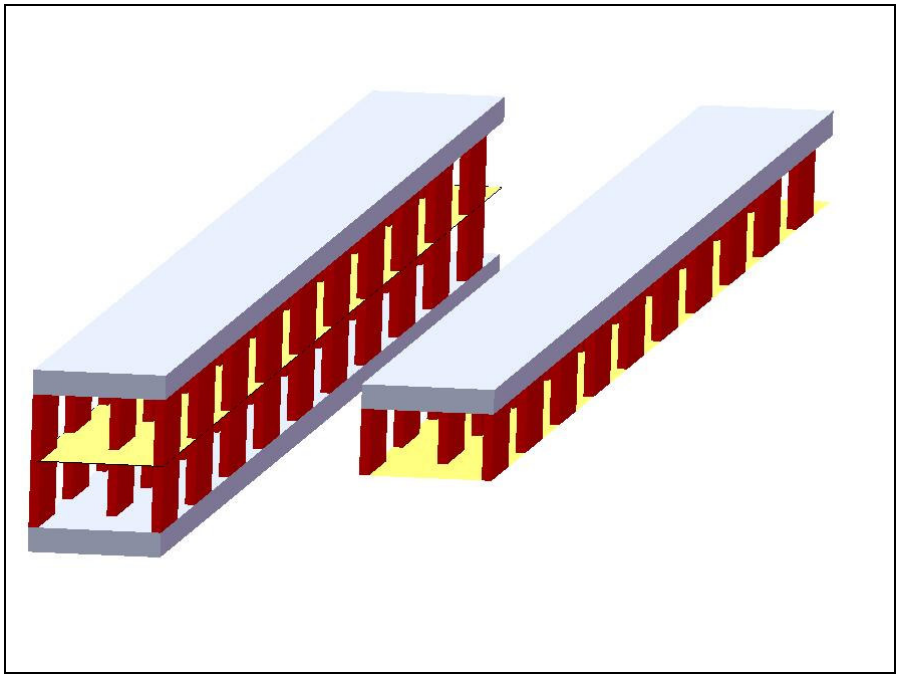

Figure 3.6 Half part of the problem.

Another simplification of the geometry is that the dividing the half part of the heat exchanger is also separated into two pieces by using another symmetry plane at the middle of the considered heat exchanger and it is perpendicular to previous symmetry plane as shown in Figure 3.7.

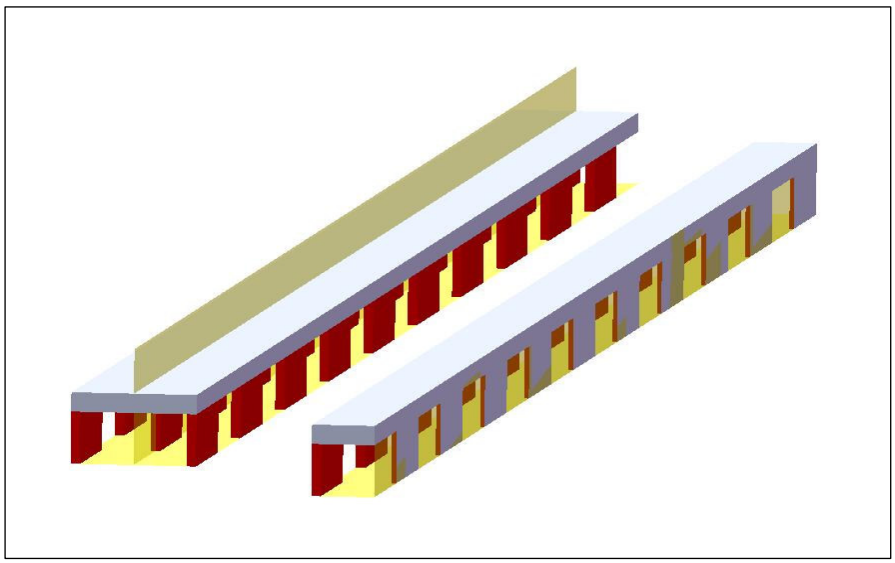

Figure 3.7. Quarter part of the problem.

In this thesis the last two geometries of considered problem of cold plate heat exchanger with OSF are both used in numerical analysis. The half part domain is used for unsteady analysis because the flow in OSF channels shows unsteady flow motion after a critical Reynolds number. The oscillating flow structures resulting from unsteady flow appear in the transverse direction and the oscillation flow does not show symmetrical behavior. Quarter part of the considered problem is used for steady–state problem because the physical behavior of the mean flow and geometry are symmetrical according to the perpendicular plane as shown above in Figure 3.7.

3.3. Material Properties

3.3.1. Thermo-physical Properties of Aluminum

The materials of OSF channels and also the cold plate heat exchanger are 6061-alloy of aluminum because of its good thermo-physical characteristics and small density and relatively low price. Following constant thermo-physical properties of aluminum are used in the numerical calculations (Shah and Sekulic 2003);

$$\rho_{Al} = 2719 \quad kg/m^3 \tag{3.1}$$

$$C_{p_{Al}} = 871 \quad j/kgK \tag{3.2}$$

$$k_{Al} = 202.4 \quad W/mK \tag{3.3}$$

3.3.2. Thermo-physical Properties of Working Fluids

One of the important steps in the set up of the numerical model is the definition of the physical properties of materials. Since for the solid materials only conduction equations are solved for the steady state problem, therefore only the thermal conductivity value is required as a property of the medium. On the other hand, for the fluid domains, properties including density, viscosity, thermal conductivity and specific heat capacity are required for the calculation purposes. The physical properties can be assumed as dependent or independent of temperature. When there is a large temperature difference between the fluid and the surface the assumption of constant thermo-physical fluid properties may cause some errors, because in reality the thermo-physical properties of the most of the fluids vary with temperature. It is also important to note that the Prandtl number of liquids also varies with temperature, similar to that of viscosity. These property variations, of course, will affect the velocity and the temperature profile of fluid in the channel. Since we aimed to show a comparison of numerical data with experimentally analysis, the thermo-physical properties of working fluids are assumed as temperature dependent throughout this thesis.

There are three working fluids used in this thesis. Those are air, water, and ethylene-glycol. Since variation of the temperature along the channel is considered to be influencing the thermo-physical properties, algebraic equations are derived as a function of temperature by the method of curve fitting from the data obtained from references within a certain temperature range. The simple form of the polynomial functions is in the following form

$$f(T) = A_1 + A_2T + A_3T^2 + \ldots \tag{3.4}$$

where f is a thermo-physical property and T is in Kelvin's.

The equations obtained for a temperature range of 273.15 – 373.15 K are given below in Equations 3.5 to 3.16 and graphs are provided in Figures 3.8-3.10 (Çengel and Cimbala 2006).

➢ For Air

- Thermal Conductivity [W/mK]

$$k\,(T) = -5e\text{-}08T^2 + 10731.5e\text{-}08T - 148254.6125e\text{-}08 \qquad (3.5)$$

- Density [kg/m^3]

$$\rho\,(T) = 0.00001T^2 - 0.009963T + 3.277 \qquad (3.6)$$

- Dynamic Viscosity [kg/ms]

$$\mu\,(T) = -4e\text{-}11T^2 + 7085.2e\text{-}11T + 86421.31e\text{-}11 \qquad (3.7)$$

- Specific Heat Capacity [j/kgK]

$$Cp\,(T) = 0.0004T^2 - 0.20222T + 1031 \qquad (3.8)$$

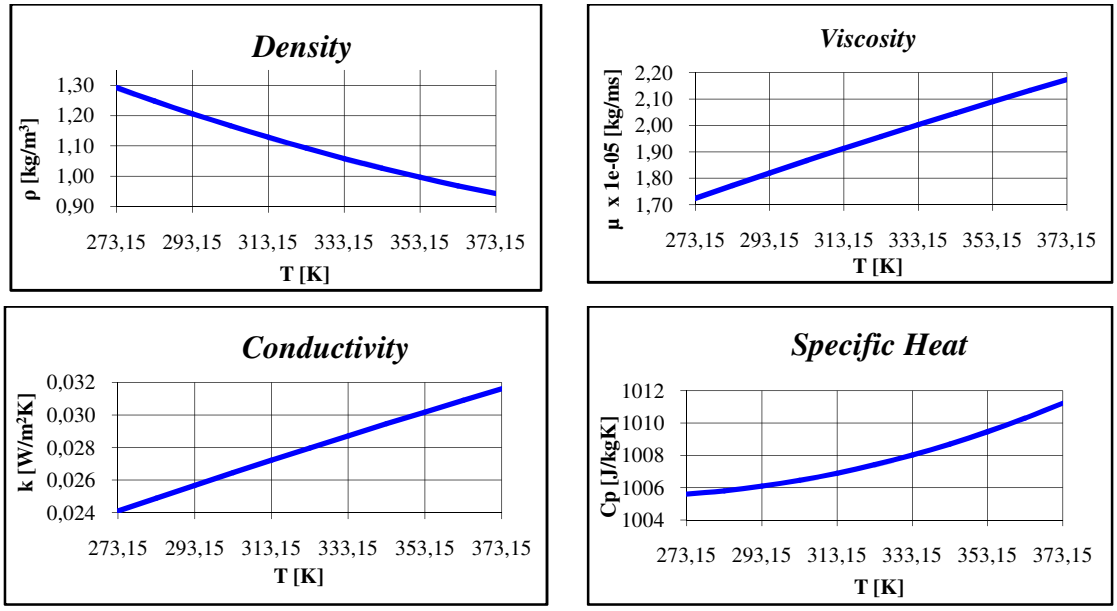

Figure 3.8. Variation of thermo-physical properties of air.

➢ For Water

- Thermal Conductivity [W/mK]

$$k\,(T) = -7e\text{-}06T^2 + 5.6241e\text{-}03T - 0.44215 \quad (3.9)$$

- Density [kg/m^3]

$$\rho\,(T) = 6e\text{-}06T^3 - 942e\text{-}06T^2 + 3.755T - 554.91 \quad (3.10)$$

- Dynamic Viscosity [kg/ms]

$$\mu\,(T) = -2e\text{-}09T^3 + 0.0211e\text{-}04T^2 - 7.4514e\text{-}04T + 885.82e\text{-}04 \quad (3.11)$$

- Specific Heat Capacity [j/kgK]

$$C_p\,(T) = 3e\text{-}06T^4 - 3.978e\text{-}03T^3 + 1.9825T^2 - 440.1033T + 40776.983 \quad (3.12)$$

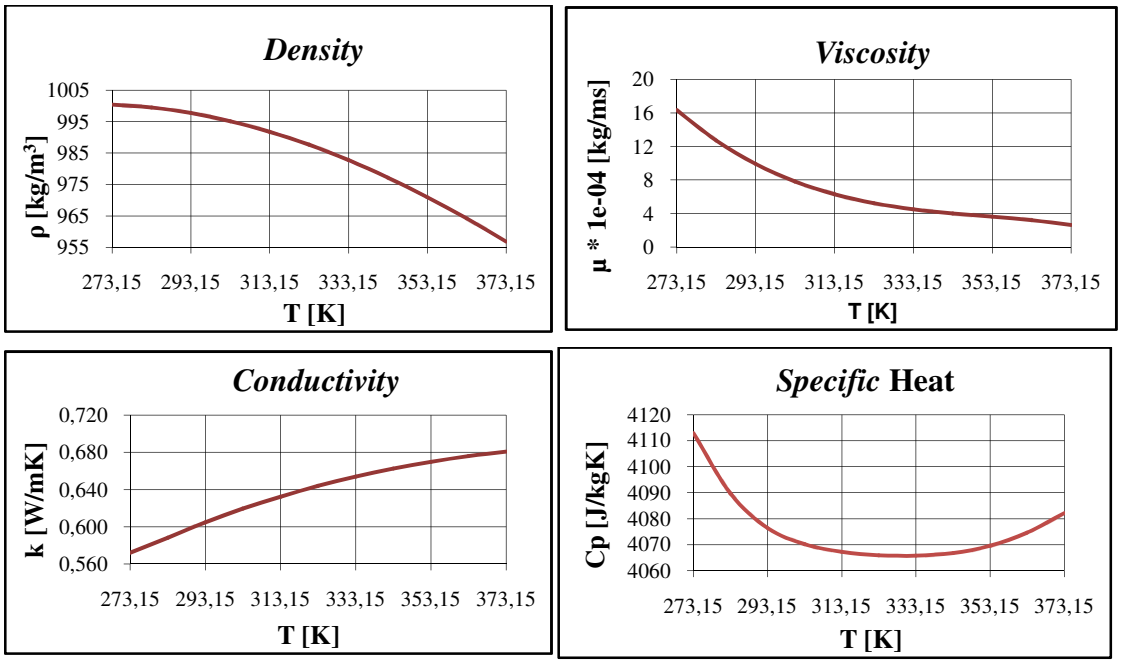

Figure 3.9. Variation of thermo-physical properties of water.

➢ For Ethylene – Glycol

- Thermal Conductivity [W/mK]

$$k\,(T) = -2e\text{-}06T^2 + 0.0017T - 0.0781 \qquad (3.13)$$

- Density [kg/m^3]

$$\rho\,(T) = 0.002T^2 - 0.80866T + 1335.3295 \qquad (3.14)$$

- Dynamic Viscosity [kg/ms]

$$\mu\,(T) = -4e\text{-}08T^3 + 43.778e\text{-}06T^2 - 1602.27e\text{-}05T + 1.964 \qquad (3.15)$$

- Specific Heat Capacity [j/kgK]

$$C_p\,(T) = 4.4183T + 1092.3 \qquad (3.16)$$

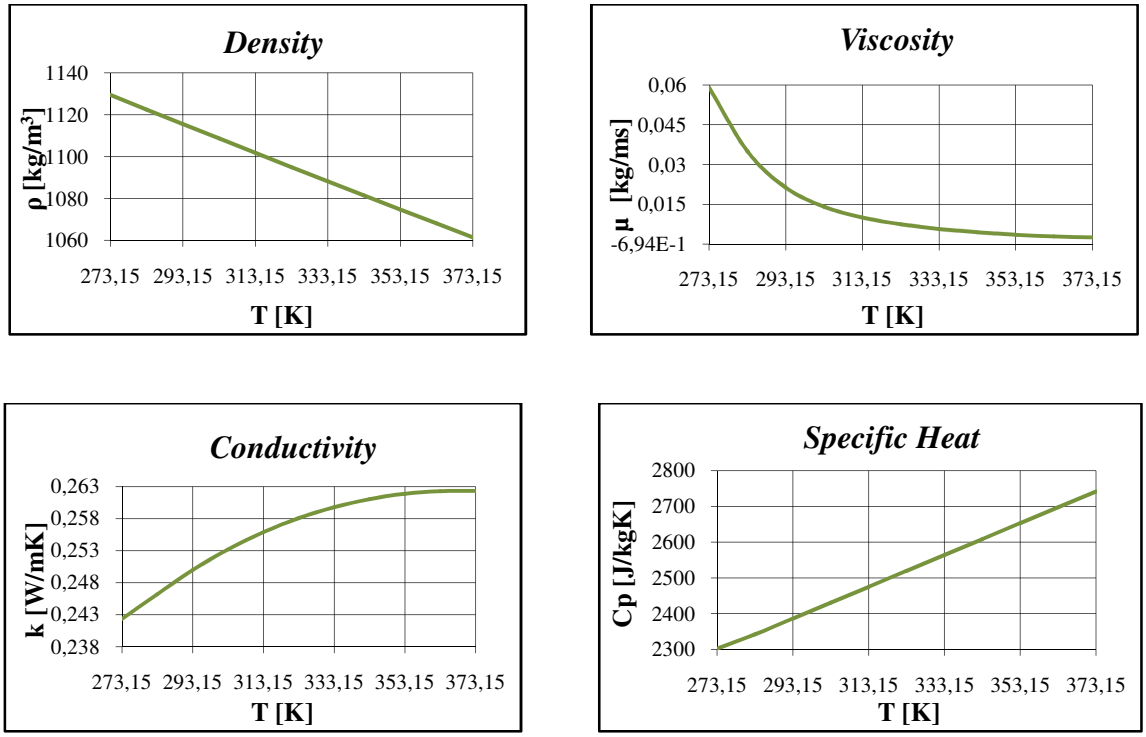

Figure 3.10. Variation of thermo-physical properties of ethylene-glycol.

3.4. Boundary Conditions

In order to solve the numerical problem, some boundary conditions depending on the physical model under investigation should be given. It is important to emphasize that these conditions must be defined carefully so that they are meaningful physically, because the calculation starts from those boundary nodes. The unknown interior node values of the computational domain are solved using the boundary conditions by an iterative manner.

As a result, the computational model of the cold plate heat exchanger consist of one fin volume with half fin thickness, one plate volume and one fluid volume. The schematic view of models of the cold plate heat exchanger under consideration is illustrated in Figure 3.11.

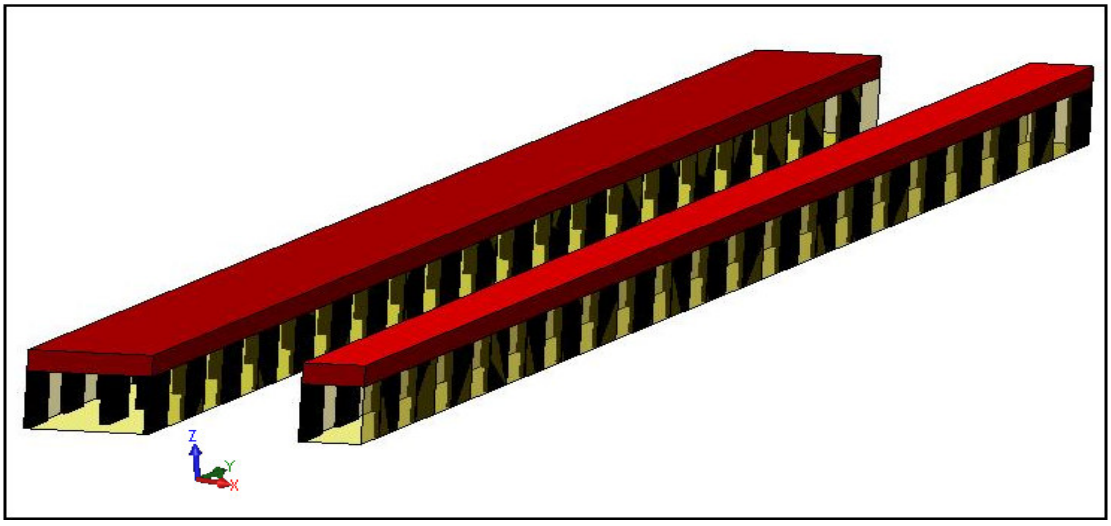

Figure 3.11. Schematic view of the cold plate heat exchanger

3.4.1. Inlet Boundary Condition

Velocity is defined as inlet boundary condition for the surface which is shown in Figure 3.12 as (1). The uniform velocity value is calculated from Reynolds number based on hydraulic diameter of OSF cannel and the viscosity at constant temperature of

300 K. Note that the viscosity of the working fluids is temperature dependent; therefore only an approximate Reynolds number is known at the beginning. Hence the first calculated velocity value is only used as initial guess value. $\boldsymbol{u_i}$ is the tensor notation of velocity vector of the fluid and it has three components for Cartesian coordinate, one in x direction (u_1=$\boldsymbol{u}$), one in y direction (u_2=$\boldsymbol{v}$) and one in z direction (u_3=$\boldsymbol{w}$). So $\boldsymbol{u_i}$ can also be written as;

$$u_i = u\vec{i} + v\vec{j} + w\vec{k}$$

The boundary conditions for this inlet surface can be listed as;

$$u = 0,\ w = 0,\ v = \text{defined value (m/s)} \tag{3.17}$$

$$T|_{inlet} = 300\ \text{K} \tag{3.18}$$

for turbulent flow, extra two boundary conditions should be given as;

$$\boldsymbol{k}\ |_{inlet} = 1\ [m^2/s^2],\ \boldsymbol{\varepsilon}|_{inlet} = 1\ [m^2/s^2] \tag{3.19}$$

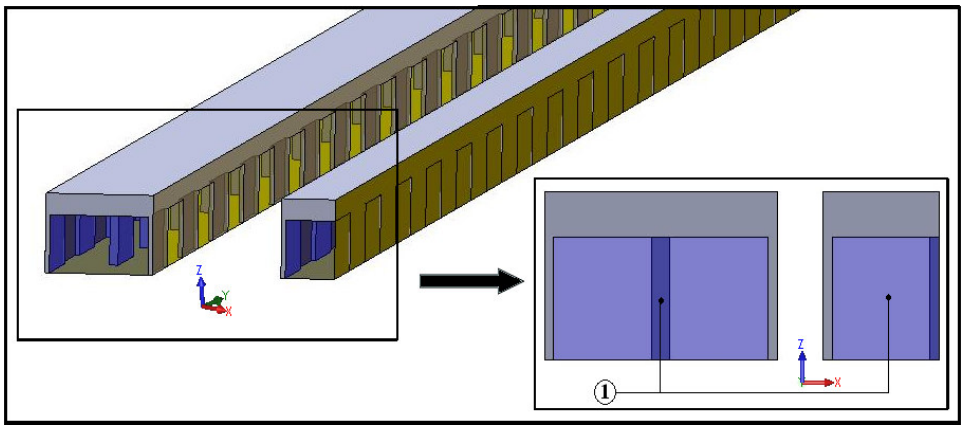

Figure 3.12. Inlet boundary condition surface.

3.4.2. Outlet Boundary Condition

Static Pressure is defined as an outlet boundary condition for the surface which is shown in Figure 3.13 as (2). Since inlet pressure will be calculated at each iteration, the outlet pressure simplify kept at a constant value. Static pressure value at the outlet surface is kept as zero at all analysis.

$$P_y|_{\text{outlet}} = 0 \text{ (Pa)} \tag{3.20}$$

for turbulent flow

$$\frac{\partial k}{\partial y} = 0 \text{ and } \frac{\partial \varepsilon}{\partial y} = 0 \tag{3.21}$$

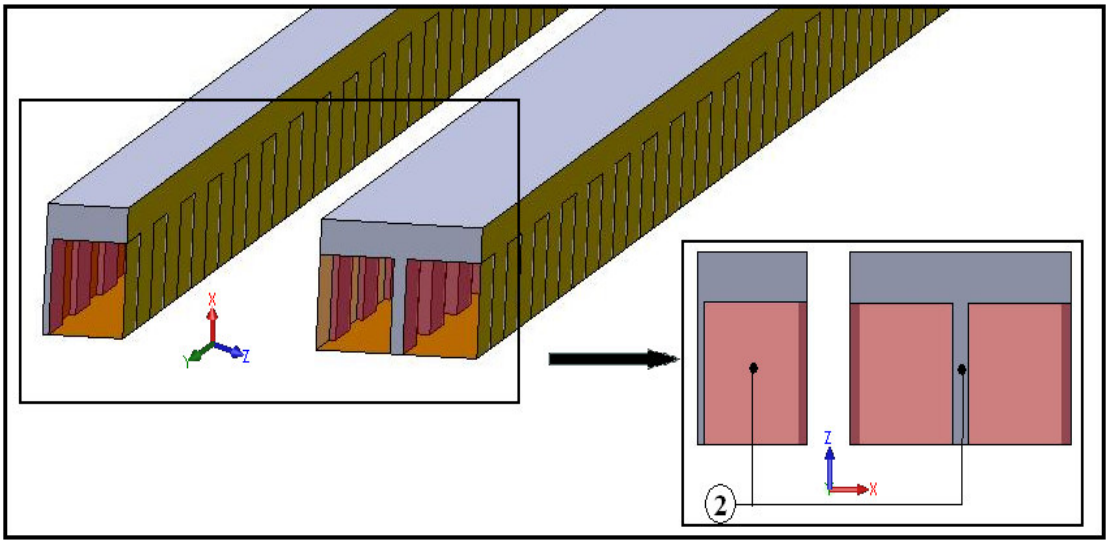

Figure 3.13. Outlet boundary condition surface.

3.4.3. Symmetry Boundary Condition

Symmetry boundary conditions are used when the physical geometry of interest, and the expected pattern of the solution, has symmetry. This condition means that there must be zero flux of all quantities across that boundary. There is no convective flux across a symmetry plane, so the normal velocity component at symmetry plane is zero.

There is also no diffusion flux across symmetry plane, therefore the normal gradients of all flow variables are zero at symmetry plane (Versteeg and Malalasekera 1995).

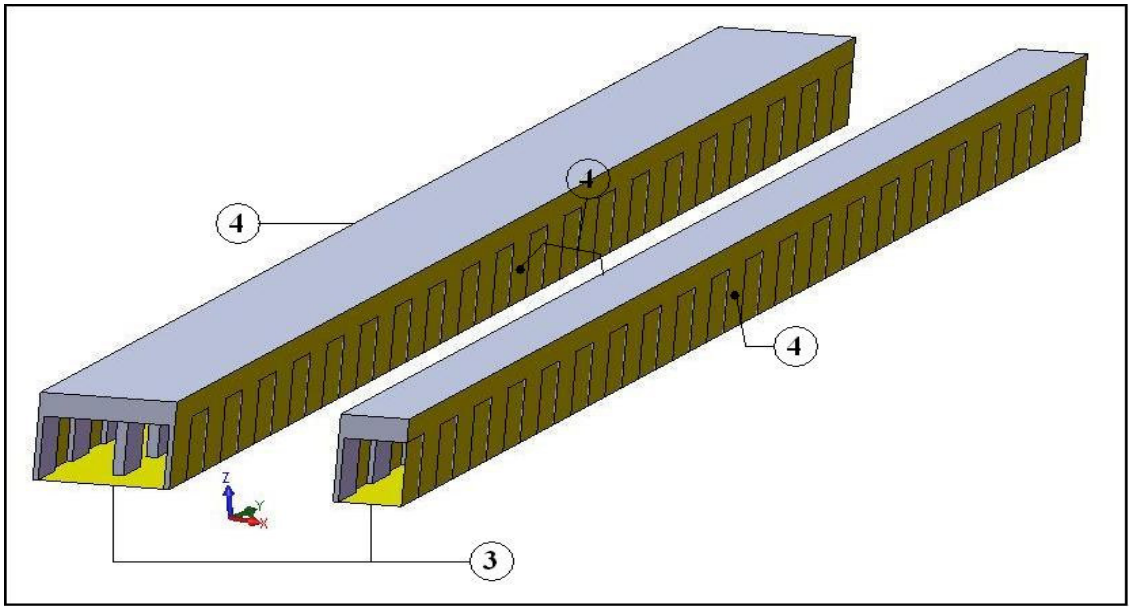

Figure 3.14. Symmetry boundary condition surfaces.

Symmetry boundary conditions are defined for the left and right surfaces indicated as (4), and bottom surface indicated as (3) in Figure 3.14 of the computational.

For the surface (3), whose normal is at z direction, the symmetry conditions are computationally defined as;

$$\frac{\partial T}{\partial z} = 0 \tag{3.22}$$

$$w = 0 \tag{3.23}$$

$$\frac{\partial u}{\partial z} = 0 \tag{3.24}$$

$$\frac{\partial v}{\partial z} = 0 \tag{3.25}$$

for turbulent flow

$$\frac{\partial k}{\partial z} = 0 \text{ and } \frac{\partial \varepsilon}{\partial z} = 0 \tag{3.26}$$

For the surfaces (4), whose normal is at x direction, the symmetry conditions are computationally defined as;

$$\frac{\partial T}{\partial x} = 0 \tag{3.27}$$

$$u = 0 \tag{3.28}$$

$$\frac{\partial v}{\partial x} = 0 \tag{3.29}$$

$$\frac{\partial w}{\partial x} = 0 \tag{3.30}$$

for turbulent flow

$$\frac{\partial k}{\partial x} = 0 \text{ and } \frac{\partial \varepsilon}{\partial x} = 0 \tag{3.31}$$

3.4.4. Wall Boundary Condition

Wall boundary conditions are use to bound solid and fluid regions. The wall boundaries can be stationary or moving walls that depend on the problem. In this thesis all walls are defined as stationary. For that reason, all of the velocity component values at these walls are zero. Several thermal boundary conditions can be defined at wall boundaries such as constant temperature, heat flux, convective heat transfer coefficient etc. Details about the boundary conditions using in this thesis and their definitions are as follows;

3.4.4.1. Thermal Boundary Conditions

Two different types of thermal boundary conditions at the wall indicated as (5) in red surfaces in Figure 3.15 are defined. These are constant heat flux and uniform temperature.

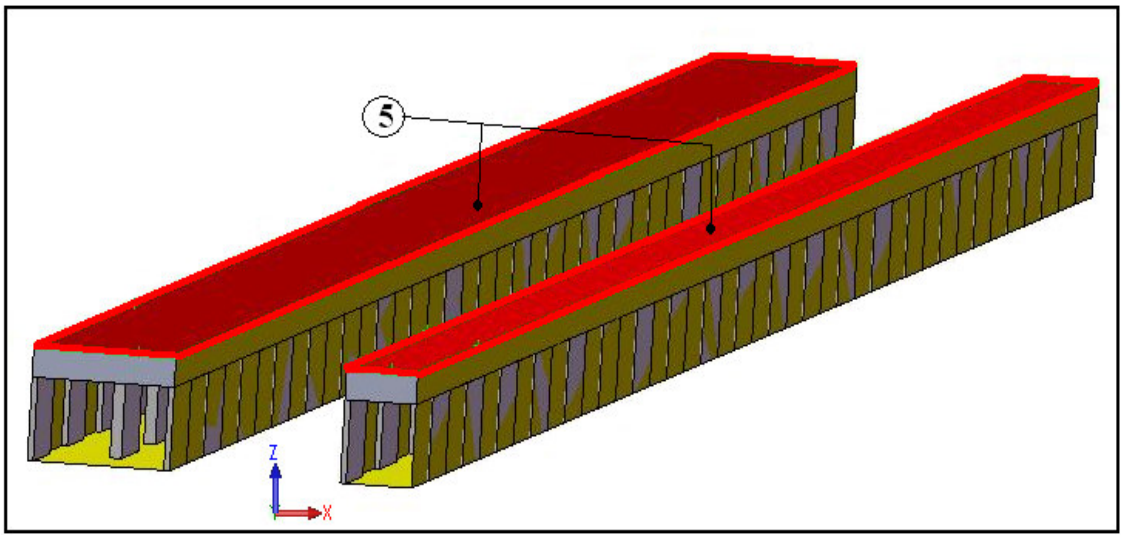

Figure 3.15. Thermal boundary conditions at walls

When a constant temperature condition is applied at the wall, the heat flux from the wall boundary to a solid cell is computed as

$$q = -\frac{k_{Al}}{\Delta n}(T_{wall} - T_{solid}) \tag{3.32}$$

where, Δn is the normal distance between wall surface and the solid center. And the uniform temperature thermal boundary condition for the surface is defined as

$$T|_{x,y} = 373\ [K] \tag{3.33}$$

As for a constant heat flux boundary condition, the wall surface temperature is computed as

$$T_{wall} = T_{solid} - \frac{q \Delta n}{k_{Al}} \tag{3.34}$$

And the constant heat flux boundary condition for the surfaces is;

$$q_x = q_y = 24 \text{ [W/cm}^2\text{]}, \; q_z = 0 \tag{3.35}$$

3.4.4.2. Adiabatic Walls

In this thesis, the walls at the inlet and the outlet sides are assumed to be adiabatic as shown in Figure 3.16. Adiabatic walls are perfectly insulated from heat flow.

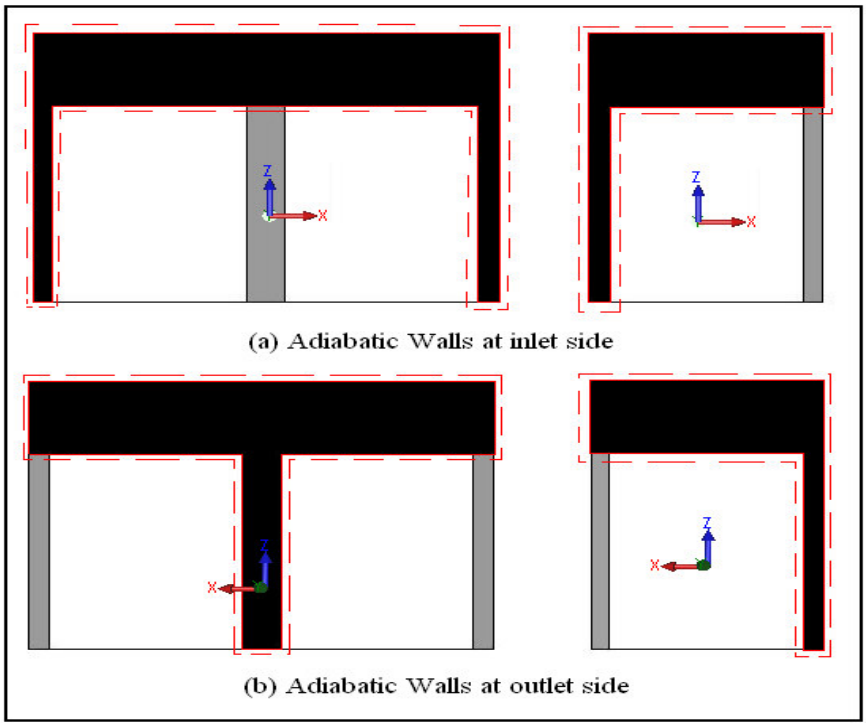

Figure 3.16. Adiabatic wall condition

The adiabatic wall condition for these surfaces is defined as

$$-k_{Al}\left.\frac{\partial T}{\partial n}\right|_{solid}=0 \tag{3.36}$$

where, n is the surface normal direction.

3.4.4.3. Interface Walls

The surfaces of solid regions which are in contact with the fluid region are called interface walls. These surfaces in black are shown in Figure 3.17.

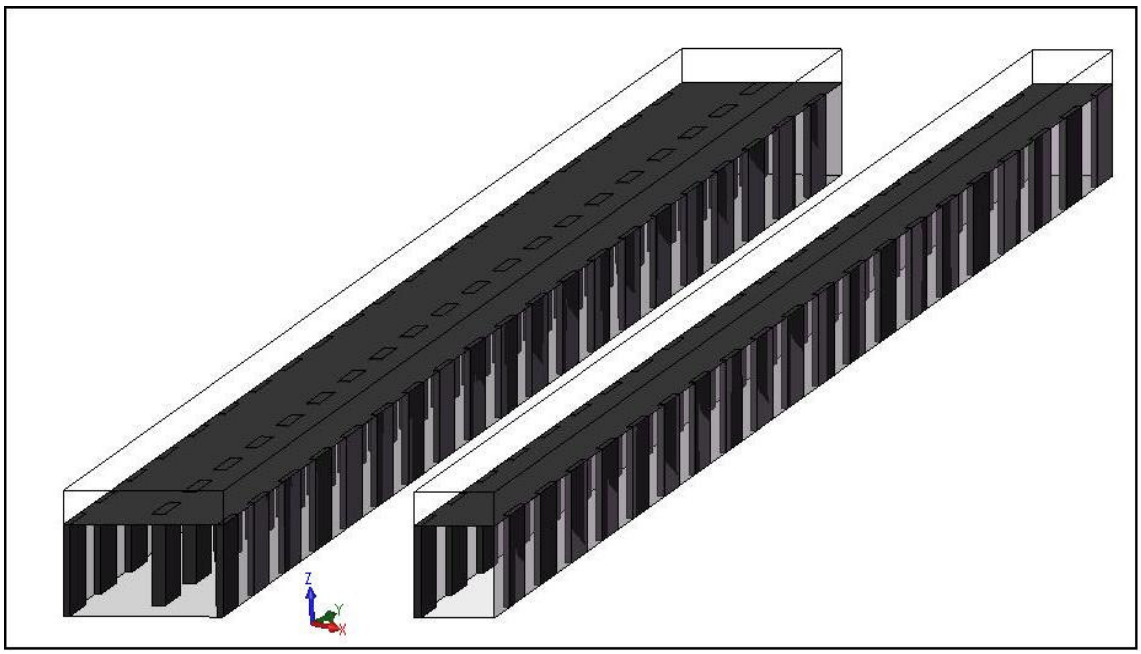

Figure 3.17. Interface walls.

The following conditions can be written for these interface walls;

$$u = v = w = 0 \tag{3.37}$$

$$-k_{Al}\left.\frac{\partial T}{\partial n}\right|_{solid} = -k_{fluid}\left.\frac{\partial T}{\partial n}\right|_{fluid} \tag{3.38}$$

$$h_{fluid}\,(T_{wall} - T_{fluid}) = -k_{Al}\left.\frac{\partial T}{\partial n}\right|_{solid} \tag{3.39}$$

The heat transfer coefficient h_{fluid} is computed based on local flow-field conditions such as temperature and velocity profiles, turbulence level etc. The pressure values at these interface surfaces are calculated since the wall velocities are known.

3.5. Governing Equations

In this part, the governing equations are given for considered problem under three distinct flow conditions. These are steady-laminar, unsteady-laminar and turbulent flow. Hence, this part may be divided into two minor parts as laminar and turbulence.

3.5.1. Laminar flow

In order to determine the flow characteristics such as velocity, temperature and pressure field of the flow, the following governing equations must be solved;

- Continuity Equation

The mathematical expression of the principle of conservation of mass applied to an elemental control volume within a fluid in motion is called the continuity equation and is given by Eq. 3.40.

$$\frac{\partial \rho}{\partial \mathrm{t}} + \frac{\partial}{\partial x_i}(\rho u_i) = 0 \tag{3.40}$$

The first term on the left hand side of continuity equation is the time rate of change of density (mass per volume). The second term is the convective term. The above equation is valid for unsteady flows of compressible fluids. The problem we consider here is incompressible and therefore, the continuity equation reduces to

$$\frac{\partial u_i}{\partial x_i} = 0 \tag{3.41}$$

$\boldsymbol{u_i}$ is the tensor notation of velocity vector of the fluid and it has three components for Cartesian coordinate, one in x direction (u_1=$\boldsymbol{u}$), one in y direction (u_2=$\boldsymbol{v}$) and one in z direction (u_3=$\boldsymbol{w}$). So $\boldsymbol{u_i}$ can also be written as;

$$u_i = u\vec{i} + v\vec{j} + w\vec{k} \tag{3.42}$$

The equation can be written in rectangular coordinates as

$$\frac{\partial u}{\partial x} + \frac{\partial v}{\partial y} + \frac{\partial w}{\partial z} = 0 \tag{3.43}$$

The continuity equation is valid for steady as well as unsteady flows.

- Momentum Equations

The dynamic behavior of fluid in motion is governed by a set of equations called the momentum equations or the equations of motion. These equations are obtained by applying Newton's second law of motion to a very small mass of fluid.

$$\frac{\partial}{\partial t}(\rho u_i) + \frac{\partial}{\partial x_j}(\rho u_i u_j) = -\frac{\partial P}{\partial x_i} + \frac{\partial}{\partial x_j}\left[\mu\left(\frac{\partial u_i}{\partial x_j} + \frac{\partial u_j}{\partial x_i} - \frac{2}{3}\delta_{ij}\frac{\partial u_i}{\partial x_j}\right)\right] + \rho F_i \tag{3.44}$$

where, $\delta_{ij} = \begin{cases} 1 \text{ for } i = j \\ 0 \text{ for } i \neq j \end{cases}$

The above equation is a general form of Navier-Stokes equations. The equation is valid any viscous, compressible Newtonian fluid with varying viscosity. The F term represents body forces such as forces of gravitational, electrical and surface forces. The body force can be written as

$$F_i = f_x\vec{i} + f_y\vec{j} + f_z\vec{k} \tag{3.45}$$

- Energy Equation

The energy equation may be obtained by applying the first law of thermodynamics to a differential element of mass. The first law of thermodynamics states that the rate of heat transfer to an element minus the rate of work done by the element is equal to the rate of increase of energy of that element. The energy equation may be written in terms of fluid enthalpy ***I*** is defined by:

$$I = U + \frac{P}{\rho} \tag{3.46}$$

$$\rho\frac{DI}{Dt} = \nabla(k\nabla T) + \frac{DP}{Dt} + \Phi + \dot{q} \tag{3.47}$$

In the energy equation (3.50) the term on the left-hand side term represents the convective terms, and the terms on the right-hand side from left to right are the rate of heat diffusion, the rate of reversible work done on the fluid particles by compression, the rate of viscous dissipation per unit volume, and heat generation per unit volume. Since for an incompressible fluid with constant physical properties,

$$dU = cdT \tag{3.48}$$

where ***c*** is the specific heat of fluid.

The above set of equations is valid for both laminar and turbulent flows. In order to analyze the problem under steady-laminar condition, the time dependent terms in the governing equations should be ignored.

The above set of equations also is coupled and nonlinear. They are only valid for the fluid side of the considered problems and it should be noted that the density, dynamic viscosity, specific heat and thermal conductivity values are taken for the working fluid which one wants to be analyzed. There are five unknowns as $\boldsymbol{u}$, $\boldsymbol{v}$, $\boldsymbol{w}$, P, T and solution of the above set of equations provides the distributions of these unknowns in the computational domain. For the solid zones the Equation 3.47 should be used ignoring the velocity terms, thus obtaining a conduction equation, and constant thermo-physical properties of aluminum ought to be taken. These equations are suitable for the computational domains, given in Figure 3.11, investigated under steady and unsteady-laminar cases in this thesis. The details of the computational domain are explained in section 3.6 of this chapter.

In next part, detailed information about the turbulence model and also its calculation method is given.

3.5.2. Turbulent flow

The standard k-epsilon (k-ε) model is used to model the turbulent flow. It must be noted, however, that the quantities such as velocity, pressure, and temperature in these governing equations described above are instantaneous values. In turbulent flow, the values always vary with time, and the variations are modeled as irregular fluctuations about mean values as shown in Figure 3.18 (Kakaç S. and Yener Y. 1994).

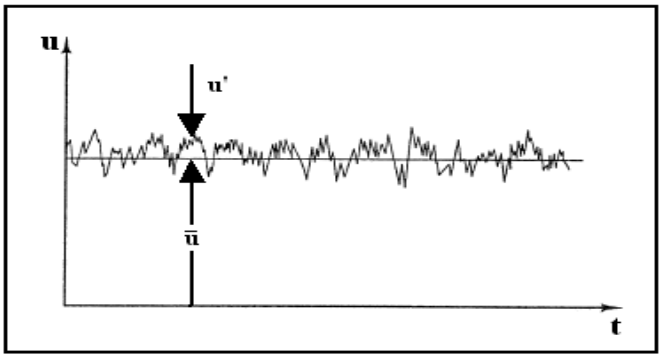

Figure 3.18. Variation of the velocity component u with time

The velocity can be decomposed into a steady mean value $\bar{u}$ plus a time-dependent fluctuating component u'(t) as seen in Figure 3.18:

$$u(x,y,z,t) = \bar{u}(x,y,z) + u'(x,y,z,t) \tag{3.49}$$

The same decomposition rule applies to the other variables of the flow field as well:

$$v = \bar{v} + v' \qquad w = \bar{w} + w' \tag{3.50}$$
$$P = \bar{P} + P' \qquad T = \bar{T} + T'$$

The fluctuating component such as $u'(t)$ can be seen from Figure 3.18 to have both positive and negative values, and the mean value $\bar{u}$ is defined as

$$\bar{u} \equiv \frac{1}{\Delta t}\int_{t_o}^{t_o+\Delta t} u\,dt \tag{3.51}$$

where Δt is sufficiently large compared to the period of the random fluctuations associated with turbulence in order to obtain a true average of the flow components. Hence it becomes clear that

$$\bar{u}' \equiv \int_{t_o}^{t_o+\Delta t} u'\,dt \equiv 0 \tag{3.52}$$

because during the period Δt all the fluctuating components of velocity cancel each other. This statement is same and true for other variables of flow field, temperature, pressure etc.

Turbulent flow is defined as steady when the mean values of variables of flow field such as $\bar{u}, \bar{v}, \bar{w}, \bar{P}, \bar{T}$ etc. do not change with time. Therefore, the time average of all quantities describing the fluctuations is equal to zero (Kakaç S. and Yener Y. 1994).

In order to obtain the governing equations for the turbulent flow, a special set of algebraic rules that follow from equation (3.51) and also equation (3.52) is defined (Bejan A, 1993):

$$\overline{u'} = 0 \quad ; \quad \overline{\left(\frac{\partial u}{\partial x}\right)} = \frac{\partial \overline{u}}{\partial x} \quad ; \quad \overline{\left(\frac{\partial u}{\partial t}\right)} = 0 \quad ; \quad \frac{\partial \overline{u}}{\partial t} = 0$$

$$\overline{\overline{u}u'} = 0 \quad ; \quad \overline{uv} = \overline{u}\,\overline{v} + \overline{u'v'} \quad ; \quad \overline{u+v} = \overline{u} + \overline{v} \quad ; \quad \overline{u^2} = (\overline{u})^2 + \overline{(u')^2} \tag{3.53}$$

- Continuity Equation

In order to obtain the continuity equation for turbulent flow, the equations (3.49) and (3.50) should be substituted into the instantaneous continuity equation obtained from equation (3.48) for an incompressible flow with constant fluid properties. Thus, it is written as (Kakaç and Yener 1994);

$$\frac{\partial \overline{u}}{\partial x} + \frac{\partial \overline{v}}{\partial y} + \frac{\partial \overline{w}}{\partial z} + \frac{\partial u'}{\partial x} + \frac{\partial v'}{\partial y} + \frac{\partial w'}{\partial z} = 0 \tag{3.54}$$

When this equation is averaged over a time interval Δt by using the definitions of equations (3.51) and (3.52), the time averages of the fluctuating components become zero and the average quantities $\overline{u}$, $\overline{v}$ and $\overline{w}$ remain the same (Kakaç and Yener 1994). Thus the equation (3.54) reduces to

$$\frac{\partial \overline{u}}{\partial x} + \frac{\partial \overline{v}}{\partial y} + \frac{\partial \overline{w}}{\partial z} = 0 \tag{3.55}$$

- Momentum Equations

A similar process with continuity equation is performed on momentum equations (3.46 – 3.48). And assuming that the flow is steady and has constant flow properties, then the momentum equations become

$$\left(\overline{u}\frac{\partial \overline{u}}{\partial x} + \overline{v}\frac{\partial \overline{u}}{\partial y} + \overline{w}\frac{\partial \overline{u}}{\partial z}\right) + \left(\frac{\partial}{\partial x}(\overline{u'^2}) + \frac{\partial}{\partial y}(\overline{u'v'}) + \frac{\partial}{\partial z}(\overline{u'w'})\right) = -\frac{1}{\rho}\frac{\partial P}{\partial x} + \nu\nabla^2\overline{u} \tag{3.56}$$

$$\left(\overline{u}\frac{\partial \overline{v}}{\partial x} + \overline{v}\frac{\partial \overline{v}}{\partial y} + \overline{w}\frac{\partial \overline{v}}{\partial z}\right) + \left(\frac{\partial}{\partial x}(\overline{u'v'}) + \frac{\partial}{\partial y}(\overline{v'^2}) + \frac{\partial}{\partial z}(\overline{v'w'})\right) = -\frac{1}{\rho}\frac{\partial P}{\partial y} + \nu\nabla^2\overline{v} \tag{3.57}$$

$$\left(\overline{u}\frac{\partial\overline{w}}{\partial x}+\overline{v}\frac{\partial\overline{w}}{\partial y}+\overline{w}\frac{\partial\overline{w}}{\partial z}\right)+\left(\frac{\partial}{\partial x}(\overline{u'w'})+\frac{\partial}{\partial y}(\overline{v'w'})+\frac{\partial}{\partial z}(\overline{w'^2})\right)=-\frac{1}{\rho}\frac{\partial P}{\partial z}+\nu\nabla^2\overline{w} \qquad (3.58)$$

It is important to note that the first term in the parenthesis on the left hand side and the right hand side terms appear in the instantaneous equations, but extra term which is the second term on the left hand side of the momentum equations given above has been obtained after the substitutions are done for turbulent flow. The new term involves products of fluctuating velocities and constitute convective momentum transfer due to the velocity fluctuations. Generally, it is customary to place this term on the right hand side of the equations (3.59 – 3.61) to reflect its role as additional turbulent stresses on the mean velocity components $\overline{u}$, $\overline{v}$ and $\overline{w}$ (Versteeg and Malalasekera 1995), (Bejan 1993):

$$\left(\overline{u}\frac{\partial\overline{u}}{\partial x}+\overline{v}\frac{\partial\overline{u}}{\partial y}+\overline{w}\frac{\partial\overline{u}}{\partial z}\right)=-\frac{1}{\rho}\frac{\partial P}{\partial x}+\nu\nabla^2\overline{u}+\left(-\frac{\partial}{\partial x}(\overline{u'^2})-\frac{\partial}{\partial y}(\overline{u'v'})-\frac{\partial}{\partial z}(\overline{u'w'})\right) \qquad (3.59)$$

$$\left(\overline{u}\frac{\partial\overline{v}}{\partial x}+\overline{v}\frac{\partial\overline{v}}{\partial y}+\overline{w}\frac{\partial\overline{v}}{\partial z}\right)=-\frac{1}{\rho}\frac{\partial P}{\partial y}+\nu\nabla^2\overline{v}+\left(-\frac{\partial}{\partial x}(\overline{u'v'})-\frac{\partial}{\partial y}(\overline{v'^2})-\frac{\partial}{\partial z}(\overline{v'w'})\right) \qquad (3.60)$$

$$\left(\overline{u}\frac{\partial\overline{w}}{\partial x}+\overline{v}\frac{\partial\overline{w}}{\partial y}+\overline{w}\frac{\partial\overline{w}}{\partial z}\right)=-\frac{1}{\rho}\frac{\partial P}{\partial z}+\nu\nabla^2\overline{w}+\left(-\frac{\partial}{\partial x}(\overline{u'w'})-\frac{\partial}{\partial y}(\overline{v'w'})-\frac{\partial}{\partial z}(\overline{w'^2})\right) \qquad (3.61)$$

These extra turbulent stresses are termed as Reynolds stresses. This set of equations (3.59 – 3.61) is called the Reynolds Averaged Navier Stokes -RANS- equations.

- Energy Equation

A similar process is performed on energy equation (3.47) and assuming that the flow is steady and incompressible with constant thermal conductivity, no viscous heat dissipation, no compression work and without heat generation inside, for steady-turbulent flow the energy equation (3.47) takes the form of

$$\overline{u}\frac{\partial \overline{T}}{\partial x}+\overline{v}\frac{\partial \overline{T}}{\partial y}+\overline{w}\frac{\partial \overline{T}}{\partial z}=\alpha\nabla^2\overline{T}+\left(-\frac{\partial}{\partial x}(\overline{u'T'})-\frac{\partial}{\partial y}(\overline{v'T'})-\frac{\partial}{\partial z}(\overline{w'T'})\right) \qquad (3.62)$$

The terms on the left-hand side of equation (3.62) represents the heat transfer by convection. The first term on the right-hand side represents the heat transfer by molecular conduction within the fluid, and second term represents the process of turbulent or eddy transfer (convective transfer). Transfer processes in a turbulent flow are controlled by two mechanisms: molecular and convective diffusions. Therefore, property fluctuations in a turbulent system produce apparent (total) stresses and fluxes (Kakaç and Yener 1994).

- Transport Equations

The standard ***k***- ***ε*** model is used as a turbulence model in this thesis. Assumed that the flow is incompressible with constant thermal conductivity, there is no heat dissipation, no compression work and without heat generation. The turbulence is assumed to be homogeneous and isotropic and therefore, the turbulence kinetic energy ***k***, and its rate of dissipation ***ε***, are given by following two equations (Versteeg and Malalasekera 1995);

$$\rho\left(\overline{u}\frac{\partial k}{\partial \mathrm{x}}+\overline{\mathrm{v}}\frac{\partial \mathrm{k}}{\partial \mathrm{y}}+\overline{\mathrm{w}}\frac{\partial \mathrm{k}}{\partial \mathrm{z}}\right)=\left[\left(\mu+\frac{\mu_{\mathrm{t}}}{\sigma_{\mathrm{k}}}\right)\left(\frac{\partial^2 k}{\partial \mathrm{x}^2}+\frac{\partial^2 k}{\partial \mathrm{y}^2}+\frac{\partial^2 k}{\partial z^2}\right)\right]+G_k-\rho\varepsilon \qquad (3.63)$$

$$\rho\left(\overline{u}\frac{\partial \varepsilon}{\partial \mathrm{x}}+\overline{\mathrm{v}}\frac{\partial \varepsilon}{\partial \mathrm{y}}+\overline{\mathrm{w}}\frac{\partial \varepsilon}{\partial \mathrm{z}}\right)=\left[\left(\mu+\frac{\mu_{\mathrm{t}}}{\sigma_{\varepsilon}}\right)\left(\frac{\partial^2 \varepsilon}{\partial \mathrm{x}^2}+\frac{\partial^2 \varepsilon}{\partial \mathrm{y}^2}+\frac{\partial^2 \varepsilon}{\partial z^2}\right)\right]+C_{1\varepsilon}\frac{\varepsilon}{k}G_k-C_{2\varepsilon}\rho\frac{\varepsilon^2}{k} \qquad (3.64)$$

In these equations, the left-hand side term is transport of kinetic energy. The first tem in parenthesis on right-hand side is the diffusion of ***k*** or ***ε*** , second term is rate of production of ***k*** or ***ε.*** G_k represents the generation of turbulent kinetic energy due to mean velocity gradients, and calculated as;

$$G_k = -\rho\overline{u_i' u_j'}\frac{\partial \overline{u}_j}{\partial x_i} \tag{3.65}$$

to evaluate G_k in a manner consistent with the Boussinesq hypothesis,

$$G_k = \mu_t S^2 \tag{3.66}$$

where S is the modulus of the mean rate-of-strain tensor, defined as

$$S \equiv \sqrt{2S_{ij}S_{ij}} \tag{3.67}$$

and

$$S_{ij} = \frac{1}{2}\left(\frac{\partial \overline{u}_i}{\partial x_j} + \frac{\partial \overline{u}_j}{\partial x_i}\right) \tag{3.68}$$

The turbulent (or eddy) viscosity μ_t is computed by combining $\boldsymbol{k}$ and $\boldsymbol{\varepsilon}$ as follows*:*

$$\mu_t = \rho C_\mu \frac{k^2}{\varepsilon} \tag{3.69}$$

The model constants for the two transport equations $C_{1\varepsilon}, C_{2\varepsilon}, C_\mu$, σ_k and σ_ε have the following values:

$$C_{1\varepsilon} = 1.44, \quad C_{2\varepsilon} = 1.92, \quad C_\mu = 0.09, \quad \sigma_k = 1.0, \quad \sigma_\varepsilon = 1.3$$

- Near Wall Treatments for Wall-Bounded Turbulent Flows

Turbulent flows are significantly affected by the presence of walls. Obviously, the mean velocity field is affected through the no-slip condition that has to be satisfied at the wall. Very close to the walls, viscous damping reduces the tangential velocity fluctuations, while kinematic blocking reduces normal fluctuations. However, towards the outer part of the near-wall region, the turbulence is rapidly augmented by the

production of turbulence kinetic energy, due to the large gradients in the mean velocity.

Traditionally, there are two approaches to modeling the near-wall region shown in Figure 3.19. In one approach the viscosity-affected inner region (viscous sub-layer and buffer layer) is not resolved. Instead, semi-empirical formulas called "wall-functions" are used to bridge the viscosity-affected region between the wall and fully-turbulent region. The use of wall functions obviates the need to modify the turbulence model to account for the presence of the wall.

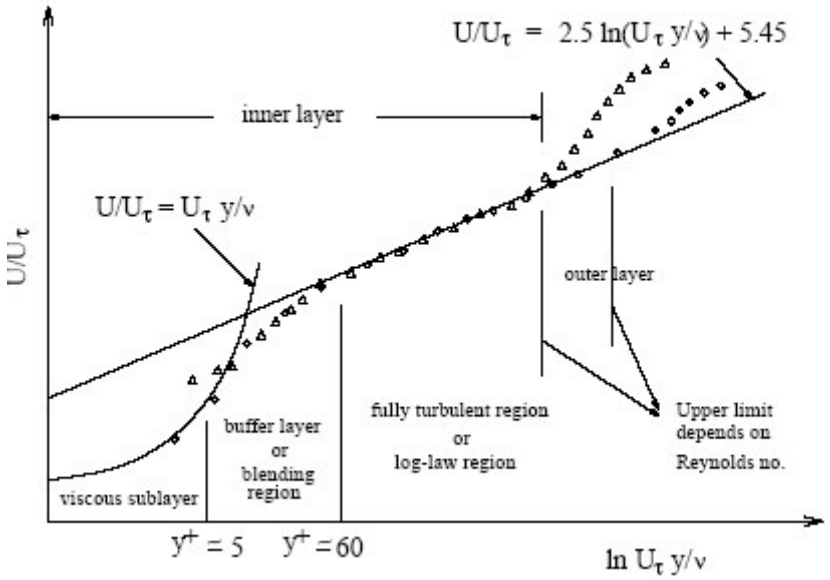

Figure 3.19. Subdivisions of the near-wall region
(Source: Fluent 6.3 User's Guide 2006).

In another approach the turbulence models are modified to enable the viscosity-affected region to be resolved with a mesh all the way to the wall, including the viscous sub-layer and are called the "near-wall modeling" approach.

Among the two approaches, the wall function approach substantially saves computational resources, because the viscosity-affected near-wall region, in which the solution variables change most rapidly, does not need to be resolved. The wall function approach is also economical, and reasonably accurate. For that reasons, the wall function approach is used in thesis.

Wall functions are a collection of semi-empirical formulas and functions that in effect "bridge" or "link" the solution variables at the near-wall cells and the

corresponding quantities on the wall. The wall functions consist of (Fluent 6.3 User's Guide 2006)

- laws-of-the-wall for mean velocity and temperature (or other scalars)
- formulas for near-wall turbulent quantities

The law-of-the-wall for mean velocity yields

$$U^* = \frac{1}{\kappa}\ln(Ey^*) \tag{3.70}$$

where

$$U^* \equiv \frac{U_p C_\mu^{1/4} k_p^{1/2}}{\tau_w / \rho} \tag{3.71}$$

$$y^* \equiv \frac{\rho C_\mu^{1/4} k_p^{1/2} y_p}{\mu} \tag{3.72}$$

and

$\boldsymbol{\kappa}$ = Von Karman constant (= 0.4187)

$\boldsymbol{E}$ = empirical constant (= 9.793)

$\boldsymbol{U_P}$ = mean velocity of the fluid at point P (center of cell)

$\boldsymbol{k_p}$ = turbulence kinetic energy at point P

$\boldsymbol{y_P}$ = distance from point P to the wall

$\boldsymbol{y^*}$ = non-dimensional sublayer thickness

The logarithmic law for mean velocity is known to be valid for $30 < \boldsymbol{y^*} < 300$. The log-law is employed when $\boldsymbol{y^*} > 11.225$. When the mesh is such that $\boldsymbol{y^*} < 11.225$ at the wall-adjacent cells, the laminar stress-strain relationship is applied and the relation can be written as

$$U^* = y^* \tag{3.73}$$

It should be noted that, in the numerical calculations for turbulence flow, the laws-of-the-wall for mean velocity and temperature are based on the wall unit, $\boldsymbol{y^*}$, rather than $\boldsymbol{y^+}$ shown in Figure 3.5.2.

$$y^+ = \frac{\rho U_\tau y}{\mu} \tag{3.74}$$

where the friction velocity is defined as

$$U_\tau = \sqrt{\frac{\tau_w}{\rho}} \tag{3.75}$$

These quantities are approximately equal in equilibrium turbulent boundary layers.
The law-of-the-wall for mean temperature yields

$$T^* \equiv \frac{(T_w - T_p)\rho C_p C_\mu^{1/4} k_p^{1/2}}{\dot{q}} = \begin{cases} \Pr y^* & (y^* < y_T{}^*) \\ \Pr_t \left[\frac{1}{\kappa} \ln(E y^*) + \overline{P} \right] & (y^* > y_T{}^*) \end{cases} \tag{3.76}$$

where $\overline{P}$ is the relationship formula between molecular Prandtl number, **Pr** and turbulent Prandtl number, $\mathbf{Pr}_t$ (0,85 at the wall), and computed by using the formula

$$\overline{P} = 9.24 \left[\left(\frac{\Pr}{\Pr_t} \right)^{3/4} - 1 \right] * \left[1 + 0.28 e^{-0.07(\Pr/\Pr_t)} \right] \tag{3.77}$$

The non-dimensional thermal sublayer thickness, y_T^*, in Equation 3.76 is computed as the y^* value at which the linear law and the logarithmic law intersect, given the molecular Prandtl number of the fluid being modeled.

The procedure of applying the law-of-the-wall for temperature is as follows. Once the physical properties of the fluid being modeled are specified, its molecular Prandtl number is computed. Then, given the molecular Prandtl number, the thermal sublayer thickness, y_T^*, is computed from the intersection of the linear and logarithmic profiles, and stored. During the iteration, depending on the y^* value at the near-wall cell, either the linear or the logarithmic profile in Equation 3.76 is applied to compute the wall temperature T_w or heat flux **q** (depending on the type of the thermal boundary conditions) (Fluent 6.3 User's Guide 2006).

3.6. Numerical Solution of the Governing Equations

The flow in an OSF channel is characterized by a complex flow field, which is affected by blockage and recirculation zones enhanced by narrow gaps. In this case the actual physical device is replaced by a discrete number of nodes that represent the entire geometry of the cell where the distributions of unknowns such as pressure, velocity etc. to be found. The approach requires defining the mathematical equations that govern the physical process. The governing equations of fluid flow and heat transfer given by Equations 3.43, 3.44, and 3.47 for laminar flow and Equations 3.55, 3.58 - 3.64 for turbulent flow can not be solved analytically therefore; these equations should be solved numerically for the investigated fluid flow problems. These equations will be solved only at the discrete points of considered problem.

As above mentioned, the flow problems include the solution of governing equations which are nonlinear partial differential equations (PDEs). First of all, the numerical solution of these governing equations starts from dividing the computational domain into small volumes (sub-domain) that are also called as meshes. For that purpose, the meshing operation for the considered heat exchanger models is accomplished by using commercial software, Gambit. Gambit has ability to generate different structured or unstructured meshes for all kinds of flow geometry. The mesh types for two and three dimensional cases shown in Figure 3.20 are available in Gambit.

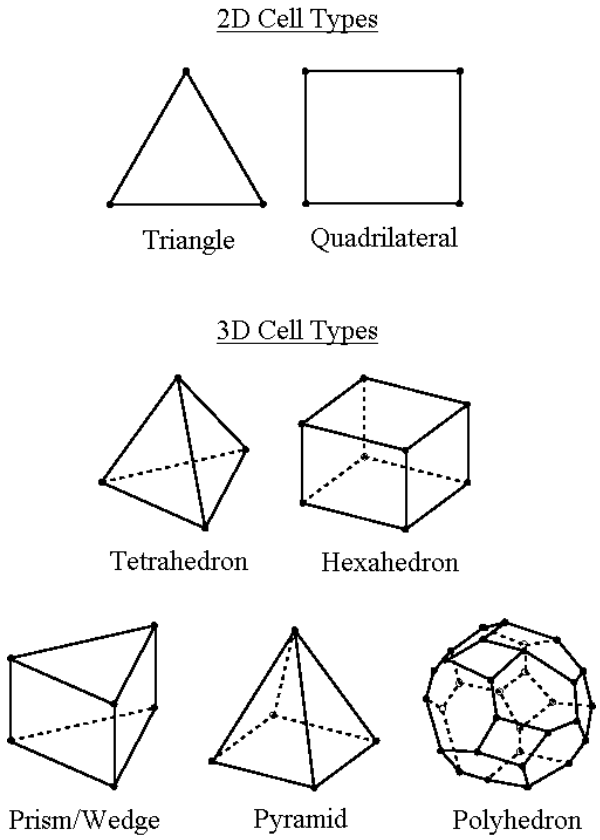

Figure 3.20. Mesh types.
(Source: Fluent 6.3 User's Guide 2006)

The unstructured hexahedral meshes are used to create the computational domain of considered heat exchanger problem. Detailed information about meshing operation for the considered problem is given in section 3.8.

Governing equations are solved by the finite volume method (FVM) which is a special type of the finite difference method. For that purpose, Fluent, one of the commercial CFD software, based on the FVM is used. Fluent includes two numerical methods:

- pressure-based solver
- density-based solver

The pressure-based approach is used for low-speed incompressible flows, while the density-based approach is mainly used for high-speed compressible flows. In both methods the velocity field is obtained from the momentum equations. In the density-based approach, the continuity equation is used to obtain the density field while the pressure field is determined from the equation of state. On the other hand, in the pressure-based approach, the pressure field is extracted by solving a pressure or

pressure correction equation which is obtained by manipulating continuity and momentum equations. Fluent solves the governing integral equations for the conservation of mass and momentum, and (when appropriate) for energy and other scalars such as turbulence. In both cases using a control-volume-based technique is used that consists of (Fluent 6.3 User's Guide 2006):

- Division of the domain into discrete control volumes using a computational grid.
- Integration of the governing equations on the individual control volumes to construct algebraic equations for the discrete dependent variables (unknowns) such as velocities, pressure, temperature, and conserved scalars.
- Linearization of the discretized equations and solution of the resultant linear equation system to yield updated values of the dependent variables.

The two numerical solvers employ a similar discretization process, but the approach used to linearize and solve the discretized equations is different. In this study the pressure-based approach was chosen because of the fact that the flow in OSF channel is incompressible.

In the pressure-based approach, the constraint of mass conservation (continuity) of the velocity field is achieved by solving a pressure (or pressure correction) equation.

The pressure equation is derived from the continuity and the momentum equations in such a way that the velocity field, corrected by the pressure, satisfies the continuity. Two pressure-based solver algorithms are available in Fluent. These are a segregated and a coupled algorithm. In the segregated algorithm, the individual governing equations for the solution variables ($\boldsymbol{u}$, $\boldsymbol{v}$, $\boldsymbol{w}$, P, T, $\boldsymbol{k}$, $\boldsymbol{\varepsilon}$) are solved one after another. Each governing equation is "decoupled" or "segregated" from other equations, while being solved. In this approach the non-linear governing equations are solved sequentially using the iterative technique. Each step in iteration can be summarized as follows (Fluent 6.3 User's Guide 2006, Versteeg and Malalasekera 1995);

1. Update fluid properties (density, viscosity, conductivity, specific heat etc.) including turbulent viscosity (diffusivity) based on the current solution (or initial conditions).
2. Solve the momentum equations, one after another, using the recently updated values of pressure and face mass fluxes.

3. Solve the pressure correction equation using the recently obtained velocity field and the mass-flux.

4. Correct face mass fluxes, pressure, and the velocity field using the pressure correction obtained from Step 3.

5. Solve the equations for additional scalars, if any, such as turbulent quantities, energy, and radiation intensity using the current values of the solution variables.

6. Check for the convergence of the equations.

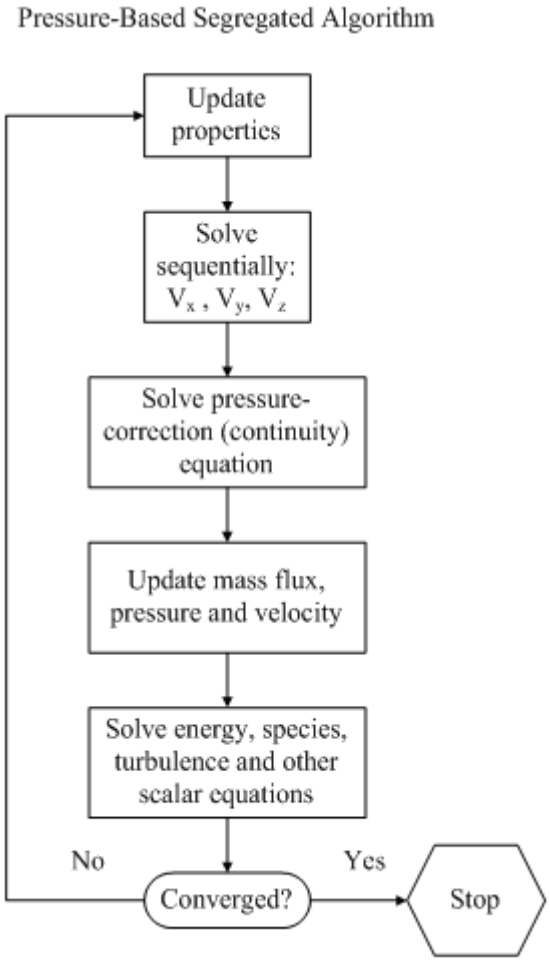

Figure 3.21. Overview of the pressure-based solution methods.
(Source: Fluent 6.3 User's Guide 2006)

Unlike the staggered algorithm described above, the pressure-based coupled algorithm solves a coupled system of momentum and continuity equations. Thus, in the coupled algorithm, Steps 2 and 3 in the segregated solution algorithm are replaced by a single step in which the coupled system of equations are solved. The remaining

equations are solved as in the segregated algorithm. Since the momentum and continuity equations are solved in closely coupled manner, the rate of solution convergence significantly improves when compared to the segregated algorithm. However, the memory requirement increases by 1.5 or 2 times that of the segregated algorithm. Since the discrete system of all momentum and pressure-based continuity equations needs to be stored in memory when solving for the velocity and pressure fields. For that reasons, the pressure-based segregated algorithm is used to solve computational domains of considered problem in thesis.

There is a point which needs to be taken into consideration for the pressure – based algorithms. Solving the momentum equations is too complicated because of the lack of an independent equation for the pressure, whose gradient appears in each of three momentum equations. For that reason some pressure-velocity linkage algorithms can be used in the pressure-based algorithm. There are several of pressure-velocity coupling algorithms in literature known shortly as SIMPLE, SIMPLER, SIMPLEC, and PISO etc. In this thesis, The SIMPLE (Semi Implicit Method for Pressure Linked Equations) algorithm is used to supply the relationship between velocity and pressure fields. The momentum equation is solved using a guessed pressure field which is calculated previous iteration or initial guess to obtain face flux. If the resulting face flux does not satisfy the continuity equation, a correction face flux is added to obtain the corrected face flux because of satisfying the continuity equation. The SIMPLE algorithm substitutes the flux correction equations into the discrete continuity equation to obtain the discrete equation for the pressure correction in the cell.

The governing equations which are discrete and non-linear are linearized to produce a system of equations for dependent variables in every computational cell. The resultant linear system is then solved to yield an updated flow-field solution. In this thesis, the governing equations are linearized by the “Point Implicit Gauss-Siedel” linear equation with respect to the set of dependent variables. By this method the unknown value in each cell is computed using a relation that includes both existing and unknown values from neighboring cells.

In brief, with using the finite control volume technique, the governing equations are converted to algebraic equations that can be solved numerically. This technique consists of integrating the governing equations about each control volume, yielding discrete equations that conserve each quantity on a control volume basis.

Discretisation of the governing equations can be illustrated most easily by considering the unsteady conservation equation for transport of a scalar quantity **Φ**. This is demonstrated by the following equation written in integral form for an arbitrary control volume ***CV*** as follows:

$$\int_{CV} \frac{\partial \rho \Phi}{\partial t} dV + \oint \rho \Phi \vec{u}.d\vec{A} = \oint \Gamma \nabla \Phi.d\vec{A} + \int_{CV} S_{\Phi} dV \tag{3.78}$$

The Equation 3.78 is the so-called transport equation for property **Φ**. The equation is used as the starting point for computational procedures in FVM. By setting **Φ** equal to 1, ***u***, ***v***, ***w*** and T, and selecting the appropriate values for diffusion coefficient **Γ** and source terms $\boldsymbol{S_{\Phi}}$, the governing equations for appreciate problem are obtained.
The integration operation of the governing equations is applied on the individual control volumes in the computational domain to construct algebraic equations for the discrete dependent variables (unknowns) such as velocities, pressure, temperature, and conserved scalars. Discretisation of Equation 3.78 on a given cell yields

$$\frac{\partial \rho \Phi}{\partial t} V + \sum \rho \Phi \vec{u}.d\vec{A} = \sum \Gamma \nabla \Phi.d\vec{A} + S_{\Phi} V \tag{3.79}$$

where $\frac{\partial \rho \Phi}{\partial t} V$ is transient term. For transient simulations, the governing equations must be discretized in both space and time. The spatial discretization for the time-dependent equations is identical to the steady-state case.
The discretized scalar transport equation (Equation 3.79) contains the unknown scalar variable Φ at the cell center as well as the unknown values in surrounding neighbor cells. This equation will, in general, be non-linear with respect to these variables. A linearized form of Equation 3.79 can be written as

$$a_P \Phi = \sum_{nb} a_{nb} \Phi_{nb} + b \tag{3.80}$$

$$a_P = \sum a_{nb} - S_P \tag{3.81}$$

$$S = S_c + S_P \Phi \tag{3.82}$$

where the subscript ***nb*** refers to neighbor cells, and a_P and a_{nb} are the linearized coefficients for Φ and Φ_{nb}, and b is the contribution of the constant part of the source term S_c and of the boundary conditions. Similar equations can be written for each cell in the grid.

The discrete values of scalars at cell centers are stored and the face values of the scalars needed for the convection terms are computed by interpolating the cell center values. The realization of this interpolation is made by using an upwind scheme. Upwinding means that the face values are derived from quantities in the cell upstream, relative to the direction of the normal velocity. There are mainly four different upwinding schemes; first order upwinding scheme, second order upwinding scheme, power law and QUICK scheme. In this thesis the first upwind scheme is used. When this scheme is used, the face value of scalar quantities is set equal to the value in the upstream cell.

At the end of each iteration, the residual sum for each of the conserved variables is computed and stored. On a computer with infinite precision, these residuals will go to zero as the solution converges but on an actual computer, the residuals decay to some small value (round-off) and then stop changing. Residual definitions that are useful for one class of problem are sometimes not appropriate for other classes of problems. Therefore, it is convenient to judge convergence not only by examining residual levels, but also by monitoring relevant quantities.

The residual is defined as the imbalance in Equation 3.80 summed over all the computational cells. In this way unscaled residuals are calculated as (Fluent 6.3 User's Guide 2006);

$$R^{\Phi} = \sum_{cells-P} \left| \sum_{nb} a_{nb}\Phi_{nb} + b - a_P\Phi_P \right| \tag{3.83}$$

Since the unscaled residual is difficult to be used for the judgment of the convergence, the scaled residuals are used instead. The scaled residuals are defined as (Fluent 6.3 User's Guide 2006);

$$R^{\Phi}_{scaled} = \frac{\sum_{cells-P} \left| \sum_{nb} a_{nb}\Phi_{nb} + b - a_P\Phi_P \right|}{\sum_{cells-P} \left| a_P\Phi_P \right|} \tag{3.84}$$

For the momentum equations the denominator term $a_p\Phi_p$ is replaced by a_pV_p, where V_p is the magnitude of the velocity at cell. For the continuity equation, the

unscaled form and scaled form of residual are defined by Equations 3.85 and 3.86, respectively (Fluent 6.3 User's Guide 2006);

$$\text{Unscaled form: } R^c = \sum_{cell\,P} |\text{rate of mass creation in cell P}| \tag{3.85}$$

$$\text{Scaled form: } R^c_{scaled} = \frac{R^c_{iteration\ N}}{R^c_{iteration\ 5}} \tag{3.86}$$

In Equation 3.86, $R^c_{iteration\ N}$ represents the residual at the Nth iteration while $R^c_{iteration\ 5}$ is the largest absolute value of the continuity residual in the first five iterations.

The under-relaxation of equations is used in the pressure-based solver to stabilize the convergence behavior of the nonlinear iterations by introducing selective amounts of Φ in the system of discretized equations (Fluent 6.3 User's Guide 2006).

$$\frac{a_P \Phi}{\alpha} = \sum_{nb} a_{nb} \Phi_{nb} + b + \frac{1-\alpha}{\alpha} a_P \Phi_{old} \tag{3.87}$$

where, α is the under-relaxation factor.

3.7. Grid Generation and Computational Details

3.7.1. Grid Generation

Of explained before, in order to perform numerical calculations, the representative domain of the considered problem should be divided into several small sub domains which are called as meshes or grids. The grid generation for the considered heat exchanger problem including OSF is obtained by using Gambit software.

The considered problem is analyzed for two different flow regimes, laminar and turbulence. In this thesis, only one meshing operation to numerically analyze the problem for both regimes is applied; although, two different meshing operations are in

general required in order to analyze the problem for the two different regimes. Compared to the laminar flow simulations, the turbulent flow is more challenging in many ways, and it needs some extra care for grid generation. In this thesis, for easier data management, grid appropriate for the turbulence case is applied to laminar case as well. For turbulent case, wall function approach is used to resolve the viscosity-affected region between the walls of OSF channels and fully-turbulent region in flow, and the mean quantities in turbulent flow have larger gradients than in laminar flow. For that reason some extra care is taken for grid generation as follows;

- Hexahedral mesh is used.
- First grid point is created in log-law region where $\mathbf{50 \leq y^{+} \leq 500}$ (Fluent 6.3 User's Guide 2006)
- At least ten points are created in boundary layer (Fluent 6.3 User's Guide 2006)

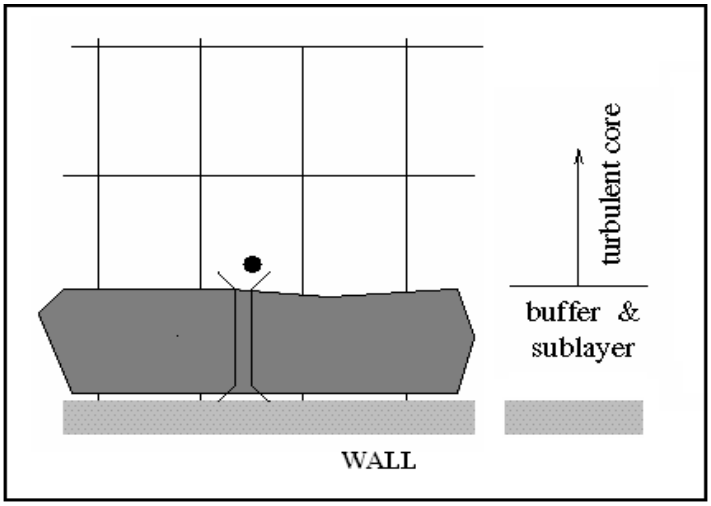

Figure 3.22. Grid generation for wall function approach.
(Source: Fluent 6.3 User's Guide 2006)

As shown in the Figure 3.22 one point should be created in log-law layer for modeling of turbulent flow. For that purpose, the non dimensional sublayer $\mathbf{y^{+}}$ is taken as equal to 50. The first grid point $\mathbf{y_{P1}}$ is calculated as about 0.01 mm by using Equation (3.72 and 3.73) in near wall treatments for wall-bounded turbulent flows section of this chapter and assuming that the problem is analyzed for Reynolds number of 4000 where the flow is turbulent. In order to create at least five points in boundary layer the following equation is used to calculate the boundary layer thickness (Bejan 1993).

$$\frac{\delta}{x} = 0.37\left(\frac{U^* x}{\nu}\right)^{-1/5} \tag{3.88}$$

where ***x*** is taken as the fin length for considered problem. The boundary layer thickness is calculated as about 0.1mm. When the situations are considered the minimum size at one face of the flow part that is conjunction with wall side of solid face is have to equal 0.01. If uniform mesh was considered for the problem, the total mesh number at only this face would have been equal to about 75000. Also the domain has a lot of conjunction faces. Thus the mesh number for whole domain would have achieved to an extreme number. Because of the reasons non-uniform mesh is used to create the grid generation for the numerical domain. As shown in Figure 3.23 the domain is created, which is based on non-uniform mesh and the rules for conjunction faces.

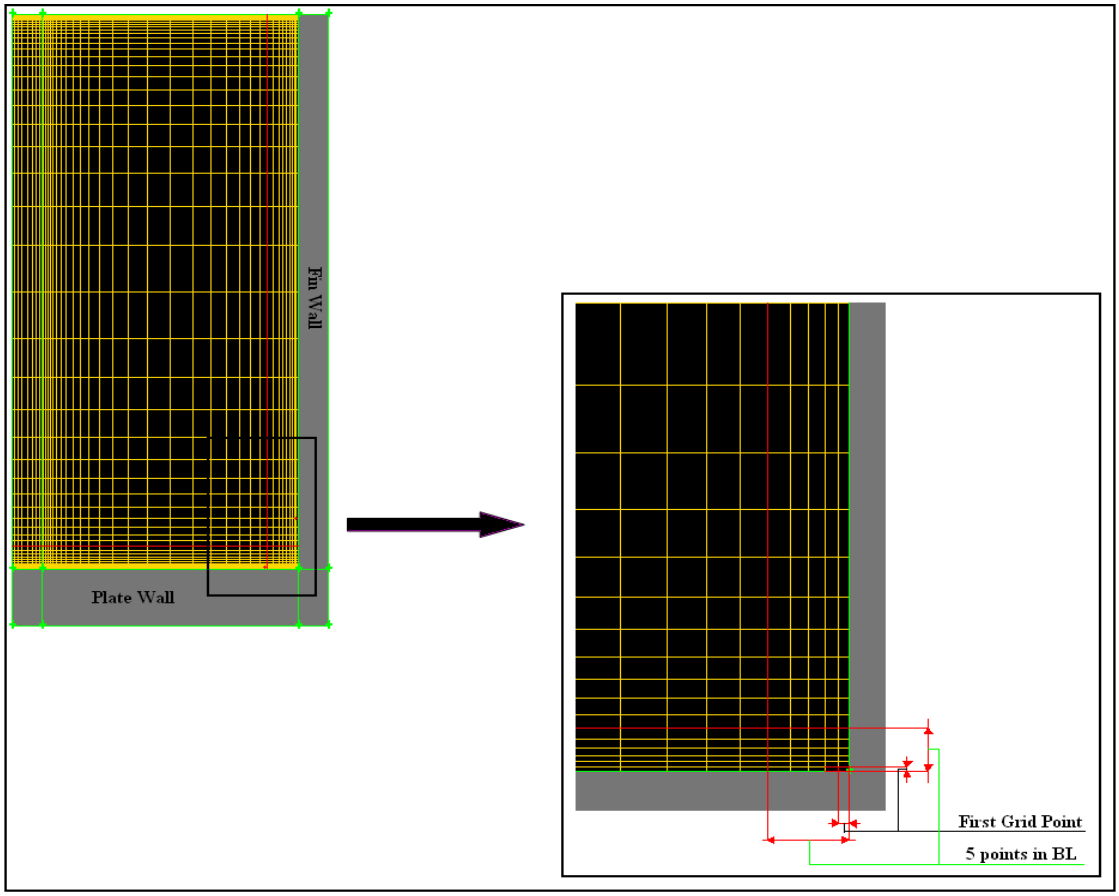

Figure 3.23. Grid generation by applying non-uniform mesh and rules for conjunction faces.

In order to resolve the velocity and temperature fields better the finer scale of meshes are used particularly near the walls, near the leading edges and in the wakes of the domain as shown in Figure 3.24

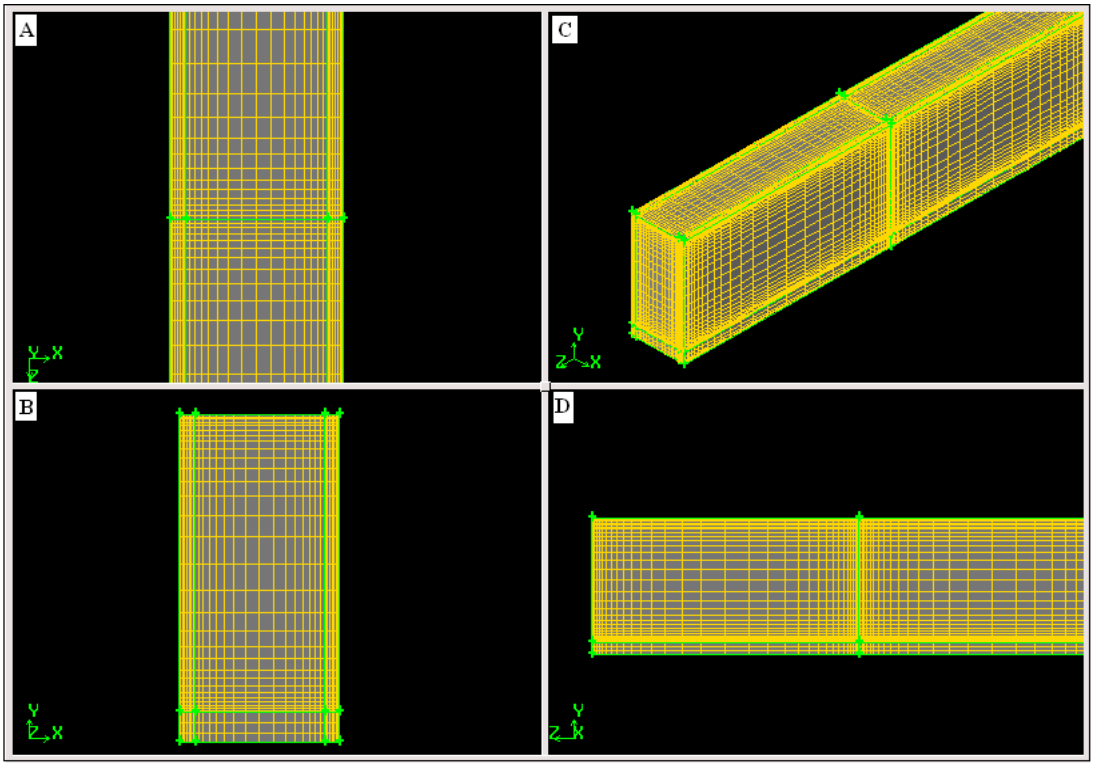

Figure 3.24. Finer meshes in domain (a-Top, b-Front, c-Isometric, and d-Left View)

In order to obtain an optimal mesh the interval sizes of the critical edges shown in Figure 3.25 are orderly changed and the alphabetic codes are given to them. They are tabulated in Table 3.93 according to order of increasing mesh number.

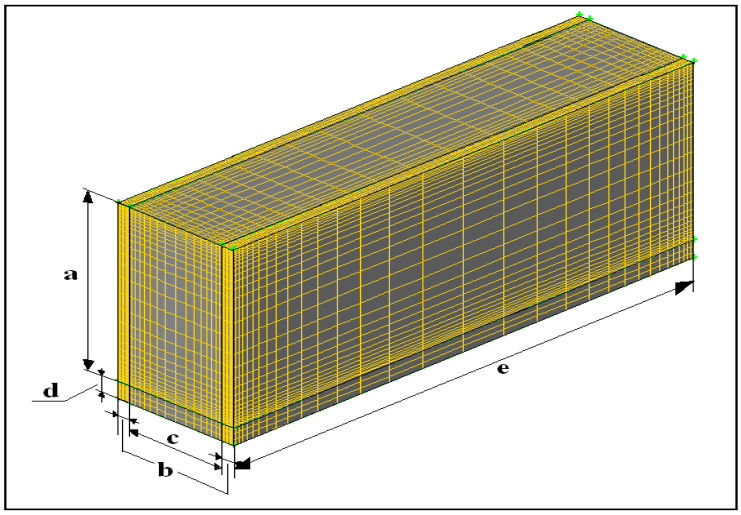

Figure 3.25. Alphabetic codes

Table 3.1. Different mesh numbers

Mesh No	Codes	Interval Size	Non-Uniform Mesh Ratio	Total Mesh in Domain
Mesh-1	**a**	0,1	1,2	**120.960**
	b	0,02	1,2	
	c	0,1	1,2	
	d	0,2	1,2	
	e	0,05	1	
Mesh-2	**a**	0,075	1,2	**375.360**
	b	0,02	1,2	
	c	0,075	1,2	
	d	0,1	1,2	
	e	0,05	1	
Mesh-3	**a**	0,06	1,2	**510.720**
	b	0,02	1,2	
	c	0,06	1,2	
	d	0,1	1,2	
	e	0,05	1	
Mesh-4	**a**	0,05	1,2	**776.000**
	b	0,02	1,2	
	c	0,05	1,2	
	d	0,1	1,2	
	e	0,05	1	
Mesh-5	**a**	0,05	1,2	**1.015.000**
	b	0,01	1,2	
	c	0,04	1,2	
	d	0,1	1,2	
	e	0,05	1	
Mesh-6	**a**	0,05	1,2	**1.289.000**
	b	0,02	1,2	
	c	0,05	1,2	
	d	0,15	1,2	
	e	0,05	1	
Mesh-7	**a**	0,04	1,2	**1.653.000**
	b	0,01	1,2	
	c	0,025	1,2	
	d	0,1	1,2	
	e	0,05	1	

.

Mesh independence analysis is conducted for fanning friction factor f as non-dimensional form of pressure drop and Colbourn j factor as non-dimensional form of heat transfer coefficient at Re=650 (laminar), Re=4000 (turbulence) based on the different mesh numbers shown in Table 3.1. Detailed information about the calculation strategy for the two factors is given in section 3.8. Results are shown in Figure 3.26 and 3.27. It is seen from this figure that at least 1 million meshes are needed to obtain mesh independent results for both of the flow regimes.

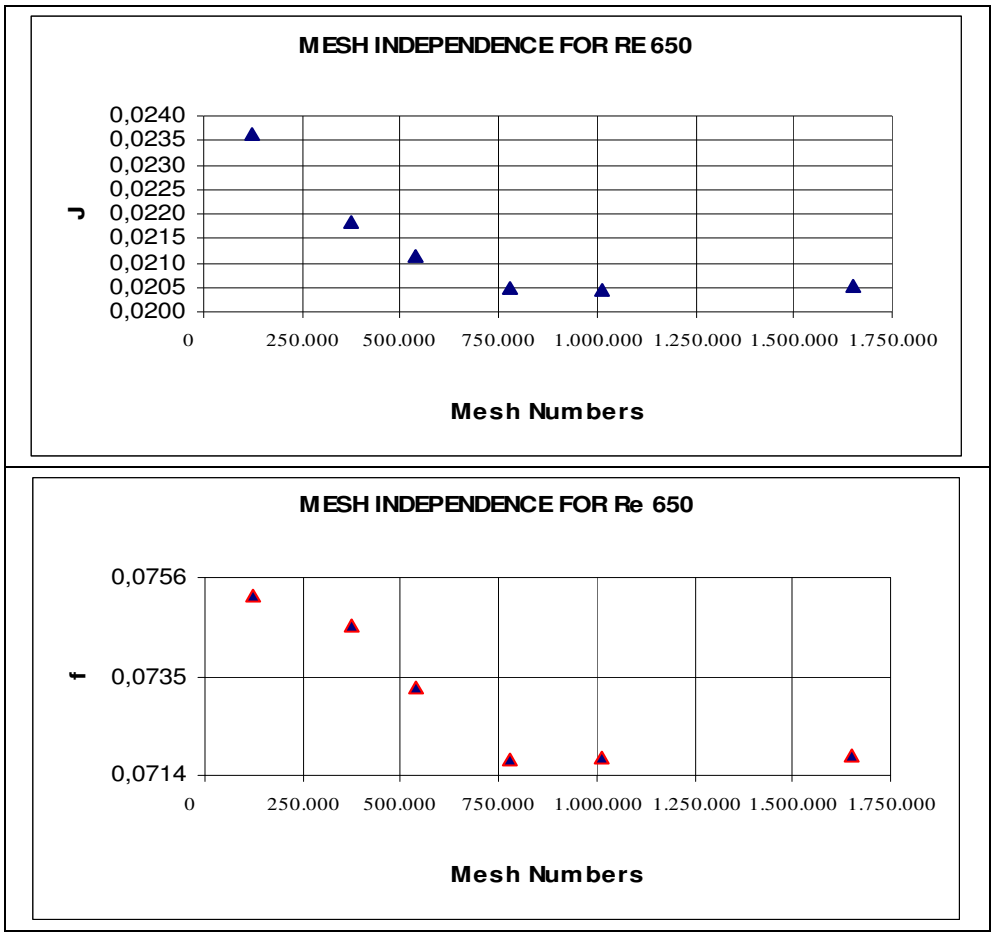

Figure 3.26. Mesh independence analysis for laminar flow

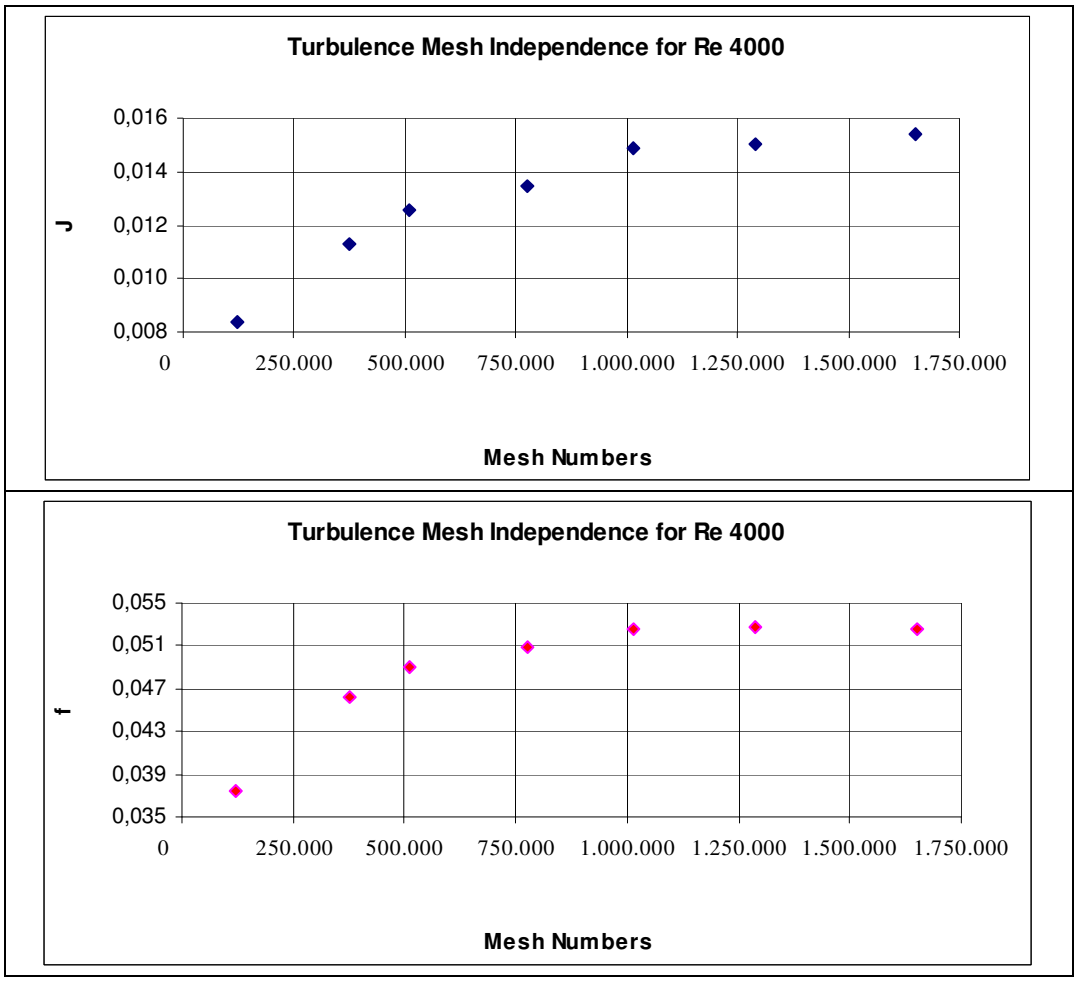

Figure 3.27. Mesh independence analysis for turbulent flow

3.7.2. Computational Details

➢ Convergence

For the investigated problems, scaled residuals for continuity, velocities and energy equations are monitored during the iterative solutions and the following values are taken into consideration for the converged numerical results;

For laminar case

- Residual for continuity: $R^{c}_{scaled}=10^{-4}$
- Residuals for velocities in x, y and z directions: $R^{\Phi}_{scaled,velocity}=10^{-7}$

- Residual for energy: $R^{\Phi}_{scaled,energy} = 10^{-7}$

The residual history of a model is shown in Figure 3.28. Similar residual histories are obtained for all of the investigated numerical models including laminar flow.

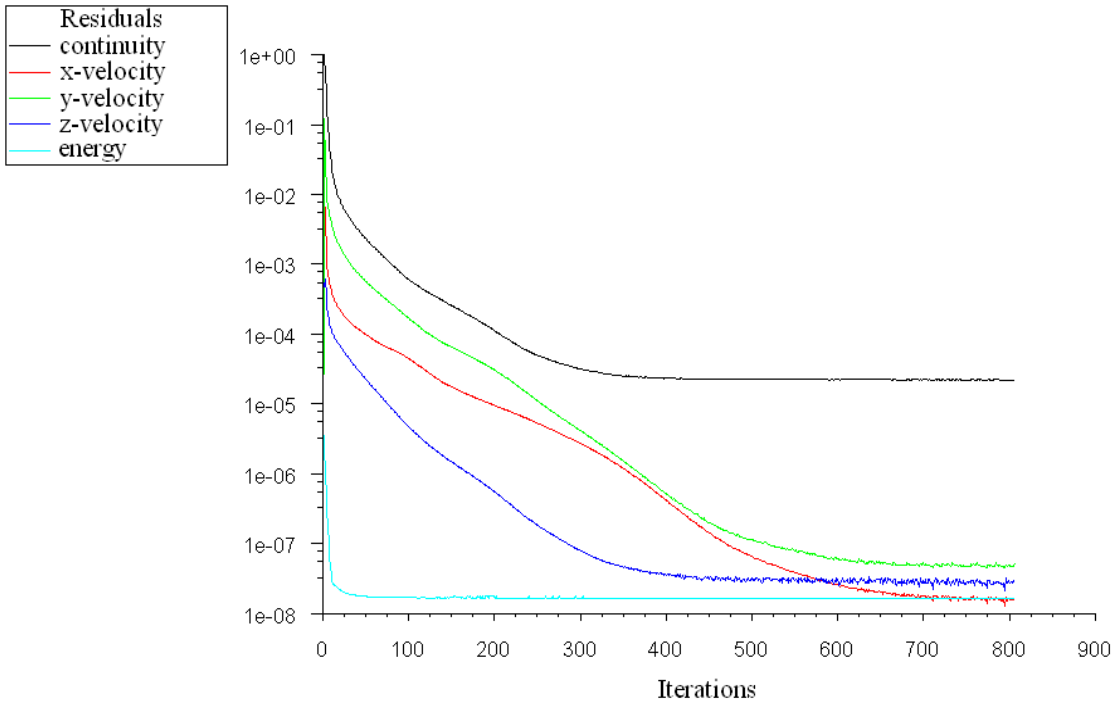

Figure 3.28. Residuals of a numerical model for laminar flow solution.

For turbulent case

- Residual for continuity: $R^{c}_{scaled}=10^{-7}$
- Residuals for velocities in x, y and z directions: $R^{\Phi}_{scaled,velocity} = 10^{-7}$
- Residual for energy: $R^{\Phi}_{scaled,energy} = 10^{-7}$
- Residual for transport equations k - ε: $R^{c}_{scaled}=10^{-7}$

The residual history of a model is shown in Figure 3.29. Similar residual histories are obtained for all of the investigated numerical models including turbulent flow.

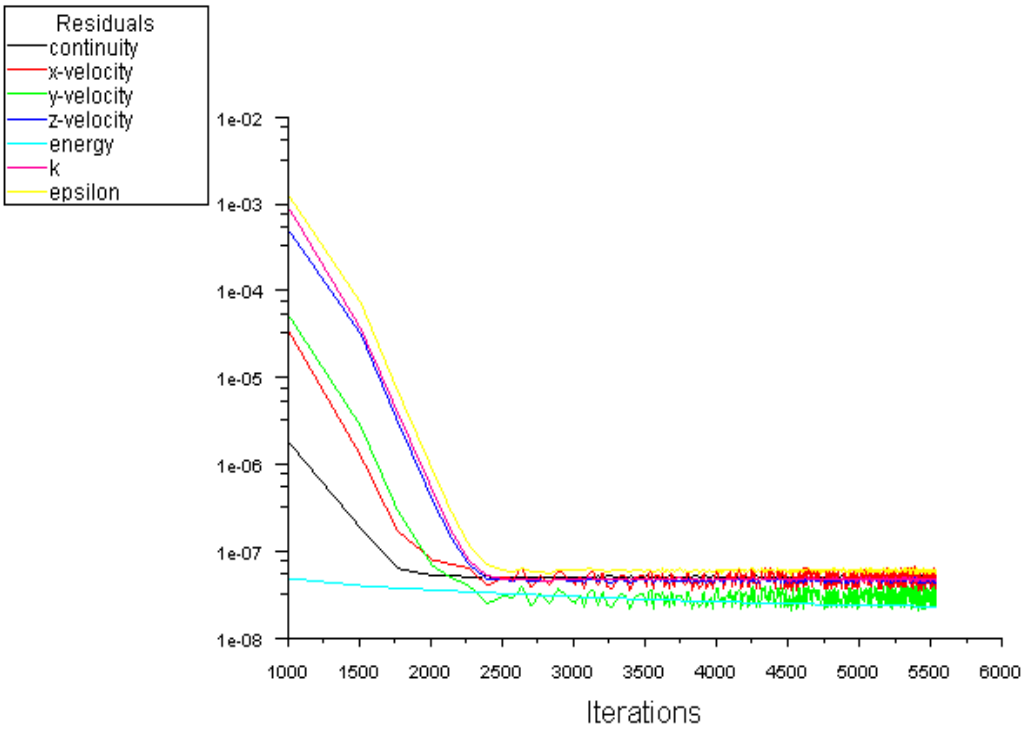

Figure 3.29. Residuals of a numerical model for turbulent flow solution.

➢ Under-Relaxation Factors

The constant under-relaxation factors (α) that are used in Equation 3.92 can be listed as;

for laminar flow;

- Pressure: 0.3
- Momentum : 0.7
- Energy: 1

for turbulent flow;

- Pressure: 0.3
- Momentum : 0.7
- Energy: 1
- TKE : 0.8 (for Turbulent Kinetic Energy)
- TDR: 0.8 (for Turbulent Dissipation Rate)

3.8. Numerical Calculation Details of Heat Transfer Coefficient and Pressure Drop

Ones computations are finalized, two important factors are calculated depending on Equation 3.89 and Equation 3.90, which are the commonly used factors in heat exchanger analysis. These factors are the Colbourn j factor that is the non-dimensional form of heat transfer, and the f-fanning friction factor that is the non-dimensional form of pressure drop.

$$j = \frac{Nu}{RePr^{1/3}} \tag{3.89}$$

$$f = \frac{\Delta P}{4L_c} \frac{D_h}{(1/2)\rho_m u_m^{\ 2}} \tag{3.90}$$

As shown in above equations, firstly the mean quantities of working fluid in OSF channel should be calculated. For that purpose the mean temperature of the fluid should be calculated. At this point two different calculation strategies are performed in order to compute the temperature value. Because the numerical problem is analyzed under two different thermal boundary conditions; constant heat flux, uniform temperature and the fluid temperature shows different behaviors under these two boundary conditions as shown in Figure 3.30 and Figure 3.31.

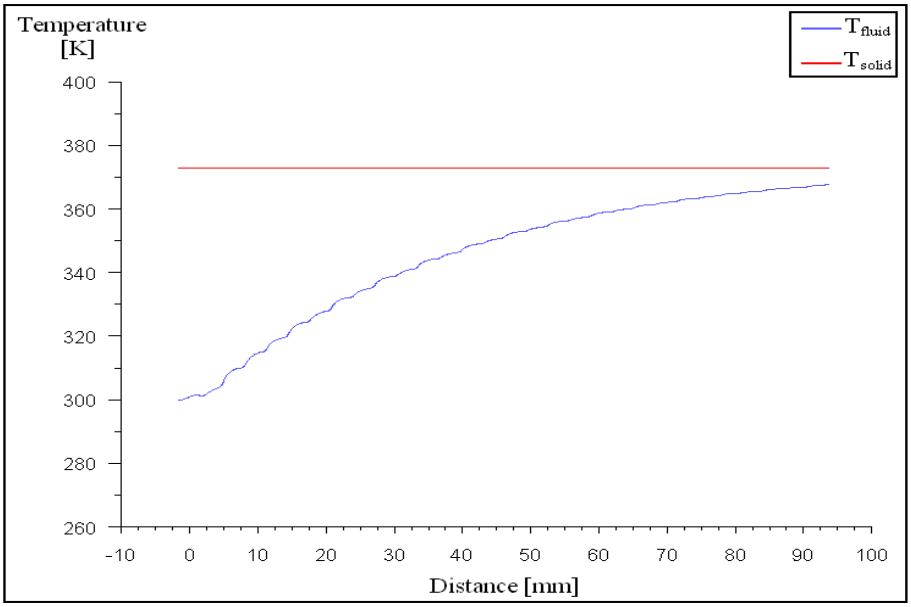

Figure 3.30. Fluid and surface temperature distributions under uniform temperature boundary condition

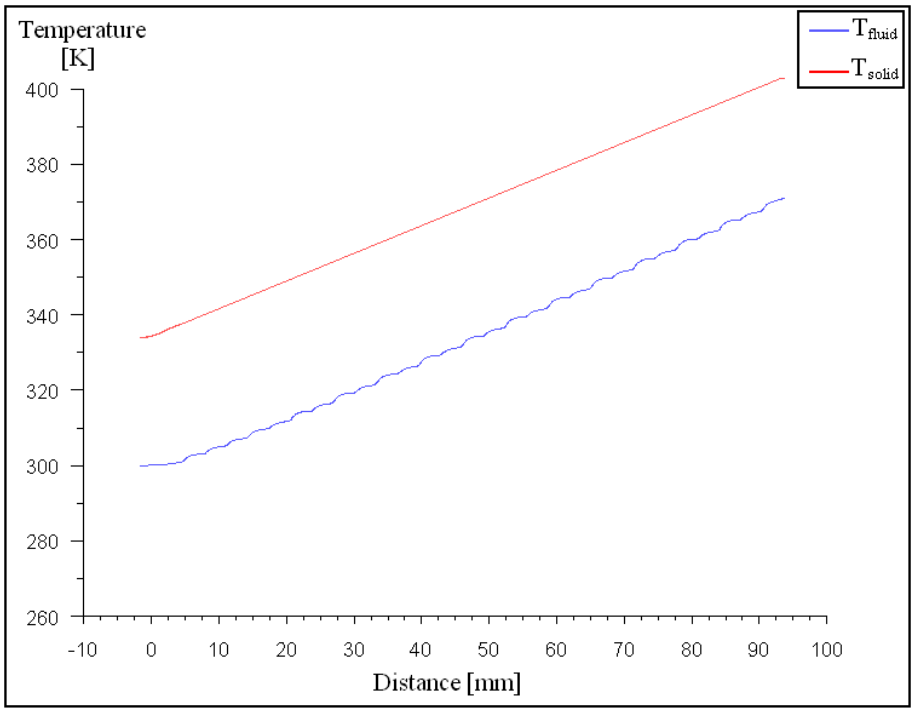

Figure 3.31. Fluid and surface temperature distributions under constant heat flux boundary condition

As shown in Figure 3.30 the mean temperature of fluid increases exponentially when the problem is analyzed under uniform temperature boundary condition however, upon analyzed under constant heat flux boundary condition, the mean temperature improves linearly. In order to get the mean temperature, firstly the fluid temperatures at inlet and outlet faces of OSF channel are calculated using the Equation 3.91 given below;

$$T = \frac{1}{A_c}\int T\, dA \tag{3.91}$$

For constant heat flux boundary condition the mean temperature of the working fluid can be calculated using the Equation 3.92

$$T_{m,fluid} = \frac{T_{inlet} + T_{outlet}}{2} \tag{3.92}$$

Whereas, for uniform temperature boundary condition firstly the logarithmic mean temperature should be calculated in order to get the mean temperature because of exponentially increasing fluid temperature. The log-mean temperature is calculated from Equation 3.93 as (Shah and Sekulic 2003);

$$\Delta T_{LM} = \frac{(T_{surface} - T_{inlet}) - (T_{surace} - T_{outlet})}{\ln\left(\frac{(T_{surface} - T_{inlet})}{(T_{surface} - T_{outlet})}\right)} \tag{3.93}$$

Then, the mean temperature of working fluid is calculated from Equation 3.94 for uniform temperature case (Shah and Sekulic 2003);

$$T_{m,fluid} = T_{surface} - \Delta T_{LM} \tag{3.94}$$

The fluid properties are obtained by substituting the mean temperature value into fluid properties equations given in section 3.3.2.

In order to compute the j factor given in Equation 3.90 the Reynolds, Nusselt, and Prandtl numbers are computed respectively with using following definitions;

$$Re = \frac{u_m D_h}{\upsilon} \tag{3.95}$$

$$Nu = \frac{h_{avg} D_h}{k} \tag{3.96}$$

$$Pr = \frac{\upsilon}{\alpha} \tag{3.97}$$

As seen in Equation 3.95, Equation 3.96 and also f-factor equation the equations depend on hydraulic diameter of OSF channel and it is defined as (Manglik and Bergles 1995);

$$D_h = \frac{4shl}{2[(sl + hl + th) + ts]} \tag{3.98}$$

The mean value of the velocity, u_m in Equation 3.95 and also in f-factor equation is calculated from average value of the velocities which are at inlet and outlet faces. Equations of the velocities and the mean velocity of them are given respectively,

$$u = \frac{1}{A_c} \int u dA \tag{3.99}$$

$$u_m = \frac{u_{inlet} + u_{outlet}}{2} \tag{3.100}$$

In order to calculate the average heat transfer coefficient on OSF walls, the numerically obtained local heat transfer coefficients are integrated over the OSF surface areas. The local heat transfer coefficient is calculated by using the Equation 3.39. Thus, Equation of the average heat transfer coefficient is given as follows;

$$h_{avg} = \frac{1}{A_{fin}} \int h dA \tag{3.101}$$

The pressure difference in the f-factor equation is calculated by subtracting the average pressure at inlet face from average pressure at outlet face of OSF. The pressure difference equation is given as;

$$\Delta P = P_{inlet} - P_{outlet} \tag{3.102}$$

The pressure value at outlet is kept equal to 0 as a boundary. Thus, only the mean pressure at inlet should be calculated. This pressure is calculated as;

$$P_{inlet} = \frac{1}{A_c} \int P dA \tag{3.103}$$

CHAPTER 4

EXPERIMENTAL ANALYSIS

The geometrical parameters of a flow channel with OSF given in Table 4.1 are used in the experimental analyses.

Table 4.1. Geometrical parameters of OSF used for experimental analyses.

Geometrical Parameters	Dimensions (mm)
Fin Length (L_f)	1.5
Fin Height (h)	3.8
Fin thickness (t)	0.2
Fin Size (s)	2.6
Channel Length (Ld)	200
Channel width	25
Channel height	4

This work investigates the pressure drop and average heat transfer coefficient for the channel with OSF where heat originated from the walls of the channel. Relations are experimentally investigated by changing the channel Reynolds number (by changing the flow rate) from 150 to 3500 in the OSF channel and could not be carried for 5000, due to the very high pressure drops. Water is used as a working fluid of the experiments.

4.1. The Flow Loop and Instrumentation

The schematic view of the experimental setup is illustrated in Figure 4.1. As seen from this figure, the instruments in the experimental setup may be explained under

two groups; first group is used for supplying water as working fluid to a test unit and the second one is the data acquisition. The instruments used in first group consist of

- A storage tank
- Water pump
- A filter
- Manual flow maters
- Test unit
- A heat exchanger and fan
- Adjusting valves

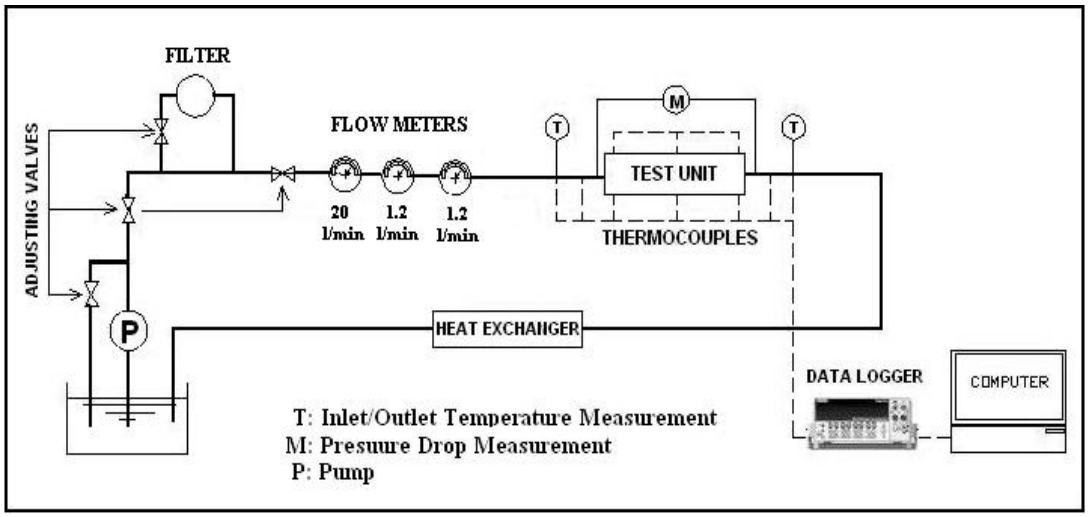

Figure 4.1. Schematic view of experimental setup.

The experimental loop can briefly be explained as: The water is stored in the tank which is also used a thermal mass in order to slow down the system response to a manageable level. A centrifuge pump is used to force the water to the test unit and also optionally through a filter (if need for filtering the water) and a set of flow meters. There are three manual flow meters; one with 0-20 l/min and other two with 0-1.2 l/min capacity which are all used in parallel. There are valves at the each flow meter entrance which are used to adjust the flow rate of the working fluid. The test unit part is the most important part of the experimental setup and detailed information about it is given in next section. A heat exchanger and an axial fan are used to transfer the built up heat in the water and therefore decrease the temperature of it. Temperature of the working fluid can not be allowed to exceed 60°C degrees since some of the construction

materials (Delrin) would lose too much of its strength and the integrity of the setup would be in danger. There are additional three adjusting valves are used for system operation; one for decreasing the flow rate and others for opening or closing some system units (such as filter unit). An open loop circulation is used to manage pressure levels and eliminate the negative effects of the expansions of the water. The instruments used in second group consist of

- Pressure transducer
- Multimeter
- Thermocouples
- Data-logger
- Power supplies
- Computer

Pressure is measured using a differential pressure transducer. The transducer is a silicon diaphragm that uses a wheat-stone bridge resistor network to measure the deflection. The excitation voltage is 24 VDC supplied by using a power supply and the output is from 4 to 20 mA. The pressure transducer is selected to give the highest level of accuracy, with a range of 0 to 5 PSIG. The output current is measured using a three-digit digital multimeter.

J-type thermocouples are used to measure the temperature data. This type of thermocouples consists of two different materials, constantan and iron. The two materials are connected each other at a point. If the connected point is touched to any object such as ice that is 0°C, then a potential difference exist between the different materials because of that the materials have different thermal conductivity. The potential difference is transferred to a data-logger in order to convert it to temperature. The measuring temperature data is kept by a computer. The photo of the experimental setup is illustrated in Figure 4.2.

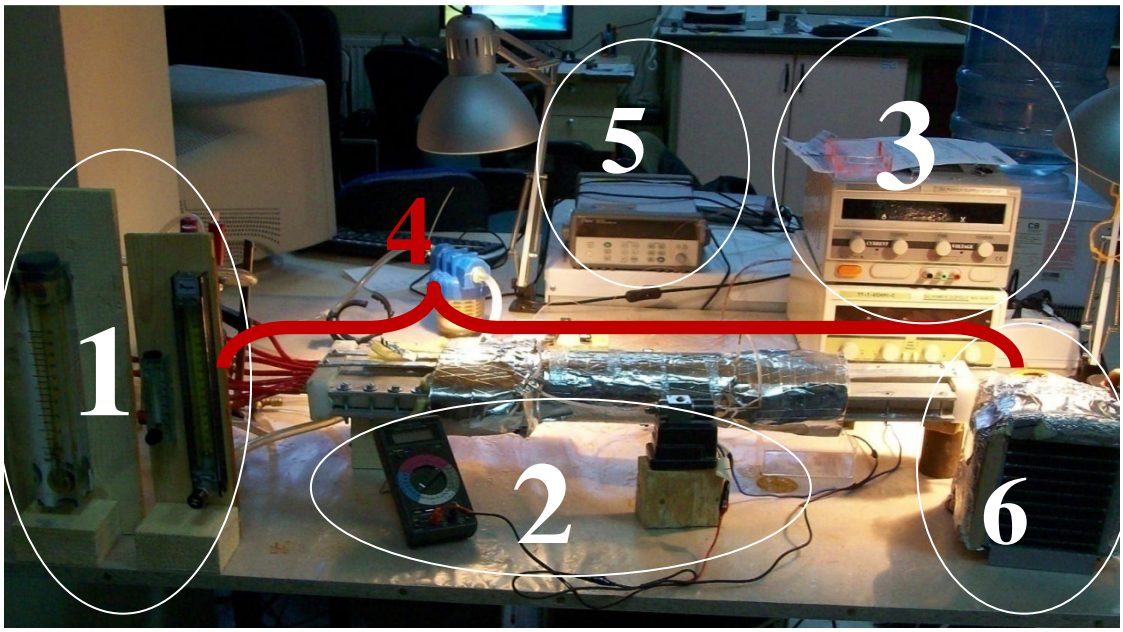

Figure 4.2. A scene from the experimental setup.

As shown in this figure, devices of the test unit are listed below;

1. Flow meters,
2. Pressure drop measuring unit,
3. Power supplies,
4. Test section,
5. Data logger,
6. Exchanger and fan.

4.2. Test Section

The test unit illustrated in Figure 4.3 consists of three regions. These are entrance, test and outlet regions. The entrance and outlet regions are made of delrin although test region is made of aluminium alloy.

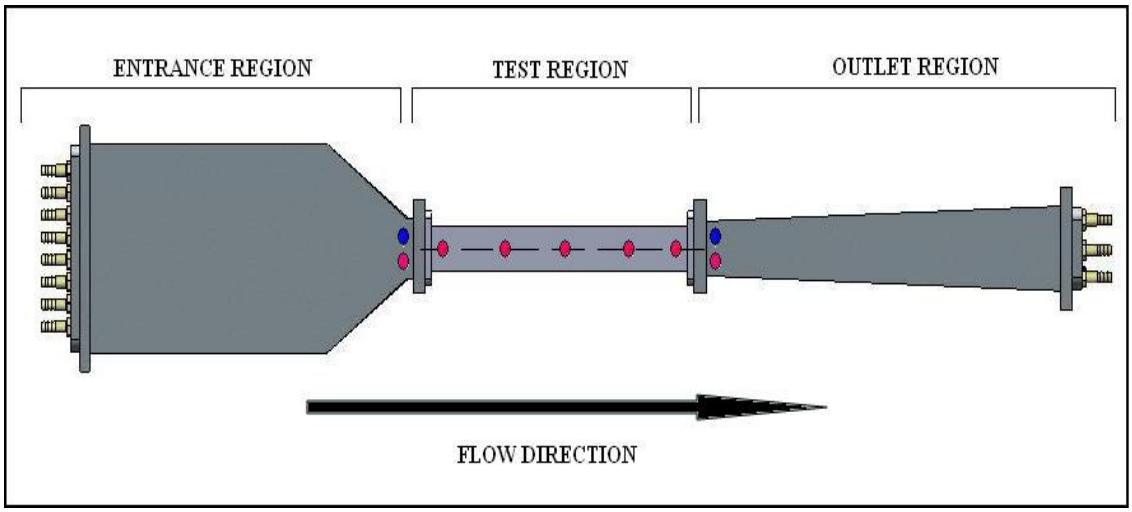

Figure 4.3. Test unit used for experimental analyses.

Fluid is being delivered uniformly to the entrance region with a 1-entrance-to-8-exit distributor which has a much bigger flow area the connected pipes and therefore minimal pressure drop as shown in Figure 4.4. The flow in the distributor is transferred to entrance region by eight hose fittings with small inner diameter (Φ3 mm).

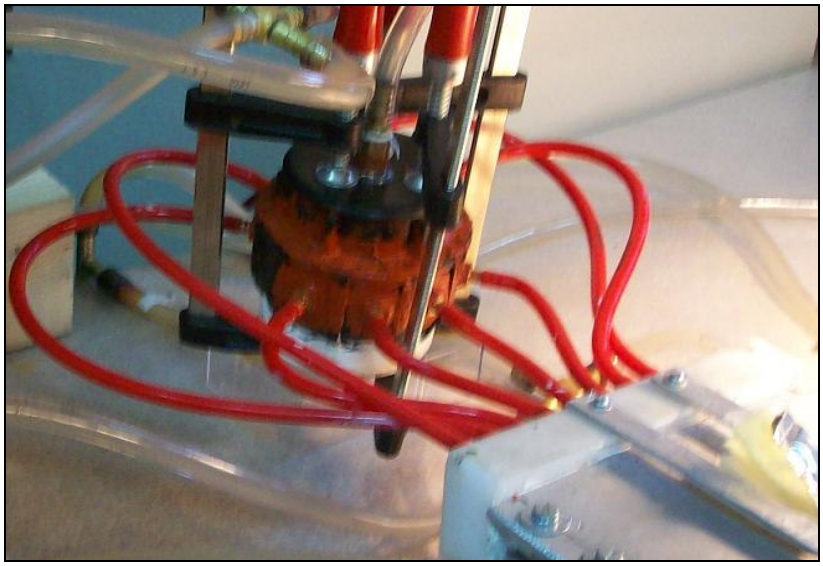

Figure 4.4. The distributor used in experimental setup

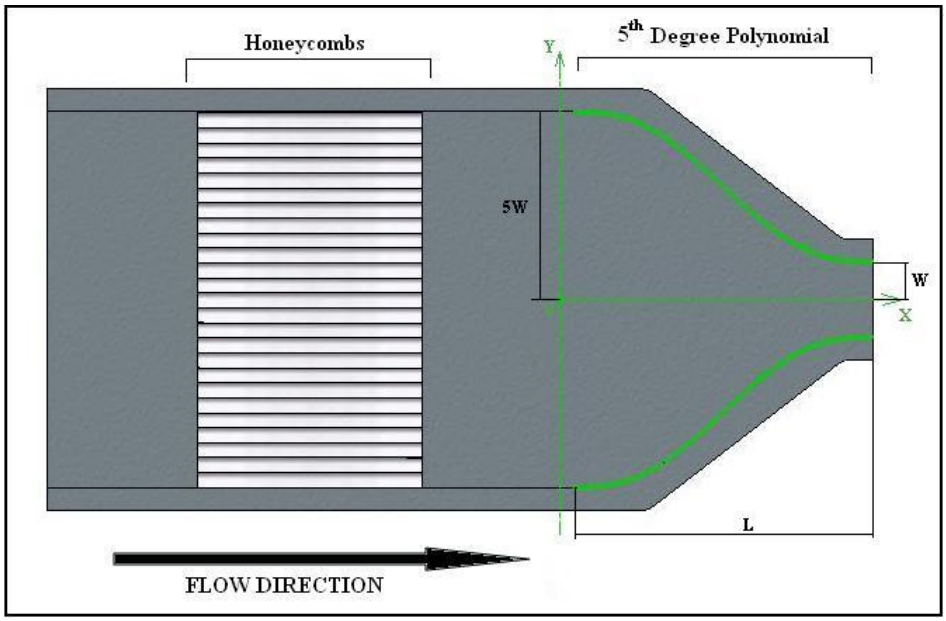

Figure 4.5. Entrance region.

Water from the distributor goes through the streamlined entrance region, shown in Figure 4.5. Flow first goes through a honeycombed region constructed with drinking straws of 75 mm long and 5 mm in diameter. This part helps to dissipate any large scale fluid motions that might be coming from distributor pipes. Flow than goes into the contraction which is designed as fifth degree polynomial in order to achieve a uniform velocity profile. This fifth degree polynomial is a widely used method in flow research facilities (gas or liquid) in order to obtain uniform velocity profile. The fifth degree polynomial equation and its boundary conditions are given as;

$$y = ax^5 + bx^4 + cx^3 + dx^2 + ex + f \tag{4.1}$$

$$x = 0 \quad y = 5W \tag{4.2}$$

$$\left.\frac{\partial y}{\partial x}\right|_{x=0} = 0 \tag{4.3}$$

$$\left.\frac{\partial^2 y}{\partial x^2}\right|_{x=0} = 0 \tag{4.4}$$

$$x = L \quad y = W \tag{4.5}$$

$$\left.\frac{\partial y}{\partial x}\right|_{x=L} = 0 \tag{4.6}$$

where **W** is the half wide of outlet part of the contraction region and **L** is the length of the region as shown in Figure 4.5.

As shown in Figure 4.3, there are two holes on the cover of the entrance region. One hole with blue point is used to measure the pressure at inlet of the test region and the other one with red point is used to measure the temperature of fluid at inlet of the test region. They are 5 mm and 5 mm off from the flange interface respectively. Pressure holes are carefully drilled and cleaned in order not to cause any error in the measurement.

As shown in Figure 4.6, another important part of the test unit is the test region. In this figure the film heater and the plate type heat exchanger used for analyzing of OFS are illustrated in “a” and a cut front view of the test region is shown in “b” and a cut view of the plate and OSF are given in “c”, and the real photo of the heat exchanger is illustrated in “d”. As mentioned earlier, the plate and also the OSF in it are made out of aluminum alloy and they are joined by brazing so that the thermal resistance between the fin and flat surfaces of the channel of the test region is minimal. Upon focusing on the figure 4-6-b, the test unit consists of seven parts. These are two insulated walls to prevent the heat transfer on plate surfaces to the ambient, two film heaters as heat sources, upper and lower parts of plate and a the OSF itself. As shown as red points in Figure 4.3, totally ten 32 AWG thermo-couples of J-type are placed on the upper and lower surfaces of the plate type heat exchanger in order to measure the local temperature data from the plate surfaces. Thermocouple connections are tested with continuity test before and after the experiments.

a)

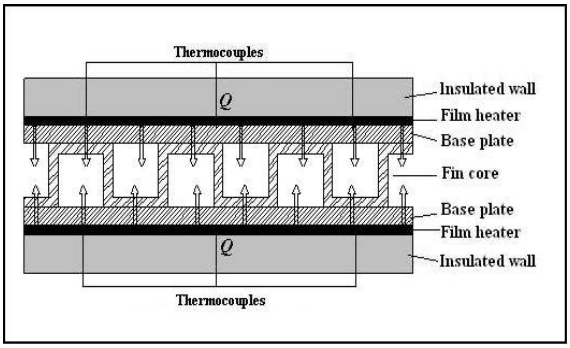

b)

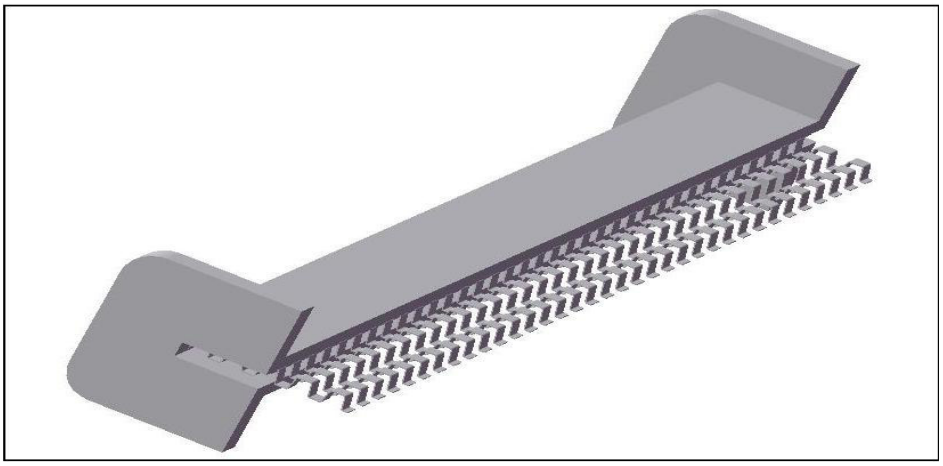

c)

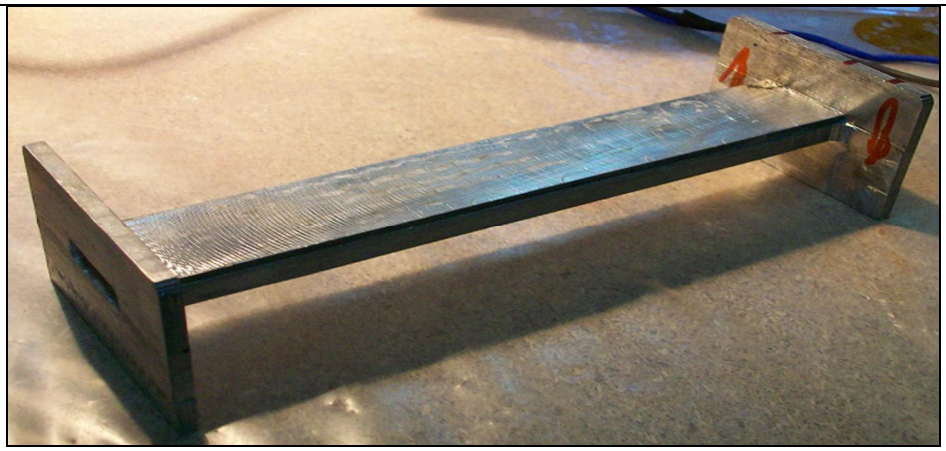

d)

Figure 4.6. Test Region and Its Parts.

Another part of the test unit is the outlet region, Figure 4.3. As shown in Figure 4.7, the outlet region is an expansion with a half angle of 2^{o}. Its purpose is to slowdown the flow

and increase the static pressure so that no effect from upstream would travel to test section and affect it.

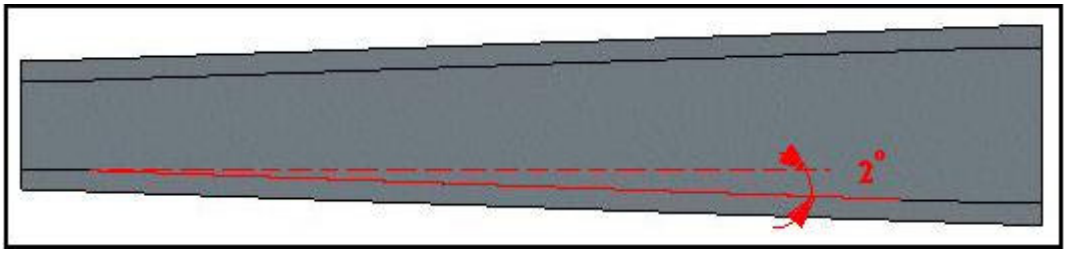

Figure 4.7. Outlet region

As shown in Figure 4.3, there are also two holes on the cover of the outlet region. One hole with blue point is used to measure the outlet pressure of the test region, other one with red point is used to measure the temperature of the fluid at outlet of the test region.

In summary, there are twelve points for measuring temperature and two points for measuring pressure. Two thermocouples on the either side of the test section are used to obtain the temperature difference of the water, and others on the channel wall are used to get the temperature difference of the upper and bottom surfaces of the heat exchanger along the flow direction.

The expanded fluid in the outlet region is collected by a collector which has three inlets and an outlet. The collector used in the test setup is illustrated in Figure 4.8.

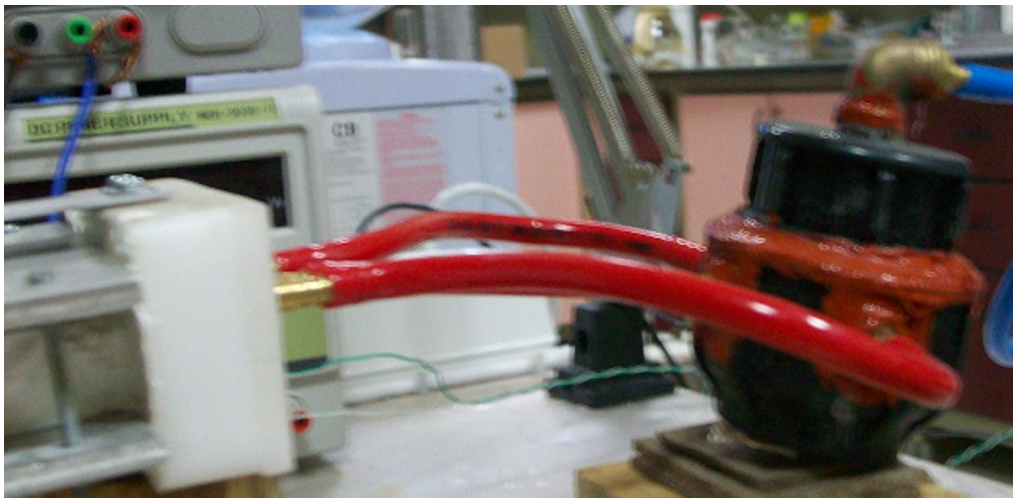

Figure 4.8. Collector

4.3. Test Procedure

It is ensured that the water used as working fluid for experimental analyses is first degassed by keeping it in the tank for a week. Since the gasses in the water may form bubbles which can stick on the heat transfer surfaces and affect the heat transfer and flow as well. In order to overcome this degassing problem, some precautions have to be taken into consideration; first, an open loop circulation system is used so that the bubbles can be taken out easily. Secondly, a huge volume storage tank is used so that not to entrain the bubbles in the circulation again. Later, the test unit is vibrated while the fluid is moving in it at the same time heat is supplied to it so that stuck bubbles can released from the surfaces.

An AC centrifugal pump is used to force the flow from the storage tank to test section through the parallel flow meters. The flow rate is manually adjustable by using the flow meters. The heat flow used is 165 W and is kept constant for all of the experiments. Then the measured temperature and temperature difference are viewed real time to make sure the heat transfer process reached the steady state. In this thesis for all experimental analyses the temperature differences between both measured points are waited to be stable because of decreasing analysis time, although the steady state situation in a flow occurs when the all measured temperatures achieve constant values with respect to time. When the flow is stable, the flow rate and also pressure drop are measured. Note that first adjusted flow rate value at the beginning of the experiments changes during the experiment due to temperature changes. Therefore it is a guessed value depending on the aimed Reynolds number and the experience of the experimentalist. Since, the properties of the fluid change when the fluid is heated.

4.4. Data Reduction for Heat Transfer and Pressure Drop Coefficients

Following the completion of data gathering, two important factors; Colbourn j factor and the f-fanning friction factor are calculated depending on Equation 3.89 and Equation 3.90 given in chapter three.

In order to calculate these factors, firstly the mean quantities of working fluid in OSF channel should be calculated. For that purpose the mean temperature of the fluid and also the mean temperature of the surfaces of test region must be accurately calculated. Although all of the temperature data is recorded to make sure of the steady state regime, only final twenty data is used as averages for the data reduction in order to reduce scatter.

The mean temperature of the working fluid can be calculated using the Equation 3.92 given in chapter three. The fluid properties are obtained by substituting the mean temperature value into fluid properties equations given in section 3.3.2.

Since the experiment is performed under the constant heat flux thermal boundary condition, its calculation strategy is nearly the same as to the numerical analysis with constant heat flux case. There is only one difference which must be mentioned is the way to calculate the average heat transfer coefficient of the OSF. In order to calculate the average heat transfer coefficient, Equations 4.7 and 4.8 (Shah and Sekulic 2003), depending on overall heat transfer coefficient of the heat exchanger and overall efficiency of it are used.

$$\frac{1}{UA} = \frac{t_p}{A_p k_p} + \frac{1}{A h_{avg} \eta_o} \;;\; U = \frac{Q}{\Delta T_{LM} A} \text{ and } Q = \dot{m} Cp (T_{out} - T_{in}) \tag{4.7}$$

$$\eta_o = 1 - \frac{A_{fin}}{A}(1 - \eta_{fin}) \tag{4.8}$$

where the fin efficiency is defined as

$$\eta_{fin} = \frac{\tanh(ml)}{ml} \;;\; m = \sqrt{\frac{2h_{avg}}{k_{fin}}} \text{ and } l = \frac{h}{2} - t \tag{4.9}$$

As shown in Equation 4.7 and 4.8, they are coupled to each other, thus they are solved iteratively. In these equations, the total heat transfer surface area of whole heat exchanger shown as "**A "**, is obtained from sum of the plate and the fin areas where the heat transfer occur (Shah and Sekulic 2003).

The logarithmic mean temperature difference is computed by using Equation 3.98 given in numerical procedure part. The surface temperature appearing in this equation is computed from the average value of measured surface temperatures from totally ten points on the test region, where the five points are on one side of it and other five points are on opposite side. The mean velocity of the flow is computed from measured flow rate to compute the Reynolds number. Noted that other equations used in this thesis are the same to the equations given in numerical analysis procedure part.

4.5. Experimental Uncertainties

The uncertainty analysis is a procedure used to quantify data validity and accuracy. The uncertainty of a measured (or a reduced from measured) parameter is determined by the method of evaluating the bias and precision errors. The following equation is used to calculate the uncertainty in a measured quantity R = R(x_1, x_2, ….., x_n) (Kline and McClintock 1953);

$$U_R = \sqrt{\left(\frac{x_1}{R}\frac{\partial R}{\partial x_1}U_1\right)^2 + \left(\frac{x_2}{R}\frac{\partial R}{\partial x_2}U_2\right)^2 + ... + \left(\frac{x_n}{R}\frac{\partial R}{\partial x_n}U_n\right)^2} \qquad (4.10)$$

where U, R, and x are respectively; uncertainty interval, result, and variable.

The measuring instruments used in the test setup have different uncertainties. The pressure transducer has an uncertainty of ± 1.724 Pa (± 0.8 mA). The power supply has also an uncertainty of ± 0.5 W. The uncertainties for geometrical parameters are assumed to be ±0.1 mm. The uncertainties of the flow meters are ± 0.05 l/min for low scale and ± 0.25 l/min for high scale meters (These are guessed quantities from meter scales).

The temperature reading has an uncertainty as well. The uncertainty of temperature directly reflects on to for the temperature difference between inlet and outlet of the working fluid which is needed to calculate the heat transfer rate and also the logarithmic mean temperature difference which are again used to calculate the

overall heat transfer coefficient of the heat exchanger. Uncertainty of temperature difference is determined by using f-distribution technique. For that reason twenty temperature data are taken into consideration. As an example, these data tabulated in Table 4.2 are selected after the temperature difference becomes nearly constant. The standard deviation s_{m_i} of the results of the both temperature differences are obtained by using the following equations (Kline and McClintock 1953):

$$s_{m_i} = \sqrt{\frac{1}{n-1}\sum_{j=1}^{n}(m_i(j) - \overline{m_i})^2} \tag{4.11}$$

where $\overline{m_i}$ is the average

$$\overline{m_i} = \frac{1}{n}\sum_{j=1}^{n} m_i(j) \tag{4.12}$$

The standard deviation for the temperature difference of the fluid is calculated to be 0.00071 and for the logarithmic mean temperature difference is calculated to be 0.000164. A confidence interval for the temperature differences with 95% confidence level is obtained as T ± 1,729s_{m_i} by using Student t-distribution. Therefore, the uncertainties for the temperature difference of fluid and the logarithmic mean temperature difference are calculated as ±0.00123 ^{o}C and ±0.0003 ^{o}C, respectively (Kline and McClintock 1953). Indeed, the uncertainties are very small because they only consist of random errors. It is known that the uncertainty consists of the method of evaluating the bias and random errors. Generally the bias errors are greater than random ones. Thus, the uncertainty of temperature reading is assumed as ± 0.1 °C from thermocouple catalog.

The resulting uncertainties are calculated for the all required quantities, for a median case (Re = 2144). One of the quantities is Reynolds number. The computing equation for the Reynolds number is

$$Re = \frac{u.D_h}{\nu} = Re(u, D_h) \tag{4.13}$$

In order to calculate the uncertainty interval of the Reynolds number, firstly, the uncertainties for the velocity u and also for the hydraulic diameter are need to be

calculated. The velocity is a function of volumetric flow rate and cross-section area of the OSF.

$$u = \frac{\dot{V}}{A_c} \tag{4.14}$$

Table 4.2. Temperature data measured from experiment.

Sample	$T_{f\,in}$	$T_{f\,out}$	$T_{w\,mean}$	ΔT	ΔT_{LN}
1	35,76	36,27	38,76	0,51	2,74
2	35,76	36,29	38,76	0,53	2,73
3	35,76	36,26	38,77	0,51	2,75
4	35,74	36,27	38,76	0,52	2,75
5	35,75	36,27	38,75	0,52	2,74
6	35,76	36,27	38,76	0,51	2,74
7	35,74	36,25	38,75	0,51	2,74
8	35,75	36,26	38,75	0,51	2,73
9	35,74	36,26	38,76	0,52	2,75
10	35,74	36,25	38,75	0,52	2,74
11	35,74	36,26	38,76	0,52	2,75
12	35,74	36,26	38,76	0,52	2,76
13	35,75	36,26	38,72	0,51	2,71
14	35,75	36,27	38,75	0,52	2,73
15	35,73	36,25	38,75	0,52	2,76
16	35,74	36,25	38,74	0,51	2,73
17	35,73	36,26	38,76	0,53	2,75
18	35,73	36,25	38,72	0,52	2,72
19	35,73	36,25	38,75	0,52	2,75
20	35,73	36,24	38,73	0,51	2,74

The volumetric flow rate are measured as 2.8 l/min by using two flow meters ($\dot{V}_h$ =2 ±0.25 l/min for high scale, $\dot{V}_l$ = 0.8±0.05 l/min for low scale)

$$\dot{V} = \dot{V}_h + \dot{V}_l \tag{4.15}$$

The relative uncertainties in volumetric flow rate for high and low scale meters are calculated as

$$U_{\dot{V}_h} = \pm\frac{0.25\ l/min}{2\ l/min} = \pm 0.125 \ and \ U_{\dot{V}_l} = \pm\frac{0.05\ l/min}{0.8\ l/min} = \pm 0.063$$

Thus, the relative uncertainty in the total volumetric flow rate is calculated by using the Equation 4.10.

$$U_{\dot{V}} = \pm\sqrt{\left(\frac{V_h}{V}\frac{\partial V}{\partial V_h}U_{V_h}\right)^2 + \left(\frac{V_l}{V}\frac{\partial V}{\partial V_l}U_{V_l}\right)^2}$$

$$U_{\dot{V}} = \pm\sqrt{\left(\frac{2}{2.8} * (1) * (\pm 0.125)\right)^2 + \left(\frac{0.8}{2.8} * (1) * (\pm 0.063)\right)^2}$$

$$U_{\dot{V}} = \pm\ 0.09 \ \text{ or } U_{\dot{V}} = \pm\ 9\ \%$$

The cross-section area of OSF is related to fin size s and also fin height h.

$$A_c = sh \tag{4.16}$$

The relative uncertainties of the fin size and fin height are

$$U_s = \pm\frac{0.1\ mm}{2.6\ mm} = \pm 0.038 \ \ and \ \ U_h = \pm\frac{0.1\ mm}{3.8\ mm} = \pm 0.026$$

Thus, the relative uncertainty in the area is calculated by using Equation 4.10 as

$$U_{\dot{A}_c} = \pm\sqrt{\left(\frac{s}{A_c}\frac{\partial A_C}{\partial s}U_s\right)^2 + \left(\frac{h}{A_c}\frac{\partial A_C}{\partial h}U_h\right)^2}$$

$$U_{A_c} = \pm\ 0.05 \quad \text{or} \quad U_{A_c} = \pm\ 5\ \%$$

Therefore, the relative uncertainty of the velocity is calculated by using Equation 4.10 and 4.14

$$U_u = \pm\sqrt{\left(\frac{V}{u}\frac{\partial u}{\partial V}U_V\right)^2 + \left(\frac{A_c}{u}\frac{\partial u}{\partial A_c}U_{A_c}\right)^2}$$

$$U_u = \pm 0.10 \quad \text{or} \quad U_u = \pm 10\ \%$$

The hydraulic diameter of the OSF is calculated by using Equation 4.17

$$\mathrm{D_h} = \frac{4\mathrm{shl}}{2[(\mathrm{sl} + \mathrm{hl} + \mathrm{th}) + \mathrm{ts}]} \tag{4.17}$$

As shown the equation above, the hydraulic diameter is related t fin geometrical parameters. Thus firstly the relative uncertainties in these parameters should be calculated. The uncertainties in fin size and fin height have been calculated above. So,

$$U_t = \pm\frac{0.1\ mm}{0.2\ mm} = \pm 0.5 \ \ and \ \ U_l = \pm\frac{0.1\ mm}{1.5\ mm} = \pm 0.066$$

Therefore, the relative uncertainties in the hydraulic diameter is calculated by using Equation 4.10 and 4.17

$$U_{D_h} = \pm\sqrt{\left(\frac{s}{D_h}\frac{\partial D_h}{\partial s}U_s\right)^2 + \left(\frac{h}{D_h}\frac{\partial D_h}{\partial h}U_h\right)^2 + \left(\frac{t}{D_h}\frac{\partial D_h}{\partial t}U_t\right)^2 + \left(\frac{l}{D_h}\frac{\partial D_h}{\partial l}U_l\right)^2}$$

$$U_{D_h} = \pm 0.01 \quad \text{or} \quad U_{D_h} = \pm 1\ \%$$

Finally the relative uncertainty of the Reynolds number is calculated as

$$U_{\dot{R}e} = \pm\sqrt{\left(\frac{u}{Re}\frac{\partial Re}{\partial u}U_u\right)^2 + \left(\frac{D_h}{Re}\frac{\partial Re}{\partial D_h}U_{D_h}\right)^2}$$

$$U_{Re} = \pm 0.103 \quad \text{or} \quad U_{Re} = \pm 10.30\ \%$$

In order to calculate the uncertainties in the heat transfer rate Q and overall heat transfer coefficient U of the heat exchanger, firstly the relative uncertainties in the temperature difference of working fluid and in the logarithmic temperature difference should be computed. The temperature differences are given in Equation 4.18 and 4.19 respectively.

$$\Delta T = T_{f-out} - T_{f-in} \tag{4.18}$$

$$\Delta T_{LM} = \frac{(T_{surface} - T_{inlet}) - (T_{surace} - T_{outlet})}{\ln\left(\frac{(T_{surface} - T_{inlet})}{(T_{surface} - T_{outlet})}\right)} \tag{4.19}$$

The relative uncertainties for these temperatures are calculated as

$$U_{T_{f-out}} = \pm\frac{0.1\ C}{36.57\ C} = \pm 0.0027 \ \ and \ \ U_{T_{f-out}} = \pm\frac{0.1\ C}{35.76\ C} = \pm 0.0028$$

$$U_{T_s} = \pm\frac{0.1\ C}{39.43\ C} = \pm 0.0025$$

The uncertainty for the temperature difference is calculated by using Equation 4.10 and 4.18

$$U_{\Delta T} = \pm\sqrt{\left(\frac{T_{f-in}}{\Delta T}\frac{\partial \Delta T}{\partial T_{f-in}}U_{T_{f-in}}\right)^2 + \left(\frac{T_{f-out}}{\Delta T}\frac{\partial \Delta T}{\partial T_{f-out}}U_{T_{f-out}}\right)^2}$$

$$U_{\Delta T} = \pm\ 0.12 \quad \text{or} \quad U_{\Delta T} = \pm\ 12\ \%$$

The uncertainty for the logarithmic temperature difference is calculated by using Equation 4.10 and 4.19

$$U_{\Delta T_{LM}} = \pm\sqrt{\left(\frac{T_{fin}}{\Delta T_{LM}}\frac{\partial \Delta T_{LM}}{\partial T_{fin}}U_{T_{fin}}\right)^2 + \left(\frac{T_{fout}}{\Delta T_{LM}}\frac{\partial \Delta T_{LM}}{\partial T_{fout}}U_{T_{fout}}\right)^2 + \left(\frac{T_s}{\Delta T_{LM}}\frac{\partial \Delta T_{LM}}{\partial T_s}U_{T_s}\right)^2}$$

$$U_{\Delta T_{LM}} = \pm\ 0.03 \quad \text{or } U_{\Delta T_{LM}} = \pm\ 3\ \%$$

The heat transfer rate is calculated from below equation

$$Q = \dot{m} C_p \Delta T = Q(\dot{m}, \Delta T) \tag{4.20}$$

The relative uncertainty in the heat transfer rate is calculated by using Equation 4.10 and 4.20

$$U_Q = \pm \sqrt{\left(\frac{m}{Q}\frac{\partial Q}{\partial m} U_m\right)^2 + \left(\frac{\Delta T}{Q}\frac{\partial Q}{\partial \Delta T} U_{\Delta T}\right)^2}$$

$$U_Q = \pm 0.15 \quad \text{or} \quad U_Q = \pm 15\ \%$$

The overall heat transfer coefficient is calculated from below equation.

$$U = \frac{Q}{\Delta T_{LM} A} = U(Q, \Delta T_{LM}) \tag{4.21}$$

The relative uncertainty in the overall heat transfer coefficient is calculated by using Equation 4.10 and 4.21

$$U_U = \pm \sqrt{\left(\frac{Q}{U}\frac{\partial U}{\partial Q} U_Q\right)^2 + \left(\frac{\Delta T_{LM}}{U}\frac{\partial U}{\partial \Delta T_{LM}} U_{\Delta T_{LM}}\right)^2}$$

$$U_U = \pm 0.1565 \quad \text{or} \quad U_U = \pm 15.65\ \%$$

The average heat transfer coefficient is calculated from below equation.

$$h = \frac{1}{\frac{1}{U} - \frac{t}{k A_w} A} = h(U, t) \tag{4.22}$$

The relative uncertainty in the average heat transfer coefficient is calculated by using Equation 4.10 and 4.22

$$U_h = \pm\sqrt{\left(\frac{U}{h}\frac{\partial h}{\partial U}U_U\right)^2 + \left(\frac{t}{h}\frac{\partial h}{\partial t}U_t\right)^2}$$

$$U_h = \pm 0.1382 \quad \text{or} \quad U_h = \pm 13.82\ \%$$

The Nusselt number is calculated from below equation.

$$Nu = \frac{hD_h}{k} = Nu(h, D_h) \tag{4.23}$$

The relative uncertainty in the Nusselt number is calculated by using Equation 4.10 and 4.23

$$U_{Nu} = \pm\sqrt{\left(\frac{h}{Nu}\frac{\partial Nu}{\partial h}U_h\right)^2 + \left(\frac{D_h}{Nu}\frac{\partial Nu}{\partial D_h}U_{D_h}\right)^2}$$

$$U_{Nu} = \pm 0.1385 \quad \text{or} \quad U_{Nu} = \pm 13.85\ \%$$

The Colbourn j factor is calculated from below equation.

$$j = \frac{Nu}{RePr^{1/3}} = j(Nu, Re) \tag{4.24}$$

The relative uncertainty in the Colbourn j factor is calculated by using Equation 4.10 and 4.24

$$U_j = \pm\sqrt{\left(\frac{Nu}{j}\frac{\partial j}{\partial Nu}U_{Nu}\right)^2 + \left(\frac{Re}{j}\frac{\partial j}{\partial Re}U_{Re}\right)^2}$$

$$U_j = \pm 0.1725 \quad \text{or} \quad U_j = \pm 17.25\ \%$$

The pressure drop in the OSF channel is measured as 5.14 A ±0.8 mA. Thus, The relative uncertainty in the pressure drop is calculated as

$$U_{\Delta P} = \pm\frac{0.8\ e{-}03}{5.14} = \pm 0.000156$$

The fanning friction factor f is calculated from below equation.

$$f = \frac{\Delta P}{4L_c} \frac{D_h}{(1/2)\rho_m u_m^2} \tag{4.25}$$

As shown the above equation, the fanning friction factor is as a function of ΔP, D_h, u. Therefore, the relative uncertainty in the fanning friction factor is calculated as

$$U_f = \pm \sqrt{\left(\frac{\Delta P}{f}\frac{\partial f}{\partial \Delta P} U_{\Delta P}\right)^2 + \left(\frac{Re}{f}\frac{\partial f}{\partial Re} U_{Re}\right) + \left(\frac{u}{f}\frac{\partial f}{\partial u} U_u\right)^{2^2}}$$

$$U_f = \pm 0.145 \quad \text{or} \quad U_f = \pm 14.50\ \%$$

The calculated uncertainties of the required quantities are tabulated in Table 4.3 below.

Tablo 4.3. Uncertainty analysis for required quantities in thesis.

Region	**Heat Transfer**			**Pressure Drop**	
Re	**h**	**Nu**	**j**	**ΔP**	**f**
± 0.103	± 0.138	± 0.1385	± 0.1740	±0.00015	± 0.1450
10.30 %	13.80 %	13.85 %	17.40 %	15.6 %	14.50 %

CHAPTER 5

RESULTS AND DISCUSSION

The main emphasis of this thesis is to obtain an optimum numerical procedure to successfully analyze OSFs backed by experimental verifications. For that purpose, two issues are taken into consideration. One of them is creating a numerical model for an OSF that was already experimentally analyzed. Secondly, another OSF is tested experimentally by ourselves and modeled using same technique in order to ensure the accuracy of the procedure. Since the later used fin has different geometry and it has never been analyzed yet. The studied issues briefly are;

- Determining the average heat transfer coefficient and pressure drop in OSF at different Reynolds numbers,
- Determining the effect of Prandtl number on the heat transfer rate and pressure drop,
- Determining the effects of the two thermal boundary conditions on heat transfer and pressure drop.

5.1. Comparison of the Numerical Model with an Experimental Study

A comparison of our numerical results with an experimental study conducted by Kays and London (1964) is performed in order to test the reliability of the numerical models. In this thesis, only the OSF with the code of 1/8-16.00(D) from the Kays and London study is taken into consideration, due to the fact that their corresponding Reynolds numbers are very close to our interest which is between 200 and 5000. The geometrical properties of the OSF are given in Table 5.1

Table 5.1. The Geometrical properties of OSF with code number 1/8-16.00(D).

Geometrical Parameters	Dimensions (mm)
Fin Length (L_f)	3.175
Fin Height (h)	3.006
Fin thickness (t)	0.152
Fin Size (s)	1.434
Channel Length (L_c)	93.25

In Kays and London's experimental study, a cross-flow heat exchanger is employed as a test section, as shown in Figure 5.1. This setup, in general, consists of the following basic elements on the unknown side; a test section, a fluid metering device, a fluid pumping device, temperature measurement devices. Similar devices are also used on the known side. Air is used on the unknown-side while steam is used on the known-side. In their experiments, the flow rates on both fluid sides of the exchanger are set at constant predetermined values. Once the steady-state conditions are achieved, the fluid temperatures and also the pressures upstream and downstream of test section on both fluid sides are measured. The tests are repeated with different flow rates on the unknown side to cover the desired range of Reynolds number for the j and f factors vs. Re characteristics (Shah and Sekulic 2003).

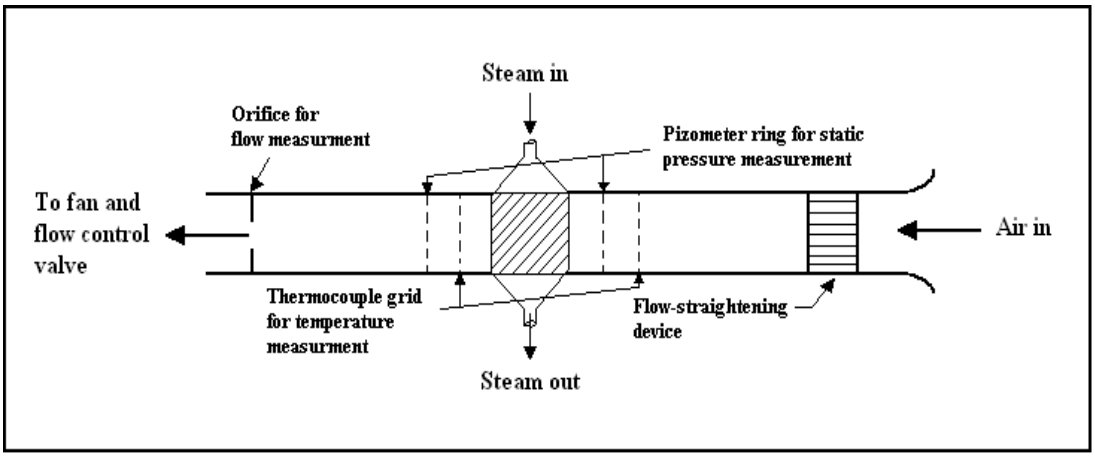

Figure 5.1. Schematic view of test setup used by Kays and London (Source: Shah and Sekulic 2003).

Since the heat capacity ratio of air versus condensing steam is almost equal to zero, condensing steam supplies an uniform temperature on the known-side of OSF.. A numerical model of the OSF with the geometrical dimensions given in Table 5.1 is created in the present study to accomplish the comparison of the numerical results with the experimental results of Kays and London. The numerical model and its meshes are presented in Figure 5.2.

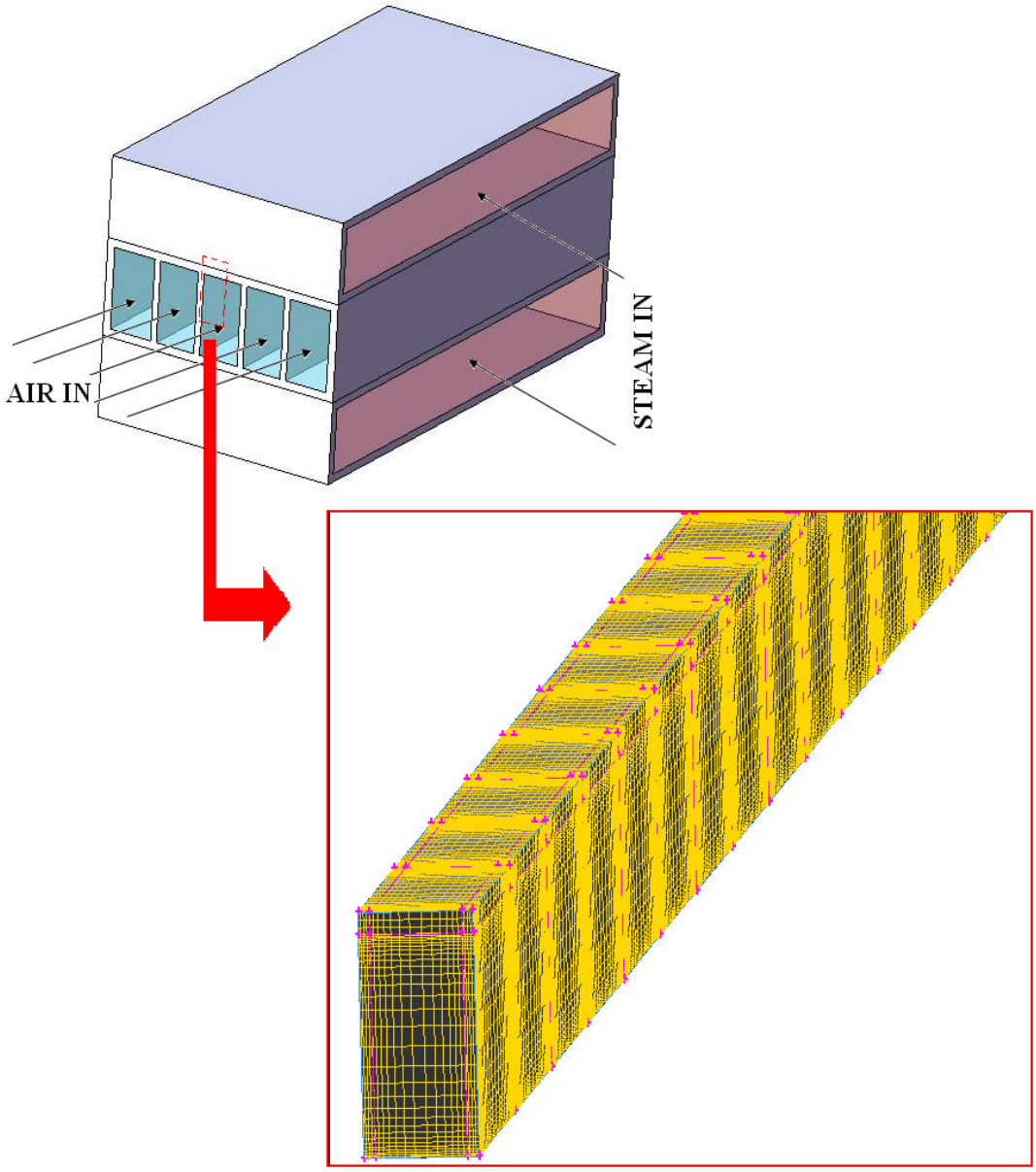

Figure 5.2. A numerical model for the OSF experimentally analyzed by Kays and London.

As shown in figure above, modeled part of the domain contains a wall junction, and a quarter part of the air channel including an OSF (or unknown side) and a uniform temperature on the steam side. This modeling approach makes use of geometrical symmetries and therefore results in a much simpler model and a drastic decrease the computational time. Detailed information about other boundary conditions, governing equations and also mesh independence analysis for the numerical model are given in chapter three in this thesis. The numerical analyses for this model are conducted by assuming that the flow is laminar and steady-state in the range of Reynolds number from 200 to 5000. The Colbourn j factor that is the non-dimensional form of convective heat transfer coefficients and the fanning friction factor-f that is the non-dimensional form of pressure drop from our numerical analyses for the OSF are compared with the experimental results of Kays and London (1964) and also the results obtained from correlations developed by Manglik and Bergles (1995) in Figures 5.3 and 5.4, respectively. Some information about the correlation equations are mentioned in chapter two and also the results obtained from the correlations developed by Manglik and Bergles are given in Table 2.1 in that chapter.

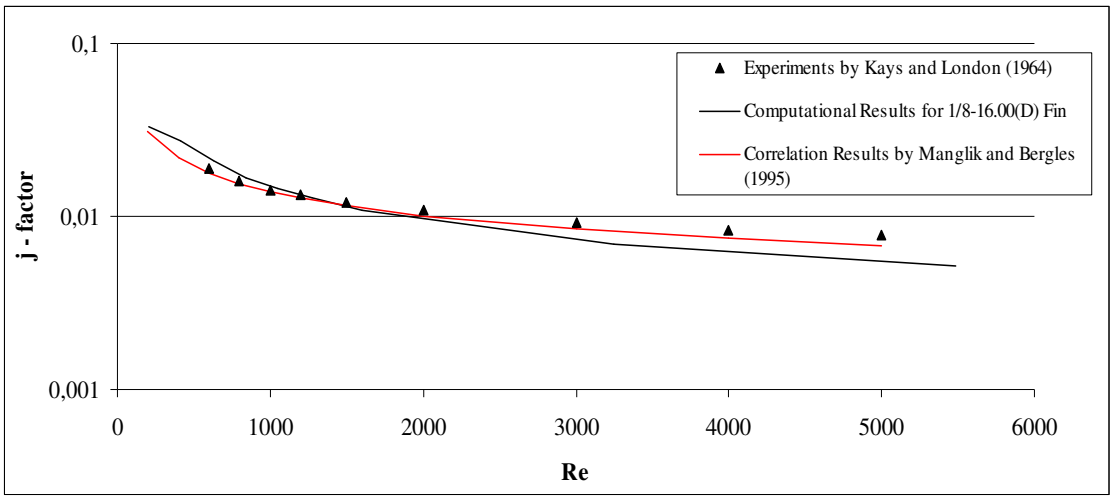

Figure 5.3. Comparison of the numerical results of the present study with the experimental results of Kays and London (1964) and the results obtained from correlations of Manglik and Bergles (1995) for Colbourn j factor.

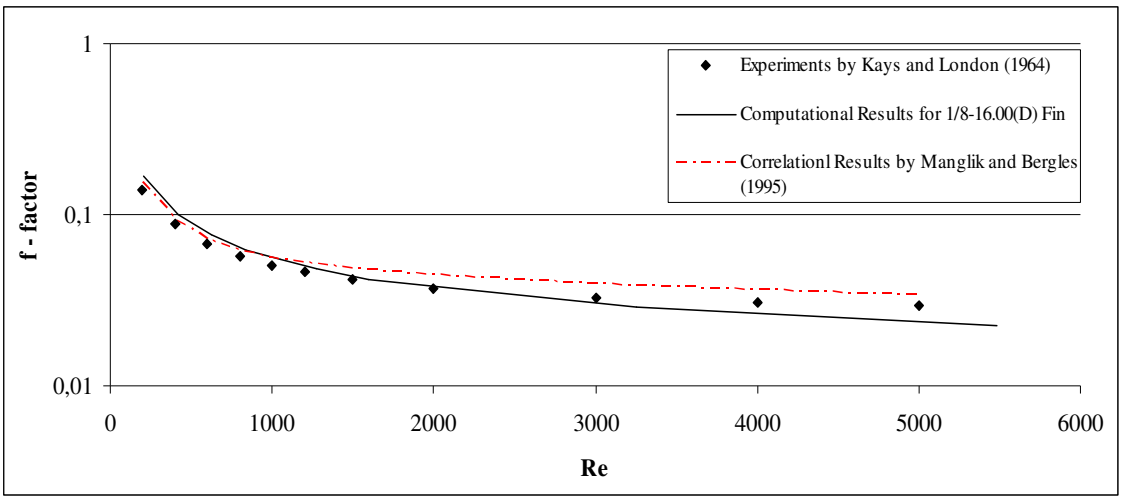

Figure 5.4. Comparison of the numerical results of the present study with the experimental results of Kays and London (1964) and the results obtained from correlations of Manglik and Bergles (1995) for Fanning friction f factor.

It can be seen from the figures that there is a considerably good agreement between the numerical results of present study and the experimental results of Kays and London (1964) for both Colbourn j factor and fanning friction factor f. As shown in Figure 5.3, since the correlations of Manglik and Bergles (1995) are obtained by curve fitting to the results of Kays and London (1964), their agreements should not surprise. The numerical results for j factor of the Reynolds number greater than 2000 start under-predicting the experiments, and the difference between experimental and numerical results increases with increasing Reynolds number. As shown in Figure 5.4, the f factor of the same numerical analyses shows a much satisfactory agreement with the same experimental data at even higher Reynolds numbers (Re~3000), but the results of Manglik and Bergles (1995) starts over-predicting the experiments at an earlier Reynolds number. The main possible reason of the values being underpredicted after a certain Reynolds number may be that the flow in the OSF channels changes a regime. Note that the numerical analyses are conducted under laminar flow assumption for all of the Reynolds numbers, therefore lower values of the j and the f factors for higher Reynolds numbers are expected. Detailed information about the effect of flow regime is given in next section of this chapter. It is concluded that the numerical results for j and f under a laminar case seem to be reliable up to Reynolds numbers of 2000 and 3000 respectively. Remember that the ordinate of the given figures are in logarithmic scale

which magnifies smaller values. Therefore the disagreement between numerics and the experiments are really small.

5.2. Effect of Flow Regime

Firstly, a numerical model based on the study of Kays and London (1964) is performed in order to investigate the effect of the flow regime. The average heat transfer coefficient and the pressure drop in the OSF channel are compared with respect to Reynolds number. As shown in Figures 5.5 – 5.7, the heat transfer coefficient and its non-dimensional forms, Nusselt number and the Colburn j factor, are given respectively.

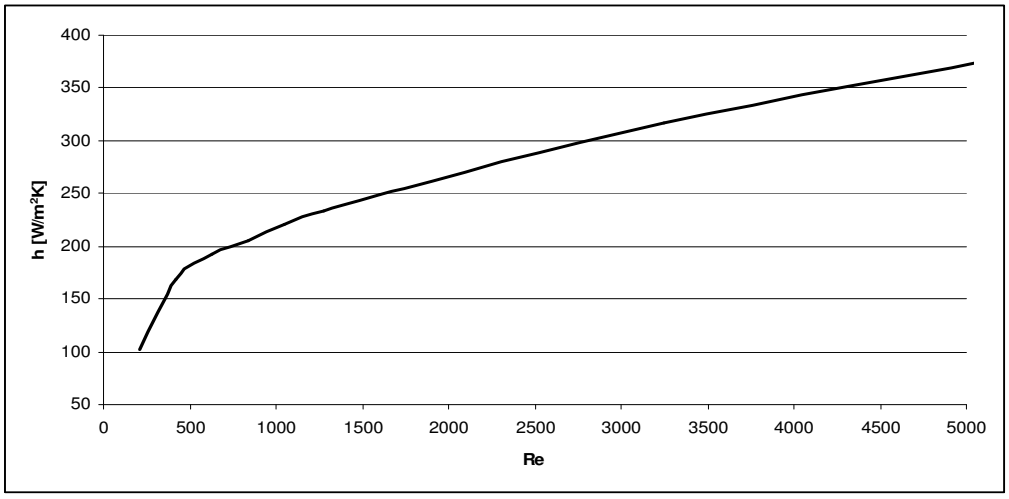

Figure 5.5. Average heat transfer coefficient vs. Reynolds number

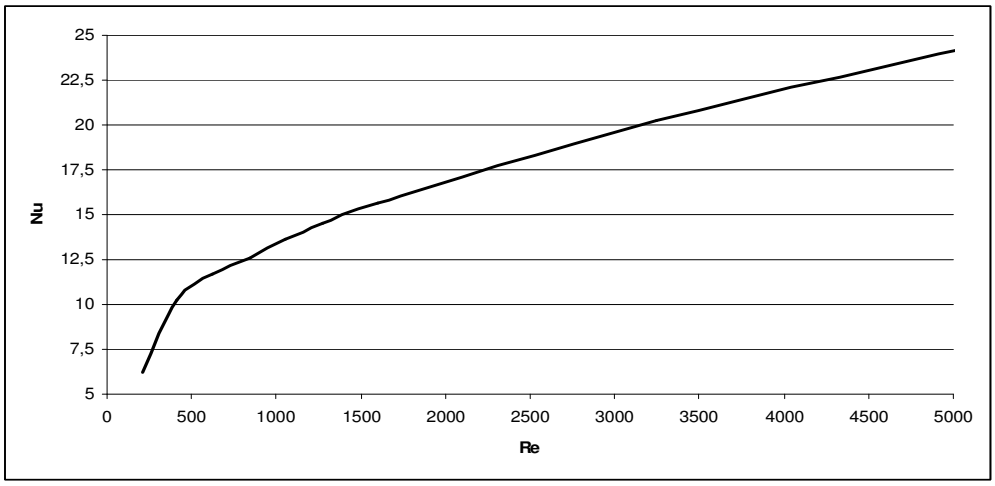

Figure 5.6. Nusselt number vs. Reynolds number

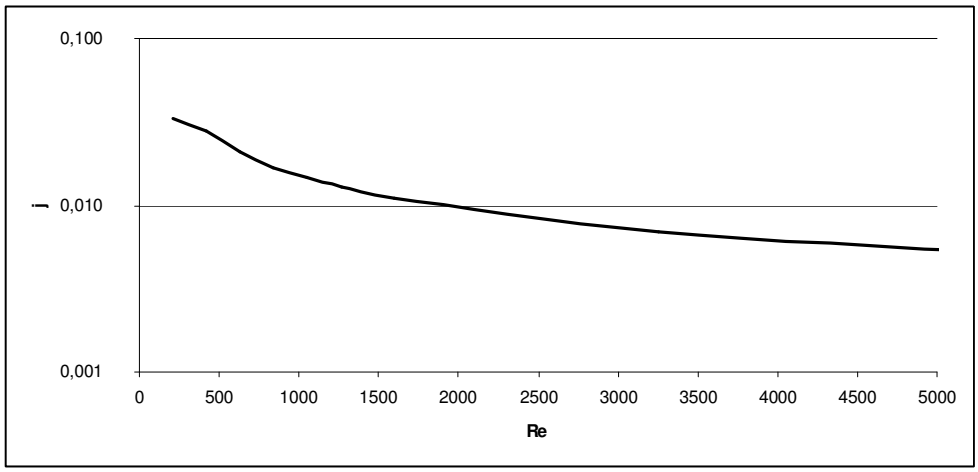

Figure 5.7. Colbourn j factor vs. Reynolds number

As seen in these figures above, the heat transfer coefficient and also Nusselt number increase with respect to increasing Reynolds number while the j factor decreases due to the fact that Reynolds numbers increases much faster than the Nusselt number.

The pressure drop and its non-dimensional form, the fanning friction factor f are shown in Figure 5.8 and 5.9 respectively. It is also seen that pressure drop increase and f factor decreases with increasing Reynolds number. Similarly, the reason of decreasing f factor is that kinematic energy of the flow (U^2) increases in much faster rate than the pressure drop.

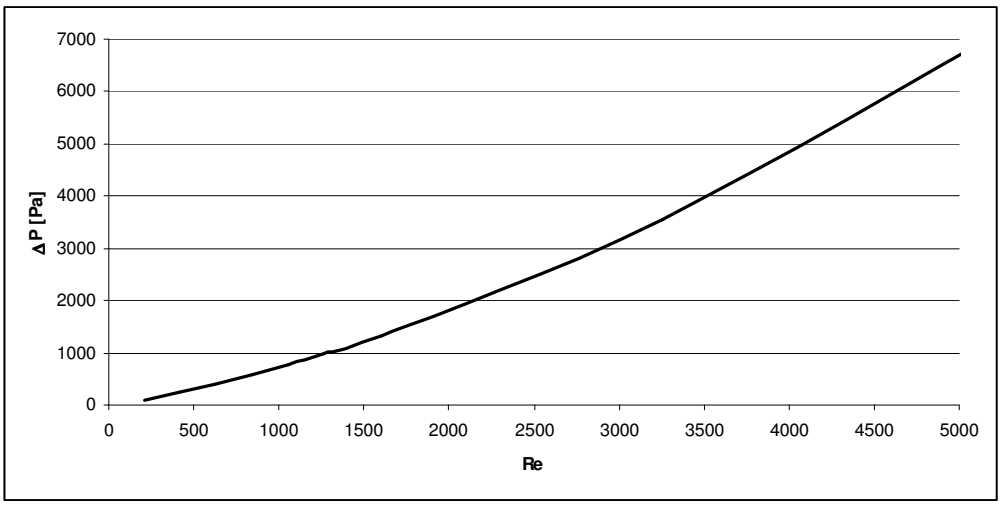

Figure 5.8. Pressure drop vs. Reynolds number

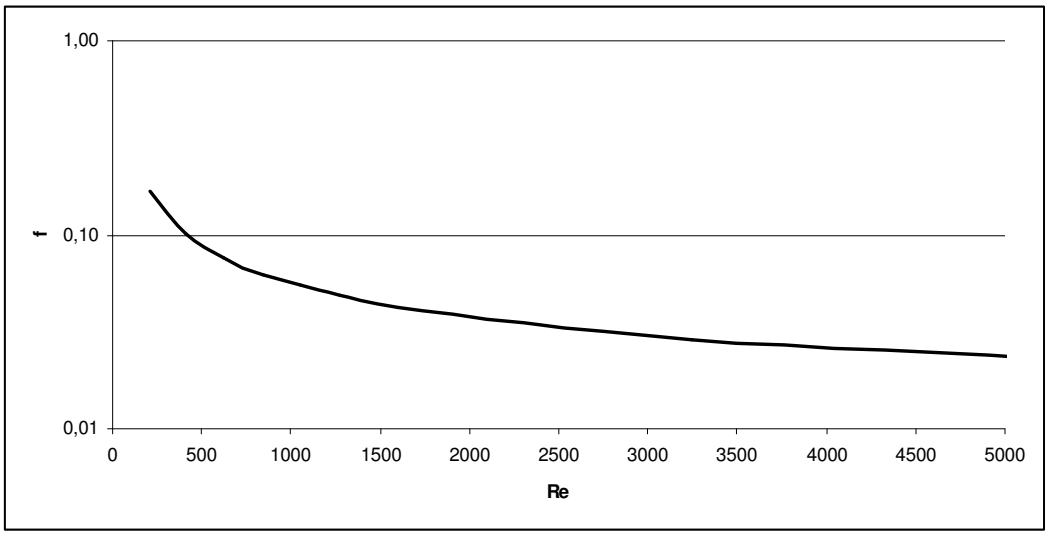

Figure 5.9. Fanning Friction f factor vs. Reynolds number

As mentioned in previous section, the numerical results for the study of Kays and London are under-predicted for Re > 2000. However, it must be mentioned that this difference between computations and experiments is most probably in the error margin. A steady turbulent model is being solved for Re > 800 in order to make certain if these under predictions can be overcome. The obtained results are compared with the laminar case and experimental results in Figure 5.10.

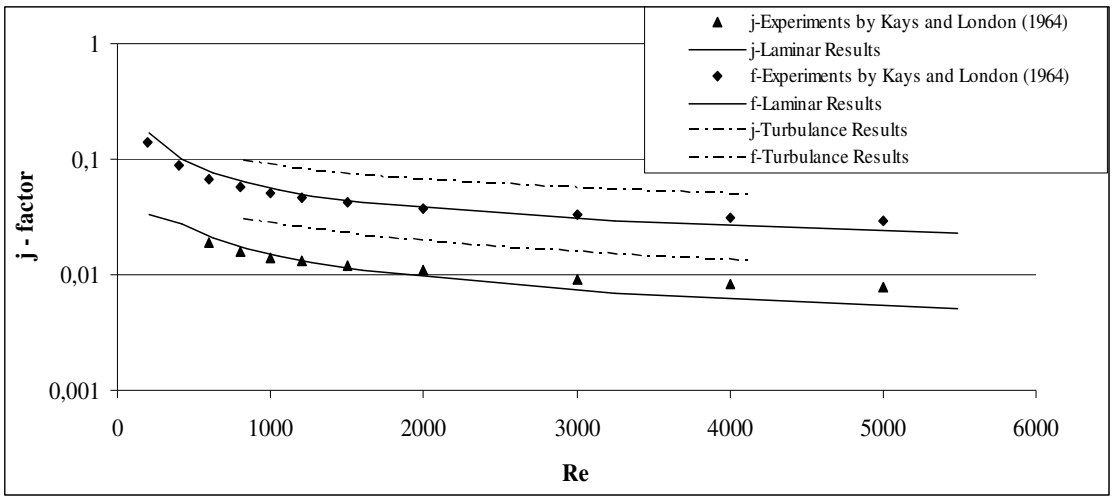

Figure 5.10. Comparison of Laminar and Turbulent Results

As shown in this figure above, the results obtained for turbulent flow model overly over-predicts both j and f factors. The k – ε numerical model used for turbulent case is known to be suitable for this kind of thin wake and boundary layer flows (Versteeg and Malalasekera 1995). The reason of this situation is conjectured to be that the flow in the OSF channel may never be fully turbulent even at high Reynolds numbers due to periodic disruption of boundary layers. Upon focusing on literature for this issue, the study of Joshi and Webb (1986) can make this situation clearer. Four different flow regimes in the OSF channel were identified focusing on the wake flow in between two successive fins by using flow visualization. As shown in Figure 5.11, in the first regime, the flow was laminar and steady. In the second regime, the oscillating flow structures were observed to appear in the transverse direction. In the third regime, the flow oscillated in the wake region. In the fourth regime, the vortex shedding started to become important. The second regime where the flow starts oscillate was assumed as transition point and after this point, the flow was usually assumed to be turbulent although, after this critical point, it may be unsteady laminar even for Re of 4500.

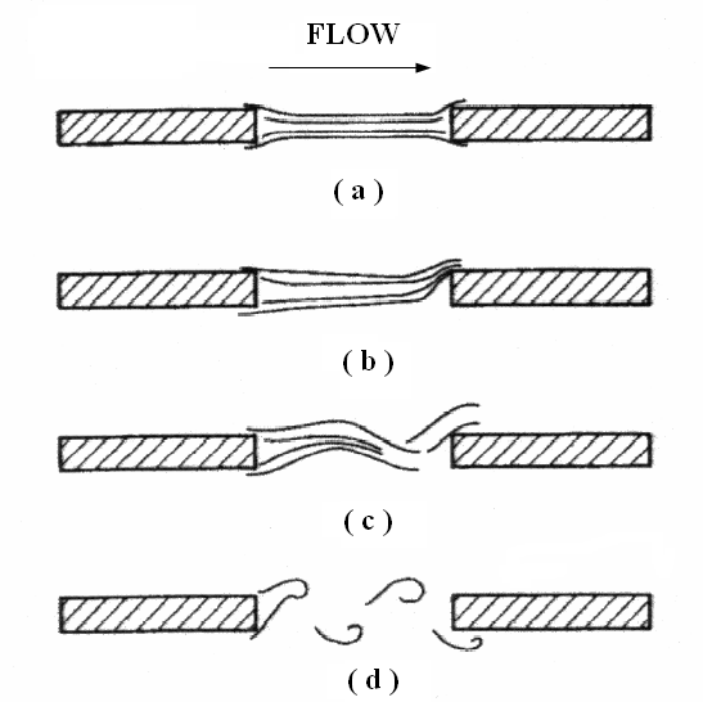

Figure 5.11. Flow patterns observed in the visualization experiments.
(Source: Joshi and Webb 1986)

An equation for the critical this Reynolds number, where the flow starts to oscillate, was also suggested by Joshi and Webb (1986). The equation includes geometrical parameters of the OSF and Reynolds number based on hydraulic diameter of the channel. In this thesis, the critical Reynolds number for the numerically analyzed OSF is computed as 1000 although the under-prediction of numerical analyses for laminar case with respect to the experimental analyses starts from 2000 for j factor and 3000 for f factor, Figure 5.10. The reason of obtained under prediction values as different critical Reynolds number from 1000 may be explained with the oscillation in the wake of the OSF channel obtained from flow visualization which does not make discernible effect on the results of the heat transfer and also the pressure drop. Actually, the critical Reynolds number points out the second region where small oscillations in wake region start. So the flow has to be unsteady laminar instead of turbulent. Various studies confirm the unsteadiness of the flow in OSF channel (Dejong and Zhang 1998, Saidi and Sunden 2001). According to those studies, when unsteady laminar flow exists in the OSF channel, Karman vortexes plays an important role, and affect the heat transfer on fin surfaces and also the pressure drop in the OSF channel. These vortexes start oscillating the flows at the trailing edges and this oscillation disturbs the boundary

layers downstream. The thermal resistance between the fin walls and the fluid decreases because of the disturbance of the boundary layer and this would result in an increase of heat transfer. The situation also results in an increase in pressure drop. Dejong and Zhang (1998) show that the increase in the heat transfer and also pressure drop are not as much as in turbulent flow. Thus, the flow in the Kays and London (1964) study may start to become unsteady and laminar beyond the Reynolds number of 2000.

Thus, in order to investigate the oscillation in the wake region, an unsteady laminar flow analyses are conducted in this thesis. Although the numerical model for analyzing the unsteady flow is successfully converged, no oscillations in the wakes of the OSF can be obtained. The reason of the situation may result from two important issues. One of them is that the very high frequency of the oscillated flow due to very thin fins. Secondly, the mesh number and also grid size in the core region of the flow may not be enough to resolve unsteady flow structures.

The contour plots of the velocity magnitude in the OSF channel are illustrated in the Figures 5.12 and 5.13 for the steady-state laminar and for steady-state turbulent flow respectively. For both cases, the region between 18^{th} and 20^{th} row of the OSF channel is illustrated, since the flow in this region is periodically fully developed. As shown in these figures, wake flow dominates the region. Upon focusing on the laminar case, at even lower Reynolds number such as 200, an impingement flow on the leading edges of the fin and a small recirculation region behind the trailing edges are observed. The wake flow fills between two successive fins beyond the Reynolds number, 1000. The same situation is obtained by Patankar and Prakash (1981). The Reynolds number related to this wake region must be defined with respect to the fin thickness. Since the fin thickness to hydraulic diameter ratio is about 20, wake Reynolds number is $1/20^{th}$ of the channel Reynolds number. The Reynolds numbers are tabulated in Table 5.2.

Table 5.2. Reynolds number based on hydraulic diameter and fin thickness.

Re_{wake}	10	50	75	150
Re_{Dh}	200	1000	1500	3000

It is known that the wake flow starts to oscillate around Reynolds number 60 (White “viscous fluid flow”, 1991) for a flow around a cylinder which corresponds to 1200 for our channel Reynolds number. Although our results start to deviate from the

experiments of Kays and London (1964) around the Re 2000. This may be due to the difference in geometry. The same observation was obtained in the study of Jossi and Webb (1998). Their flow visualization study shows that the boundary layers on the each fin always remain laminar even at high Reynolds numbers around 2500. Therefore, turbulent boundary layer may never exist on the fins because of the fact that the fin lengths are so small and they are interrupted along the flow direction.

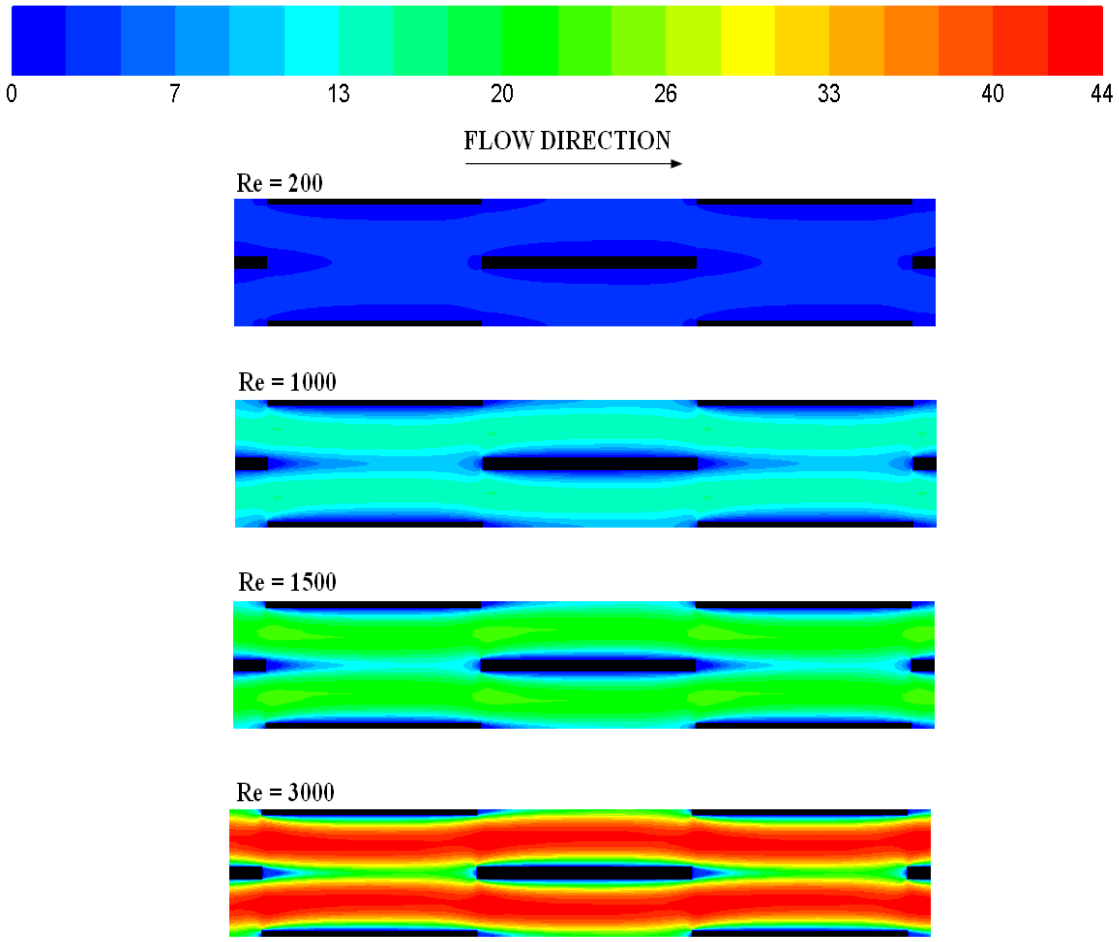

Figure 5.12. Contours of velocity magnitude for laminar flow.

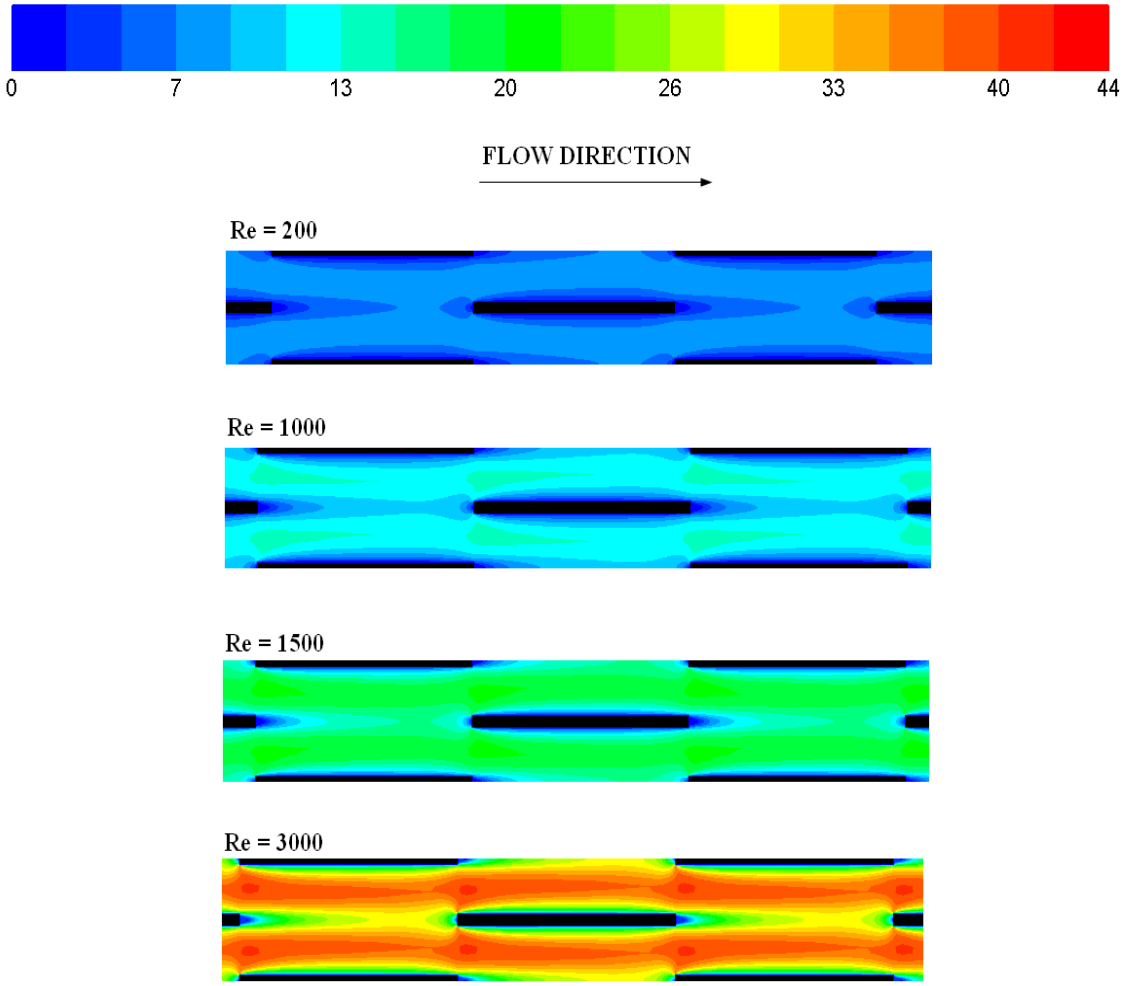

Figure 5.13. Contours of velocity magnitude for turbulent flow.

As mentioned earlier, another OSF is taken into consideration in this thesis (also known as Gürcan's fin). This fin is investigated numerically and also experimentally in the range of Reynolds numbers from 150 to 3500. Water is used as the heat transfer fluid and the heat is supplied uniformly by a ribbon heater. As shown in Figures 5.14 – 5.15, the Nusselt number and the Pressure drop over channel length data obtained by our experiments are compared with numerical data in order to show the accuracy of the experiments. As shown in those figures, the Nusselt numbers and also the pressure difference over channel length data are good agreement with the computational results for almost all Reynolds numbers. The Colbourn j factor and the fanning friction f factor results are also given in Figure 5.16 and Figure 5.17 respectively in order to give much more meaningful comment on the comparisons.

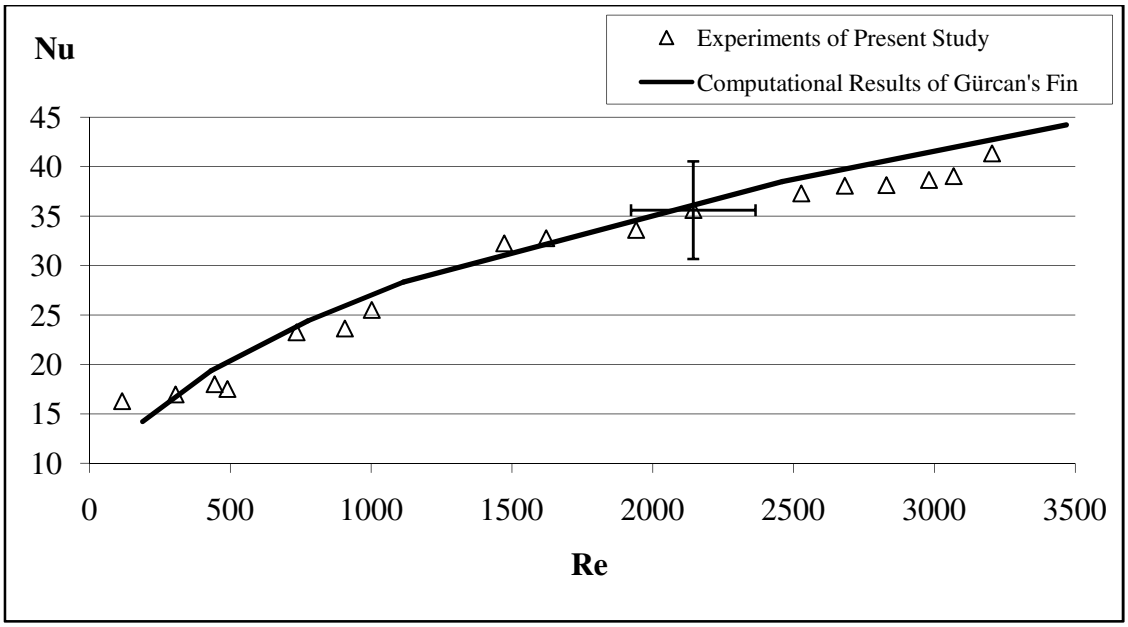

Figure 5.14. Comparisons of Nusselt numbers.

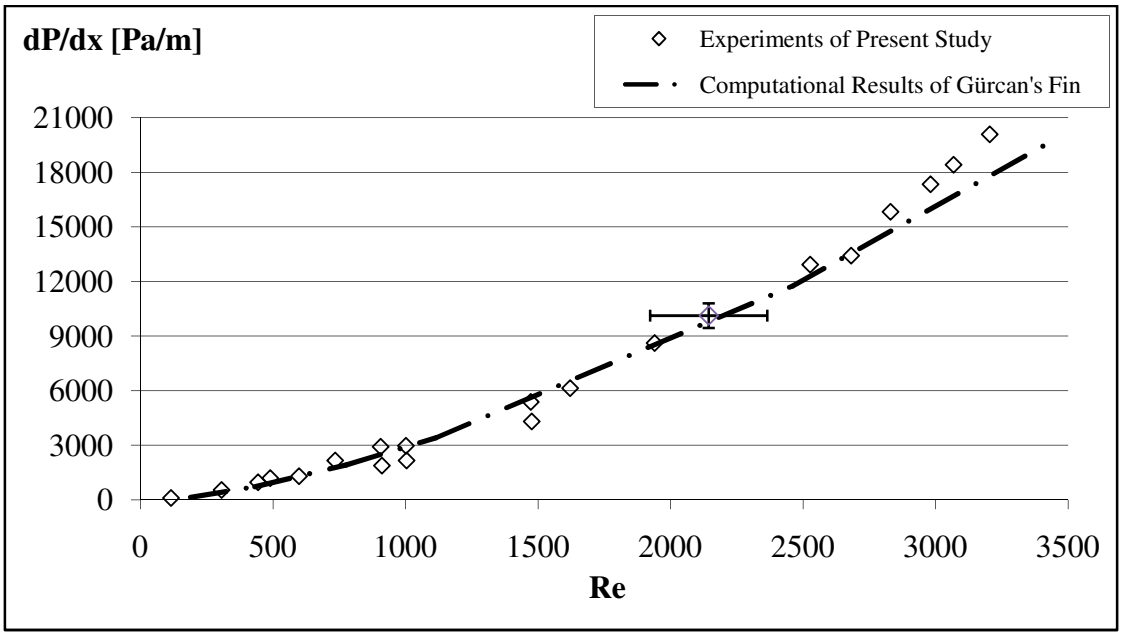

Figure 5.15. Comparisons of pressure drop over channel length.

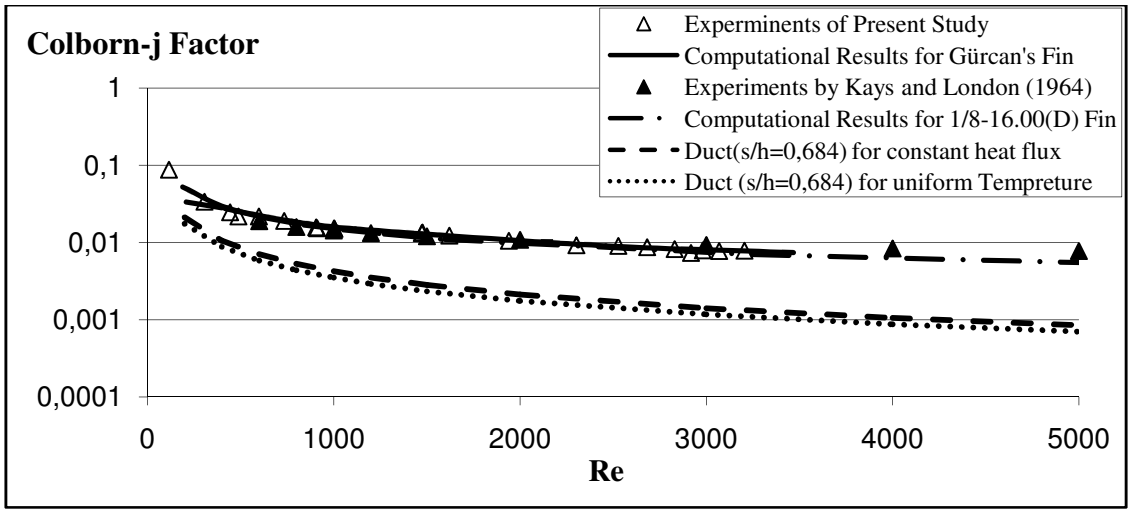

Figure 5.16. Comparison of experimental and numerical results for j factor.

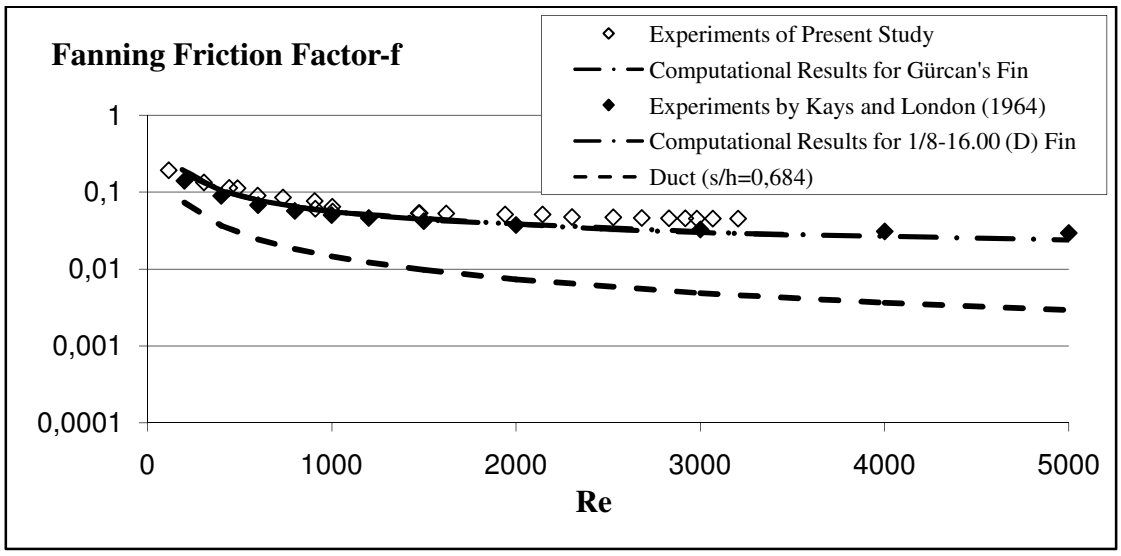

Figure 5.17. Comparison of experimental and numerical results for f factor.

As shown in those figures, the computational results of Gürcan's fin for j are in very good agreement with computations and other experiments as well. This is very encouraging for the dependability of the computations and as well as the experiments. On the other hand, fanning friction f factor are under-predicted with respect to our experimental results for Re >1500 although when comparing with experiment of Kays and London (1964) and the numerical results of the OSF with code 1/8-16.00(D) , the numerical results are strongly in good agreement similarly to the results given in Figure 5.4. This suggests a larger error margin for the pressure drop measurements.

Nevertheless, our experiments and computations are in very close proximity of the Kays and London's findings. Note that Kays and London' experiments and also our computational domain created in this thesis is conducted under an uniform temperature thermal boundary condition and by using air as a working fluid whose Prandtl number is almost 0.7. Although, the experiments and computational domain for Gürcan's fin is done by using constant heat flux thermal boundary condition and by using water as a working fluid whose Prandtl number is 2 to 4,35. The obtained results show that there is no remarkable effect of using different types of thermal boundary condition on the heat transfer and the pressure drop. It is also concluded that the differences between the Prandtl numbers of the fluids does not significantly affect the important flow characteristics. Detailed information about these two effects is given in next sections.

According to the results obtained in this study and the flow visualization results obtained by Dejong and Zhang (1998), and also Saidi and Sunden (2001), the flow regions in the OSF channel can be explained as

- For Re<2000, the flow in OSF channel is steady and mostly laminar
- At Re ~ 3000, oscillations in the flow start to affect on heat transfer and pressure drop. Flow is conjectured to be still laminar but unsteady.
- Beyond this critical Reynolds number, vortexes in the wakes are shed and at the same time, the oscillations become important.

5.3. Effect of Prandtl Number

The effect of Prandtl number is investigated by using air, $0.707 < Pr < 0.71$ and water, $2 < Pr < 4.35$ and ethylene glycol, $94 < Pr < 138$. The obtained results are illustrated as j and f factor vs. Re in Figure 5.18 and 5.19.

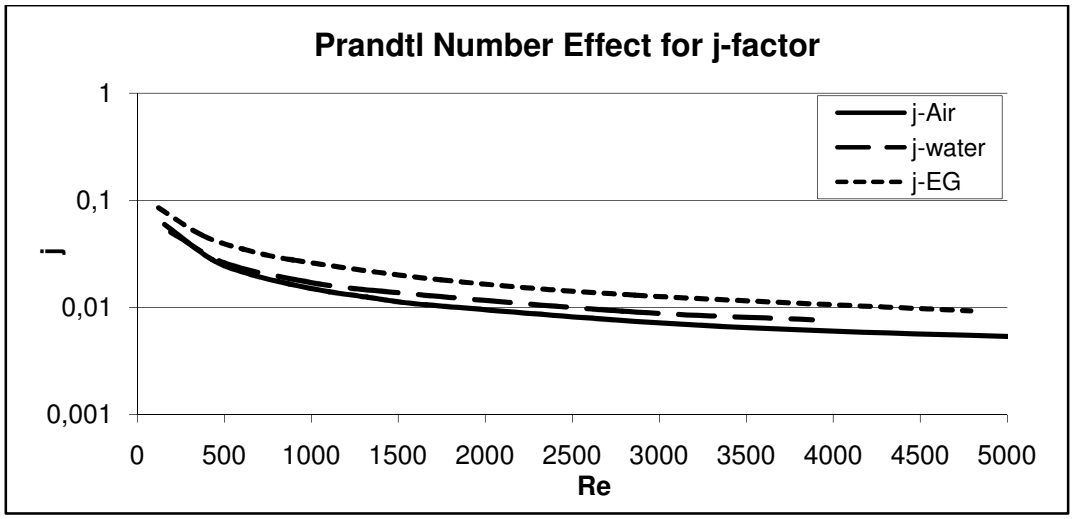

Figure 5.18. Effect of Prandtl number on heat transfer.

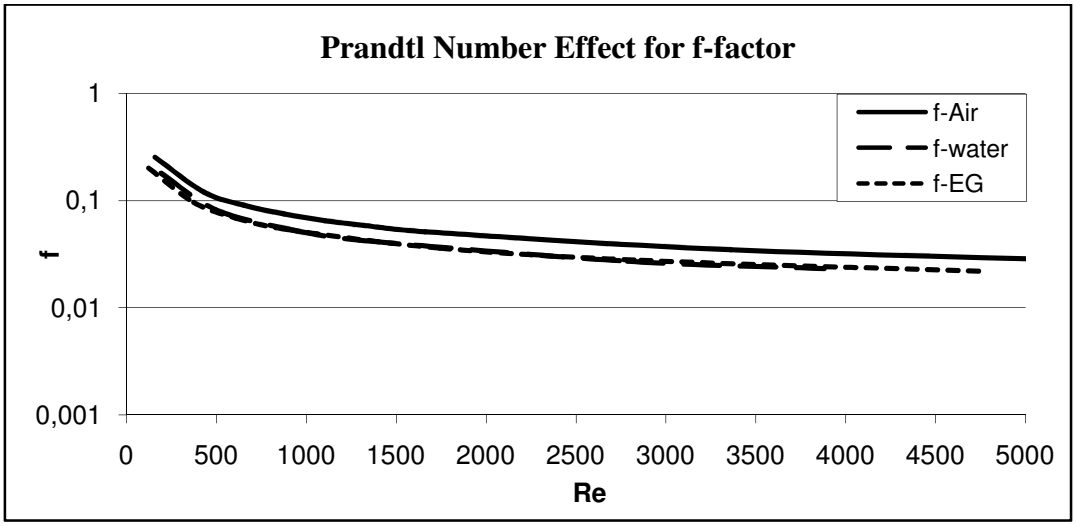

Figure 5.19. Effect of Prandtl number on pressure drop.

As shown in Figure 5.18, the Colbourn j factor increases with increasing Prandtl number. The reason of the increasing the j data, which is a non-dimensional form of heat transfer coefficient, with increasing Prandtl number is that the flow with Prandtl number of nearly one, the velocity and temperature boundary layers develop at almost same rate, however, for a fluid whose Prandtl number greater than one such as water the thermal boundary layer develops much slower than the hydraulic boundary layer. So the thermal developing region is much longer than the hydraulic developing length. The situation is similar to effect of entrance region of flow in a continuous duct, where a

higher heat transfer coefficient is gained at the entrance. Upon focusing on the results of the fanning friction factor-f given in Figure 5.19, for high Prandtl number fluids is almost same although the f factor data for Prandtl number of nearly one is higher than others.

5.4. Effect of Thermal Boundary Condition

The numerical domain for Gürcan's fin is numerically analyzed by supplying constant heat flux and uniform temperature thermal boundary conditions on top and bottom surfaces of it in order to investigate the effect of using different thermal boundary conditions on the heat transfer coefficient and also pressure drop. For that reason, a plane shown in Figure 5.20 is created at the middle of the 20th row of the OSF.

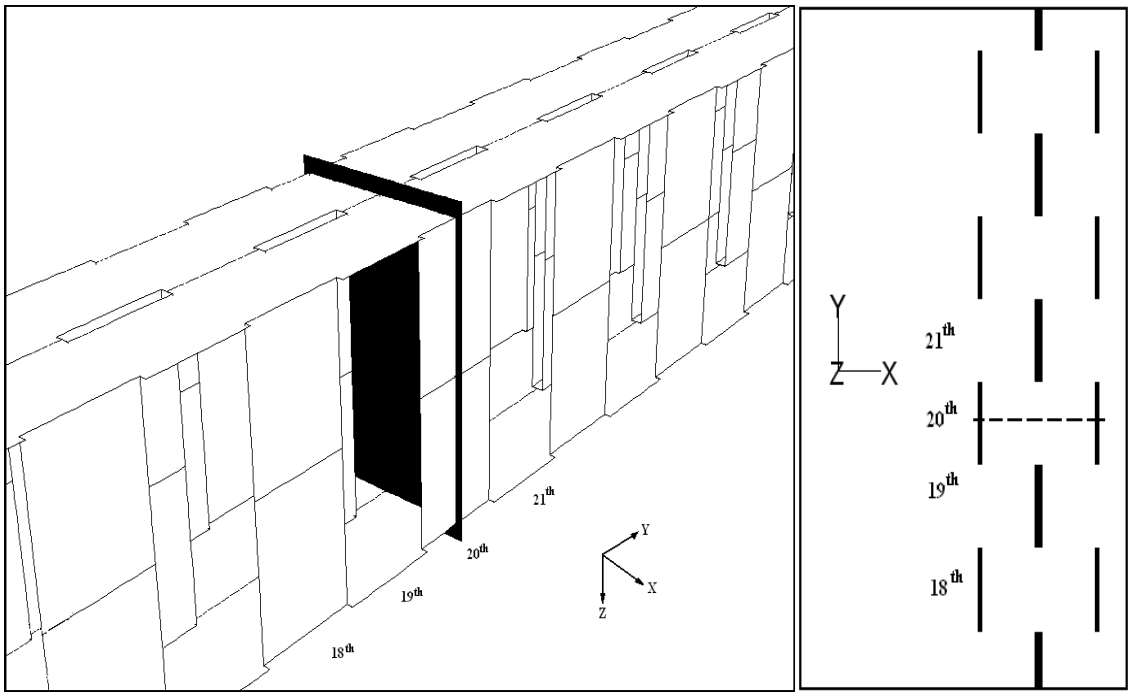

Figure 5.20. The plane at the middle of 20th row of the OSF.

The comparisons for the different boundary conditions are illustrated on the plane as temperature contour-lines in Figure 5.21.

Constant Heat Flux

Uniform Temperature

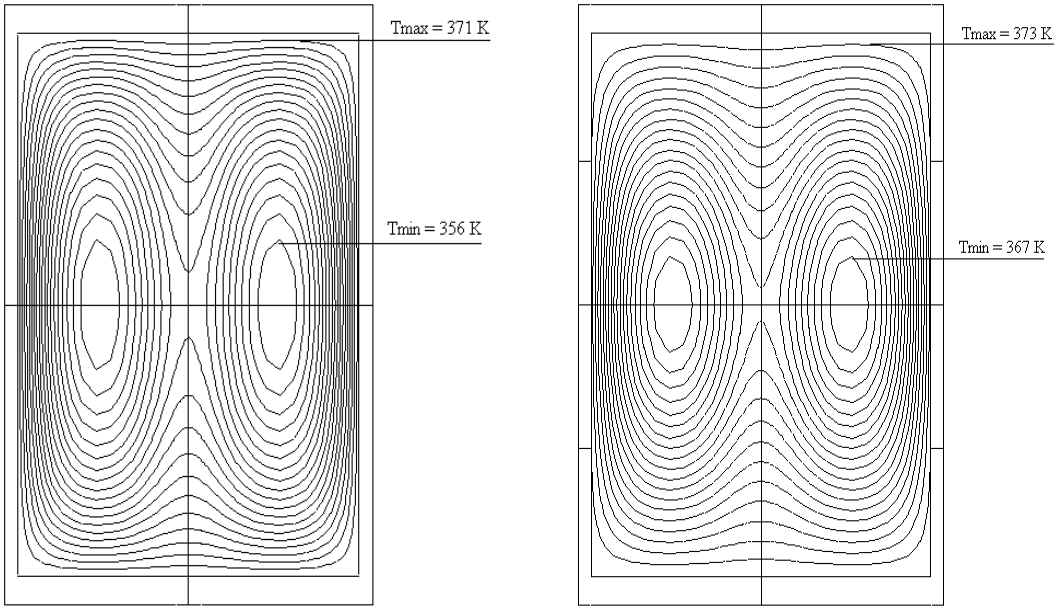

a-) Re = 200

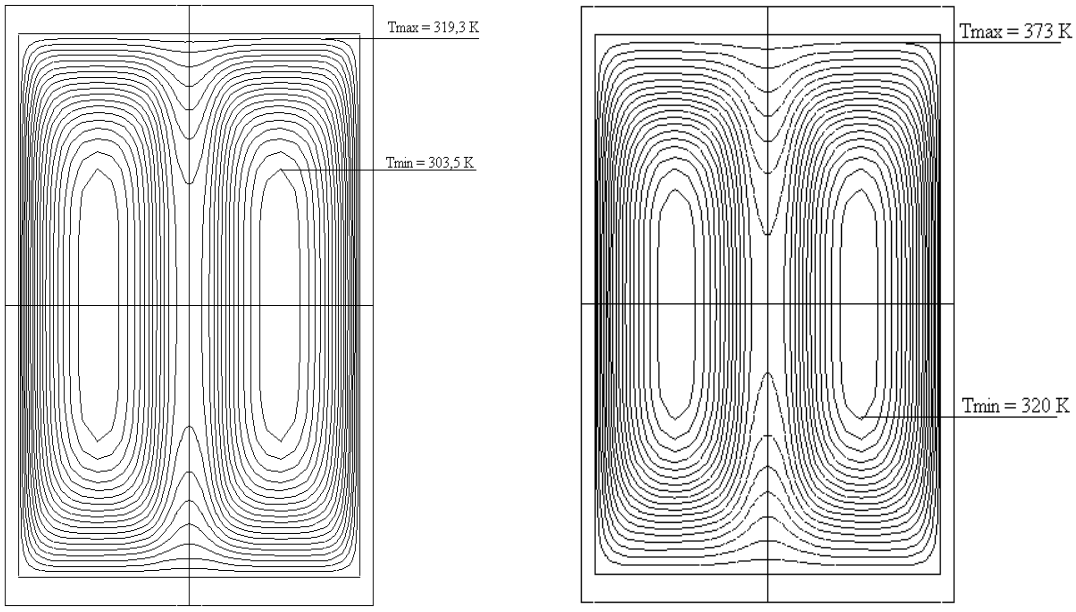

b-) Re = 1000

Figure 5.21. Comparison of the thermal boundary conditions

(cont. on next page)

.

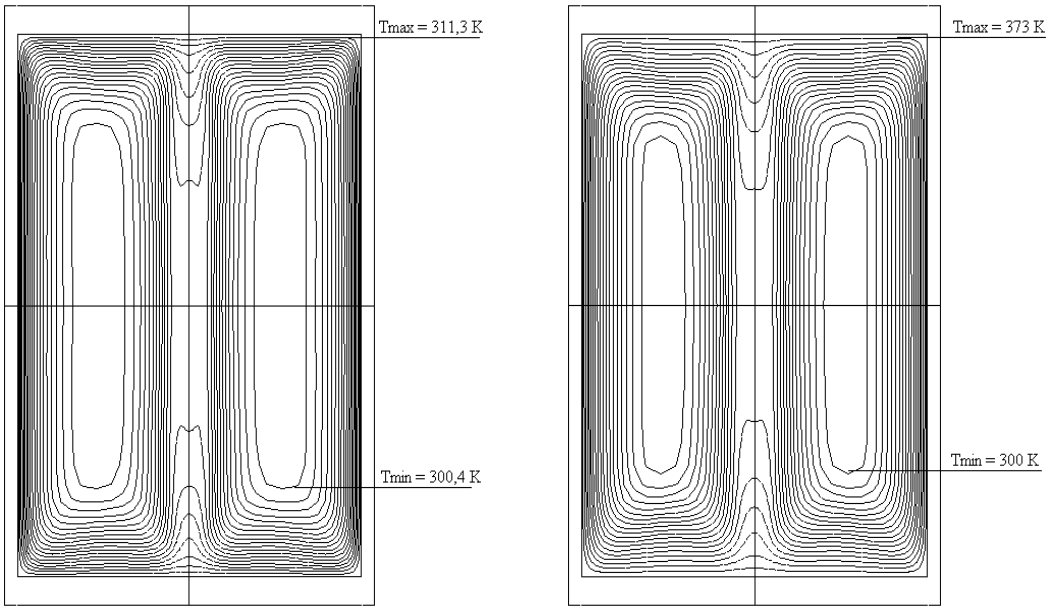

c-) Re = 3000

Figure 5.21. (cont.) Comparison of the thermal boundary conditions.

As shown in those figures above, using different types of boundary conditions for the considered OSFs does not make any difference between these two very different boundary conditions. For that reason, the velocity vectors and velocity contour-lines at different Reynolds numbers only for the uniform temperature thermal boundary condition are illustrated, respectively.

Secondary flows are observed as shown in Figure 5.22. These flows start from near the upper and bottom walls of the OSF due to the velocities at x direction, grown towards to center due to the velocities at z direction and the velocities at both x and z directions disappear at the center because of the velocities at y direction which is the flow direction. The velocities at x and z direction are substantially smaller than the velocity at y direction. Effects of these secondary flows to the heat transfer are subject to a future study.

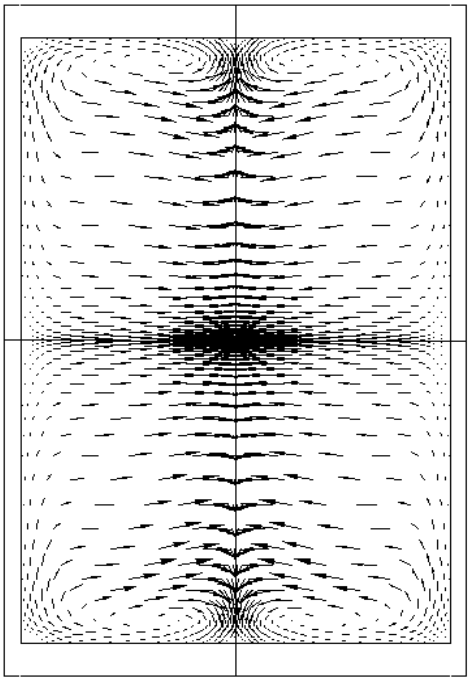

a) Re = 200

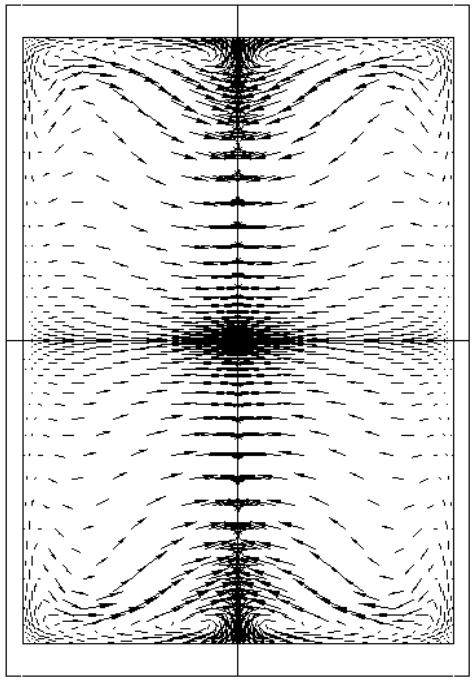

b) Re = 1000

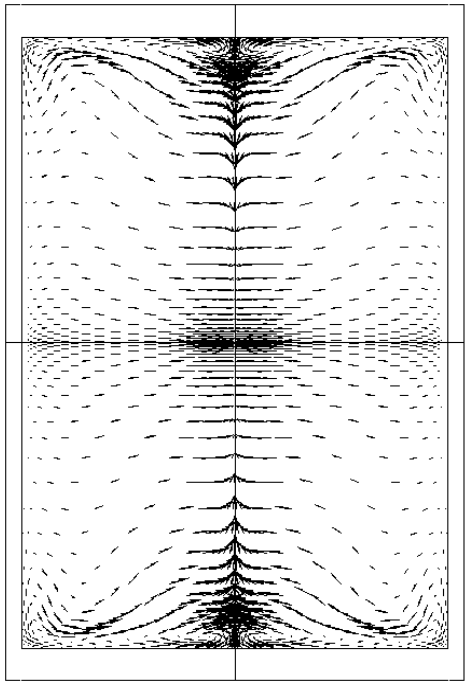

c) Re = 3000

Figure 5.22. Velocity vectors at x-z direction

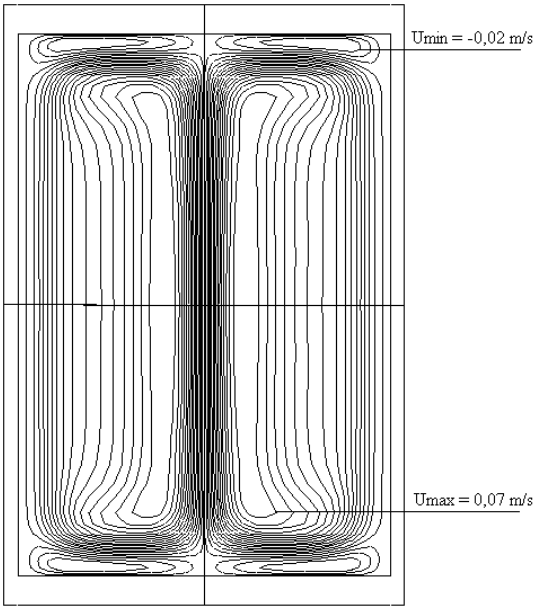

a) Re = 200

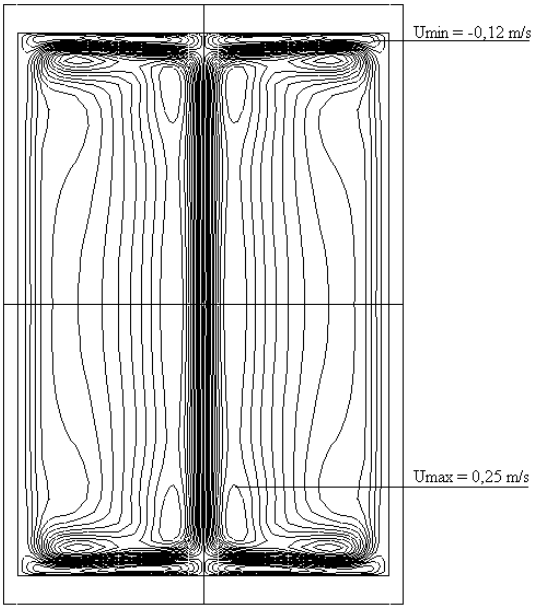

b-) Re = 1000

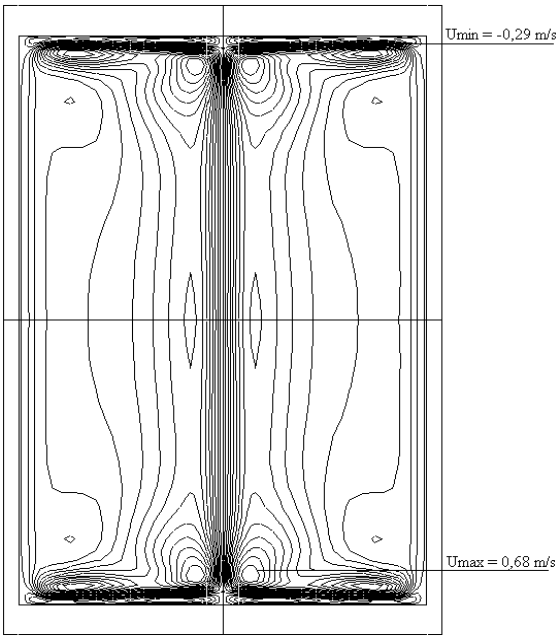

c-) Re = 3000

Figure 5.23. Contour-lines of velocity at x-direction.

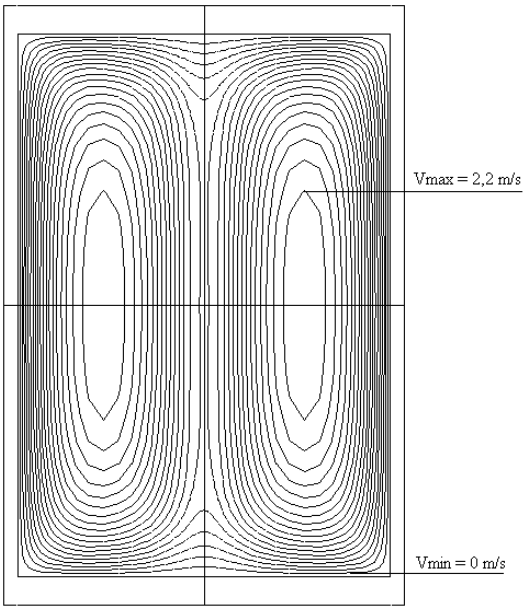

a) Re = 200

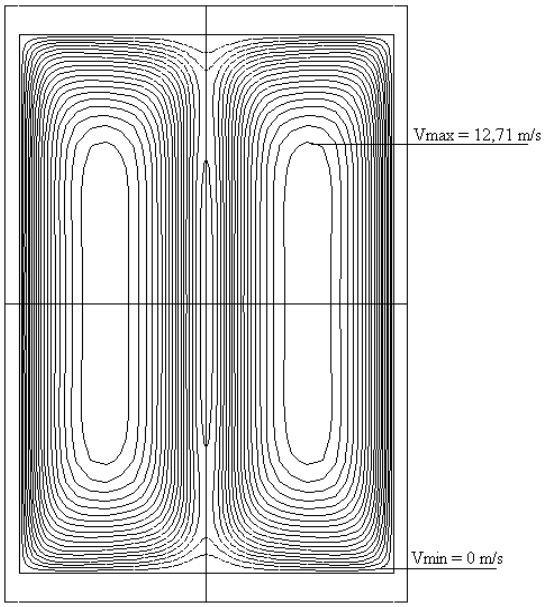

b) Re = 1000

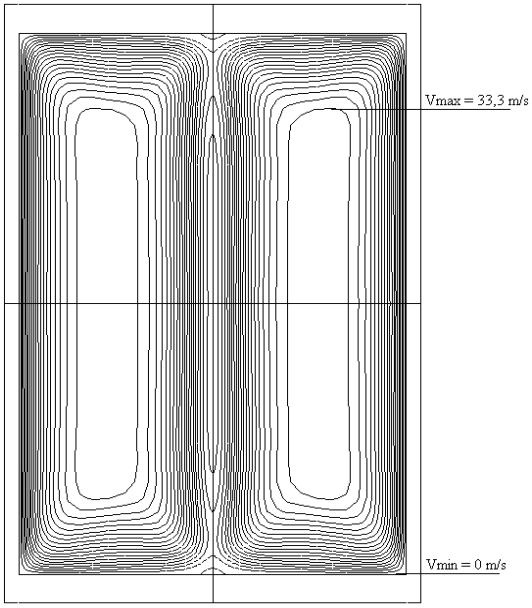

c) Re = 3000

Figure 5.24. Contour-lines of velocity at y-direction.

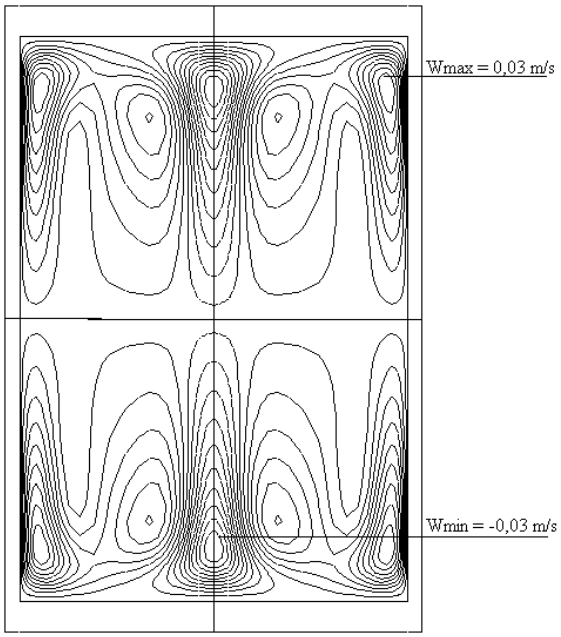

a) Re = 200

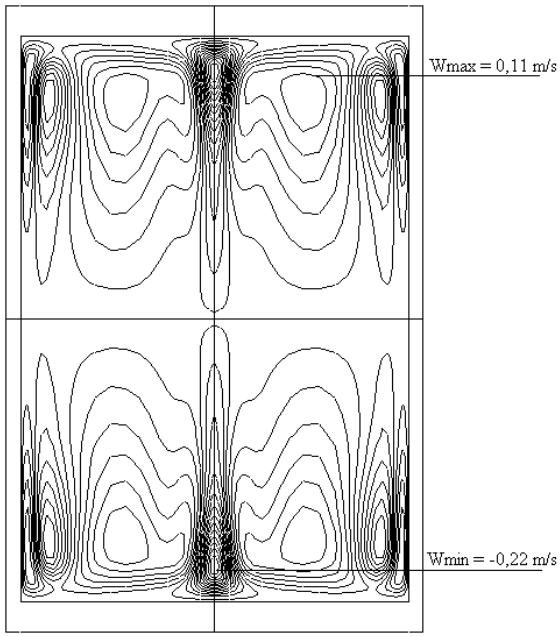

b) Re = 1000

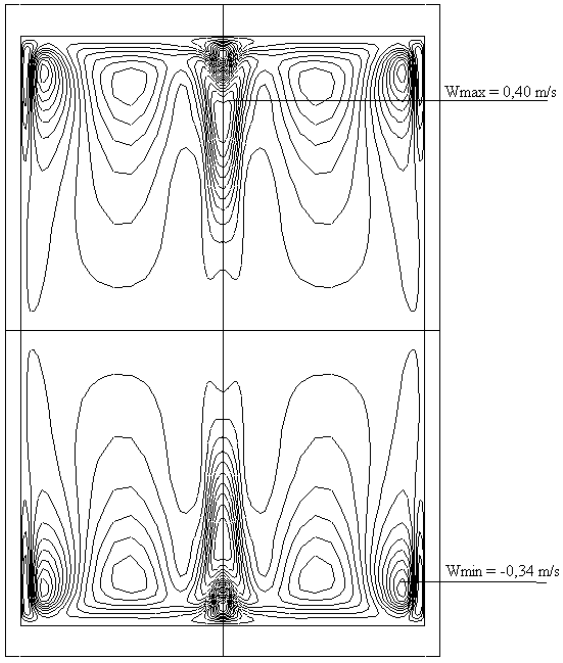

c) Re = 3000

Figure 5.25. Contour-lines of velocity at z-direction.

CHAPTER 6

CONCLUSIONS

The main aim of the present study is to check consistencies between computations and experiments of the heat transfer characteristics of an OSF. For that purpose, two experiments for two different OSFs (code: 1/8-16.00(D) by Kays and London (1964) and Gürcan's fin) are used. Note that the geometry of the OSF coded as "Gürcan's Fin" has not been studied up to now and there is no result about it in literature. Computations by using a 3-D numerical model created in this thesis for these fins are also performed. Analyzing the fins with using a 3-D numerical model, that is investigated as conjugate problem, is the main difference of the present thesis from the literature. The computational model for these fins is analyzed by assuming the flow as steady and laminar at the range of Reynolds number from 200 to 5000. The effect of flow regime in these types of OSFs is investigated. Also, the heat transfer boundary conditions and the Prandtl numbers of the computationally tested fluids are kept different for these fins in order to see the effect of those. The effect of Prandtl number is investigated by using air, $0.707 < Pr < 0.71$ and water, $2 < Pr < 4.35$ and ethylene glycol, $94 < Pr < 138$. The obtained results from experiments and also computations are illustrated as the Nusselt number and Colbourn j factor, which are the non-dimensional forms of the heat transfer coefficient, and the fanning friction f factor, which is the non-dimensional form of pressure drop. Moreover, all results (experimental and computational) are compared with Kays and London's experiments (1964) and also the results of Manglik and Bergles's correlations (1995). Results of the study can be summarized shortly below;

1. The heat transfer coefficient in an OSF channel increases with increasing Reynolds number as in duct flow. As expected, high pressure drop is also observed.

2. The computational results show that a deviation from experiments starts (as an under-prediction) at around Reynolds number, 2000 for j factor and 3000 for f factor.

3. The flow regimes for the OSFs are explained as

   - For Re < 2000, the flow in OSF channel is steady and mostly laminar thus, only the surface interruption increases the heat transfer and the pressure drop because the interruptions causes to periodically restart the boundary layers on fin surfaces and bound the growth of them
   - At Re ~ 3000, oscillations in the flow start to show an effect on heat transfer and pressure drop. Flow is conjectured to be still laminar but unsteady.
   - Beyond this critical Reynolds number, transverse vortexes that in the wakes are shed and at the same time, the oscillations become important. In this regime the vortices plays important role to improve the heat transfer by bringing fresh fluid from the main region to fin surface. But the swirling flow generated by the vortices near the fin surfaces increase the skin friction on them. Thus the pressure drop increases

4. The computations indicate that the Colbourn j factor increases with increasing Prandtl number. The fanning friction factor-f, for high Prandtl number fluids (water and Ethylene Glycol) is almost same although the f factor for Prandtl number of nearly one (air) is higher than others.
5. Using different types of thermal boundary condition, i.e. constant heat flux and uniform temperature, does not make any measurable difference in the heat transfer and the pressure drop characteristics.

After taking everything into consideration, future works may be suggested as

- Flow visualization analyses should be performed in a scale up model in order to determine the all of the flow regimes in an OSF
- Unsteady analyses should be conducted to obtain the effect of wake flow in these type of fins.

REFERENCES

Bejan, A., eds. 1993. *Heat Transfer.* New Jersey: John Wiley & Sons Inc.

Comini G., Croce G. and Nonino C. 2004. Modeling of Convection Enhancement Mechanisms. *International Journal of Numerical Methods for Heat and Fluid Flow*.14:66-84.

Çengel A. Y. and Cimbala M. J., eds. 2006. *Fluid Mechanics: Fundamentals and Applications*: The McGrawHill.

Dejong N. C. and Jacobi A. M. 1997. Experimental Study of Flow and Heat Transfer in Parallel – Plate Arrays: Local, Row-by-Row and Surface Average Behavior. *International Journal of Heat Mass Transfer* 40:1365-1378.

Dejong N. C., Zhang L. W., Jacobi A. M., Balchandar S., and Tafti D. K. 1998. A Complementary Experimental and Numerical Study of Flow and Heat Transfer in Offset Strip-Fin Heat Exchangers. *Journal of Heat Transfer* 120:690:702.

Dong J., Chen J., Chen Z., and Zhou Y. 2007. Air-side Thermal Hydraulic Performance of Offset Strip Fin Aluminum Heat Exchangers. *Applied Thermal Engineering* 27:306-313.

Fluent Incorporation, 2006. *Fluent 6.3. User's Guide*. Canterra Resource Park 10 Cavendish Court Lebanon: Fluent Inc.

Guo L., Chen J., Quin F., Chen Z. and Zhang W. 2008. Empirical Correlations for Lubricant side Heat Transfer and Friction Characteristics of HPD type Steel Offset Strip Fins. *International Communications in Heat and Mass Transfer* 35: 251-262.

Guo L., Chen J., Quin F., Chen Z. and Zhou Y. 2007. Influence of Geometrical Factors and Pressing Mould Wear on Thermal-Hydraulic Characteristics for Steel Offset Strip Fins at Low Reynolds Number. *International Journal of Thermal Science* 46:1285-1296.

Hu S and Herold K. E. 1995a. Prandtl number effect on offset fin heat exchanger performance: predictive model for heat transfer and pressure drop. *International Journal of Heat and Mass Transfer* 38(6):1043–1051.

Hu S and Herold K. E. 1995b. Prandtl number effect on offset fin heat exchanger performance: experimental results. *International Journal of Heat and Mass Transfer* 38(6):1053–1061.

Joshi H.M. and Webb R.L. 1987. Heat Transfer and Friction in Offset Strip Fin Heat exchanger. *International Journal of Heat and Mass Transfer* 30(1):69-80.

Kalkar A.K. and Patankar S.V. 1990. Numerical Prediction of Fluid Flow and Heat Transfer in a Circular Tube with Longitudinal Fins Interrupted in the Streamwise Direction. *Journal of Heat Transfer* 112:342-351.

Kays W. M. and London A. L. 1964. *Compact Heat Exchangers*. 2nd edition, NewYork: McGraw Hill.

Kline S. J. and Mc Clintock F. A. 1953. Describing Uncertainties in single-sample experiments. *Mechanical Engineering* 75(1):3-9.

Löhner, R. 2008. *Applied computational fluid dynamics techniques. An introduction based on finite element methods.* Chichester, West Sussex: John Wiley&Sons Inc.

Manglik R. M. and Bergles A. E. 1995. Heat Transfer and Pressure Drop Correlations for the Rectangular Offset Strip Fin Compact Heat Exchanger. *Experimental Thermal Fluid Science* 10:171 – 180.

Maughan J.R. and Incropera F.P. 1990a. Mixed Convection Heat Transfer with Longitudinal Fins in a Horizontal Parallel Plate Channel: Part I-Numerical Results. *Journal of Heat Transfer* 112:612-622.

Maughan J.R. and Incropera F.P. 1990b. Mixed Convection Heat Transfer with Longitudinal Fins in a Horizontal Parallel Plate Channel: Part II-Experimental Results. *Journal of Heat Transfer* 112:634:645.

Michna J. G., Jacobi A. M. and Burton L. R. 2005. Air-side Thermal – Hydraulic Performance of an Offset Strip Fin Array at Reynolds Numbers up to 120 000, Fifth *International Conference on Enhanced, Compact and Ultra – Compact Heat exchangers: Science, Engineering and Technology* 8-14.

Muzychka Y. S. and Yovanovich M. M. 2001a. Modeling the f and j Characteristics of the Offset Strip Fin Array. *Enhanced Heat Transfer* 8:261-267.

Muzychka Y. S. and Yovanovich M. M. 2001b. Modeling the f and j Characteristics for Transverse Flow through an Offset Strip Fin at Low Reynolds Number. *Enhanced Heat Transfer* 8:243-259.

Patankar S.V. and Prakash C. 1981. An Analysis of Plate Thickness on Laminar Flow and Heat Transfer in Interrupted Plate Passages. *International Journal of Heat and Mass Transfer* 24:1801-1810.

Saidi A. and Sunden B. 2001. A Numerical Investigation of Heat Transfer Enhancement in Offset Strip Fin Heat exchangers in Self-Sustained Oscillatory Flow. *International Journal of Numerical Methods for Heat and Fluid Flow* 11(7):699-716.

Sparrow, E. M., Baliga, B. R. and Patankar S. V. 1977. Heat Transfer and Fluid Flow Analysis of Interrupted – wall Channels, with Application to Heat Exchangers, *Journal of Heat Transfer* 99: 4-11.

Shah, R.K. and Sekulic, D.P. eds. 2003. *Fundementals of heat excgangers design.* New Jersey: John Wiley & Sons Inc.

Tinaut F.V., Melgar A. and Rahman Ali A.A. 1992. Correlations for Heat Transfer and Flow Friction Characteristics of Compact Plate-Type Heat exchangers. *International Journal of Heat and Mass Transfer* 35(7):1659-1665.

Versteeg, H.K. and Malalasekera, W., eds. 1995. *An introduction to computational fluid dynamics the finite volume method.* London: Longman Group Ltd.

Weiting A.R. 1975. Empirical Correlations for Heat Transfer and Flow Friction Characteristics of Rectangular Offset Fin Plate Heat Exchangers. *Transactions of ASME Journal of Heat Transfer* 97: 488-497.

Zhang L.W., Balachandar S., Tafti D.K. and Najjar F.M. 1997. Heat Transfer Enhancement Mechanisms in Inline and Staggered Parallel-Plate Fin Heat exchangers. *International Journal of Heat and Mass Transfer* 40(10):2307-2325.